Uncertainty reduction in image log fracture interpretation, and its implications to the geological history of the Geneva Basin, Switzerland

M.E.C.J. Doesburg

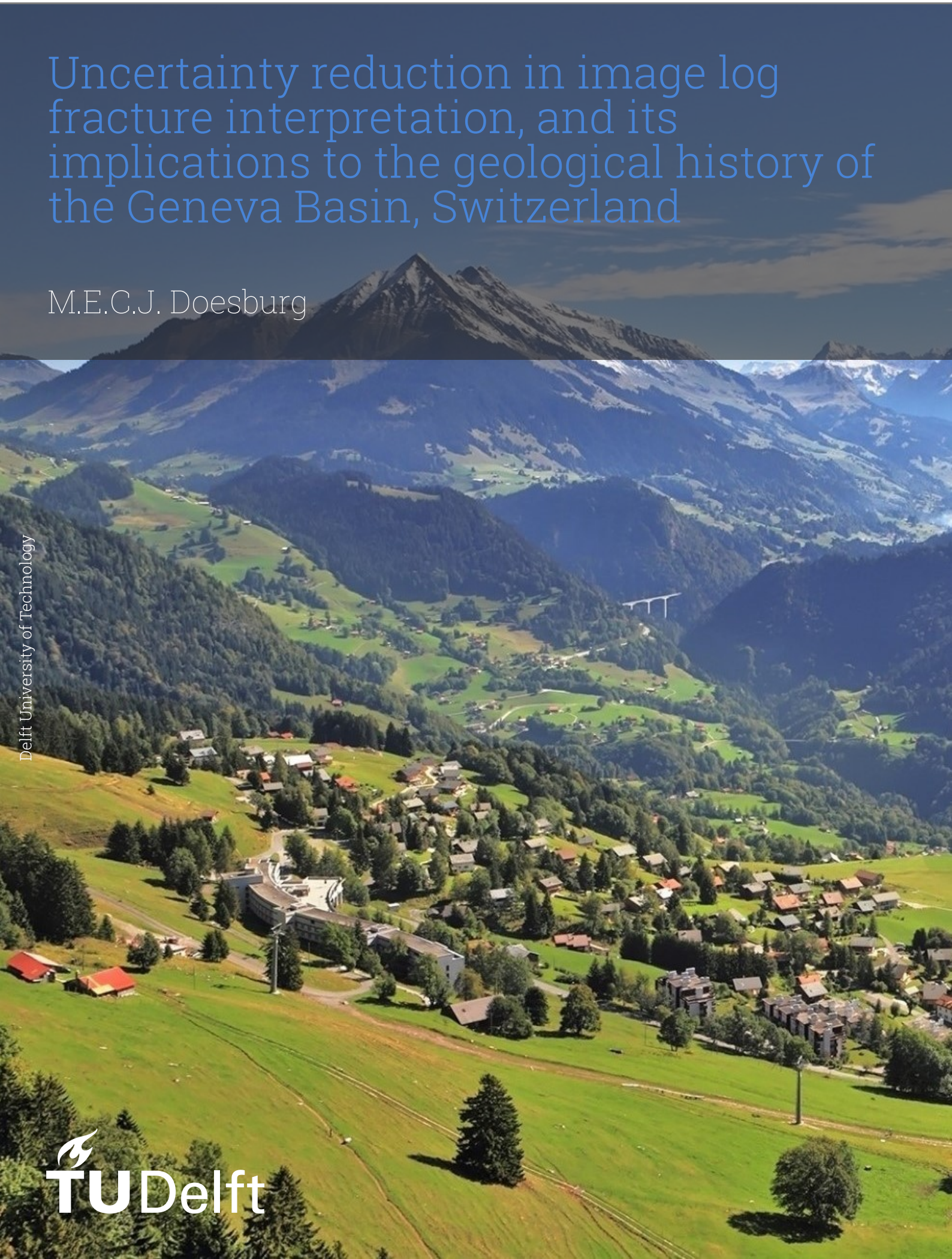

Delft University of Technology

TU Delft

Uncertainty reduction in image log fracture interpretation, and its implications to the geological history of the Geneva Basin, Switzerland

by

M.E.C.J. Doesburg

Student Name	Student Number
Myrthe Doesburg	5136369

Supervisor:	Dr. P-O.B.R. Bruna
Supervisor:	Prof. Dr. G. Bertotti
Supervisor:	Msc. J. Hupkes
Supervisor:	Dr. A.D. Danillidis
Faculty:	Faculty of Civil Engineering and Geosciences, Delft
Course name:	AESM2310 - Final Thesis Geo-Energy Engineering

Cover:	Photograph by Success Tours
Style:	TU Delft Report Style

TU Delft

Abstract

Natural fractures play a crucial role in many sustainable subsurface applications, particularly in reservoirs with low primary porosity and permeability. Therefore, fracture analysis has become a fundamental aspect of geosciences, often starting with fracture interpretation from borehole image logs. It has been widely recognized that interpretations come with uncertainties; nevertheless, there is a current lack of both quantitative and qualitative understanding regarding differences among interpretations. This study aims to address this gap, by performing a statistical analysis on five interpretations of the same well, highlighting their differences and similarities. Based on the results from the analysis, a workflow was created to reduce uncertainties in fracture interpretations from image logs.

The created workflow was then applied to two wells in the Geneva Basin, Switzerland; associated with a geothermal project aiming to produce heat and electricity from the Upper Cretaceous limestone rocks. Research has shown that these rocks form a tight reservoir, and fluid flow will rely on the presence of fracture networks. In the two wells, a total of eight fracture sets were defined based on movement and relative chronology, and used to reconstruct the fracture history of the basin. This led to the identification of four Mesozoic to Cenozoic stress regimes: 1) a normal or strike-slip regime, 2) a NE-SW reverse regime, 3) a normal regime, and 4) a NW-SE reverse regime. The latter is considered the main deformation event of the region: the Late Miocene fold-and-thrust tectonics. In the Geneva Basin, this event is represented by a pair of NE-SW striking conjugates, which forms the majority of observed fractures. The fifth fracture set is believed to be fault-related and was only observed in one of the wells.

Beyond the regional implications, this study emphasizes the importance of uncertainty reduction in the early stages of fracture analysis, and its effects on establishing a reliable fracture history.

Preface

Some years ago I came to Delft to study Geo-Energy Engineering at the Technical University, not yet knowing what the upcoming years would hold. For me, the TU Delft is an environment filled with possibilities, stimulating anyone to try new things, go greener and make an impact. During my masters, I learned programming, went on field trips, got to know the industry and studied a lot of fractures. But not less important, I challenged myself, learned to think creatively and improved my problem solving skills.

Firstly, I would like to thank the Services Industriels de Genève, the University of Geneva and Prof. Moscariello for providing me with their data.

I would like to thank Pierre-Olivier Bruna for being the main supervisor during my Master Thesis; I learned a lot from your expertise, you often gave me valuable insights and helped me grow confidence in my work. And thank you specifically, for giving me the freedom to proceed at my own pace. Additionally, I would like to thank Giovanni Bertotti, for providing me valuable feedback during the project and be critical to my own work. Moreover, thanks to Jasper Hupkes, with whom I started studying in Utrecht and, in a funny, unexpected way, ended my studies here in Delft. I very much enjoyed working with you three over the past months. I also want to express my gratitude to Andrea Moscariello, from the University of Geneva, for believing in our work on the GEothermie2020 project, and to Alexandros Daniilidis for participating in my thesis committee.

Aside from that, I would like to thank Guillaume Rongier, who helped me get along on my statistical analysis, and Rien Corstanje, for always being available for all our WellCAD related questions.

I would like to thank my incredible family, friends and roommates, for their support during my studies and for making Delft feel like home. Lastly, I wish to thank my parents, brother, Frits and Fre(d). I could not have done it without you.

M.E.C.J. Doesburg
Delft, September 2023

Contents

List of Figures

List of Tables

1

Introduction

Natural fractures play a crucial role in reservoirs with low primary porosity and permeability because they can act as pathways for fluid flow. To do so, fractures must be open and form connected networks (Allen and Allen, 2013). Fracture analysis is, therefore, essential in many sustainable subsurface applications, like geothermal energy subtraction, hydrogen storage, and CO_2 storage.

Not less important, fractures are the most important indicators for paleostresses and are key in reconstructing the structural history of a region. The fracture type and its orientation provide valuable information on the stresses that formed them. In some cases, fractures exhibit relationships with other geological structures that offer indications of their relative chronology. These relationships make it possible to determine the relative timing of geological events.

Fracture data can be acquired from outcrops, seismic lines, cores, or boreholes. Cores and boreholes directly sample the subsurface and provide sufficient resolution to identify small-scale fractures accurately. However, they provide limited spatial coverage, and due to their vertical orientation lateral variations are not represented. Although both cores and boreholes provide valuable sources of subsurface information, boreholes are more cost-effective and therefore often favoured over cores.

For those reasons, borehole data often forms the base of geomodels. Fracture interpretation heavily relies on borehole image logs, which provide essential input for fracture models to predict fluid flow and reservoir capacities. However, it is important to recognize that fracture interpretations will always come with uncertainties, which can result in inaccurate models. While several studies have focused on the influence of different interpretations on subsequent modeling (Bond, 2015; Schaaf and Bond, 2019), very few studies have attempted to quantify and qualify the differences in interpretations themselves.

Understanding the uncertainties related to fracture interpretation is thus essential for optimizing geothermal projects. By analyzing and, where possible, reducing the uncertainties, more reliable future models can be developed, contributing to the successful development of geothermal plays.

Reducing uncertainties in fracture interpretations is of key importance in the Geneva Basin, where the Geneva government, the Services Industriels de Genève (SIG), and the University of Geneva (UNIGE) started the 'GEothermie2020 project' in 2013 (Lecompte, 2019). The project aims to produce heat and electricity from geothermal energy in the canton of Geneva to reduce greenhouse emissions. During the exploration phase of the project, two boreholes were acquired: GEo-01 and GEo-02 (Figure 1.1). Both boreholes reach the Upper Cretaceous limestone rocks, which have a high potential for developing geothermal energy as suggested by the work of Rusillon, 2018. However, the work also mentions that primary porosity and permeability are relatively low, and flow will rely on the existence of fracture networks. Several studies have focused on fracture interpretation from GEo-01 (Jorge, 2022; Koumrouyan, 2019; Lo, 2019) and GEo-02 (Andre-Ghapgou, 2021) and on subsequent fracture modeling (Alhamad, 2021; Jorge, 2022; Lo, 2019).

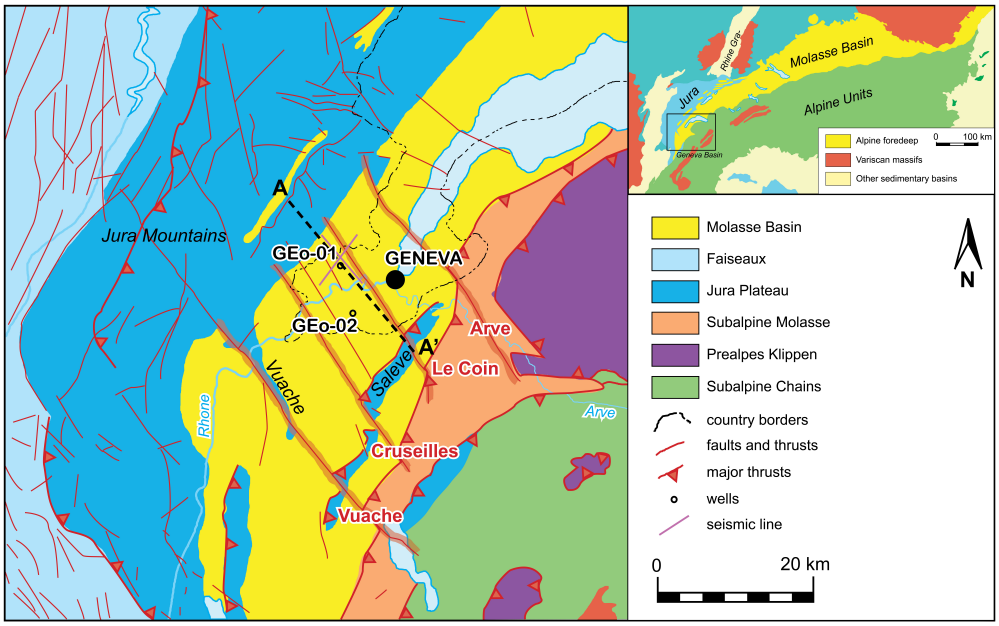

Figure 1.1: Geological map of A) the Molasse Basin and B) the Geneva Basin (modified from Sommaruga et al., 2017) In the center of The Geneva Basin Europe lies the Geneva Basin: a low relief area bounded by Lake Geneva and the Jura, Salève, and Vuache mountains. The cross-section A - A' can be found in Figure 3.1.

This study consists of two main components. The first part involved a statistical analysis of the available interpretations of GEo-01. In this part, a workflow was developed to reduce uncertainty in fracture picking on image logs. In the second part of the study, the workflow was applied to GEo-01 and GEo-02, resulting in an improved fracture database. The findings contributed to a better understanding of the geological evolution of the basin and might ultimately contribute to the generation of more realistic fracture models.

The main question this study tries to answer is the following:

'How to reduce uncertainties in fracture interpretation from borehole images to optimize fracture data acquisition and provide a reliable structural history in the Geneva Basin?'

1.1. Outline of the report

Chapter 2 and 3 begin with providing background information on fractures in general and the geological setting of the Geneva Basin. Chapter 4 introduces the borehole data of GEo-01 and GEo-02; chapter 5 concerns the research workflow and methodology. Chapter 6 addresses the first part of this study and presents the findings of the statistical analysis performed on five fracture interpretations and the ensuing workflow for uncertainty reduction. chapter 7 addresses the second part of the study, in which GEo-01 and GEo-02 and interpreted based on the suggested workflow. Chapter 8 discusses the meaning of the results and offers a reconstruction of the fracture history of the basin. It describes the limitations and uncertainties of the work and provides suggestions for future research. Chapter 9 briefly summarizes the findings.

2

Fractures

Fractures can highly influence flow in a reservoir: open fractures form pathways for fluids, whereas closed or filled fractures block flow. To make predictions of fluid flow in a reservoir, fracture models are developed that incorporate various fracture types, characteristics and include drivers that created them. Therefore, accurately measuring or estimating these fracture characteristics and drivers, is highly important in developing reliable models.

2.1. Types

Fractures are defined as mechanical discontinuities in rocks, and form when the subjected stress exceeds the strength of the rock in a brittle regime (Fossen, 2016). This stress is expressed in terms of the three principal stresses: $\sigma_1 > \sigma_2 > \sigma_3$. Depending on the orientations of the three principal stresses, rocks can open or shear, resulting in different types of fractures. In this way, certain fractures are reliable indicators of the paleostress orientations.

Figure 2.1 shows various fracture types concerning the three principal stresses. Extension fractures form when relative movement is perpendicular to the fracture planes. These are called **joints** if the displacement is minimal. If they are filled, these are called **fissures** (air or fluid) or **veins** (minerals). **Stylolites** are irregular, planar zones, which form by local pressure and dissolution normal to σ_1 (Fossen, 2016; Lorenz and Cooper, 2020). **Shear fractures** form where the relative movement is parallel to the fracture plane. They can appear as conjugate sets, typically 60° apart, or as **polymodal fractures**, in which three or more sets develop simultaneously (Healy et al., 2015).

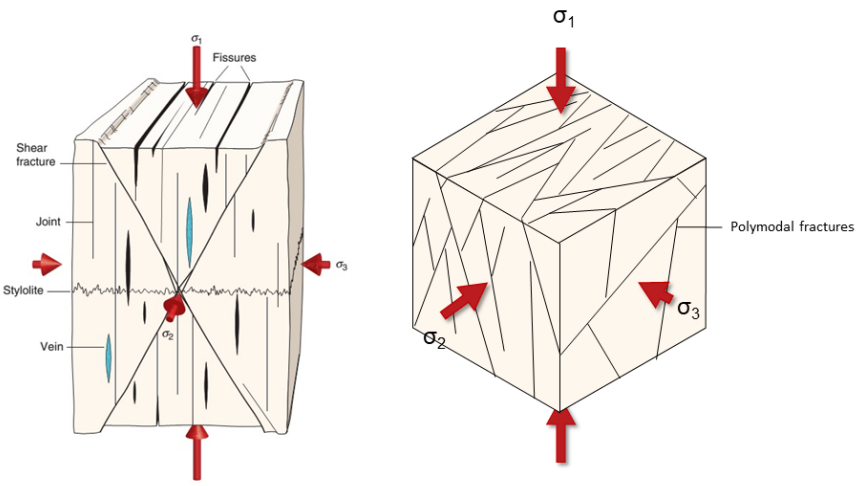

Figure 2.1: Various fracture types relative to the principle stresses (From Fossen, 2016) and the classification in Mode I-IV (modified from Healy et al., 2015).

Azimuth and dip

The dip direction and angle represent the orientation of a fracture. The orientation of the fracture may vary slightly along its length, and if a rock has been deformed, the orientation of the fracture may have changed (Lorenz and Cooper, 2020).

2.2. Drivers

The distribution of fractures can be random or show some spatial organization, either regularly distributed or forming clusters (Bistacchi et al., 2020). The more brittle beds of a formation often accommodate more fractures, but at the time of fracturing, the brittleness of the rock might have been different (Lorenz and Cooper, 2020). This change in the rocks over time may cause that the observed fracture pattern does not coincide with the current mechanical properties of a rock. To address this issue, Laubach and Olson, 2009 proposes to separate mechanical stratigraphy from fracture stratigraphy. Separating the mechanical characteristics from the fracture properties may provide a better understanding of fracture patterns and may result in more accurate predictions of fractures elsewhere.

Additionally, drivers can affect the distribution. Fractures drivers are geological processes that explain the occurrence of fractures because they (locally) alter the stress fields.

One of the main drivers of fractures is **far-field stresses** that deform the rocks on a large regional scale (Figure 2.2C). The second main driver is **faulting**, which affects the stress field locally. The effect of faults on fracture patterns is dependent on the type of fault and the in-situ stress (Blenkinsop, 2008). Shear fractures, veins, joints or stylolites form near the (propagating) fault, creating a zone with higher fracture density than the background level (Figure 2.2A) (Fossen, 2016). Another main driver is **folding**, creating a variety of patterns in the hinges and limbs caused by local deflections of the stress field. The patterns vary in orientation, connectivity, and permeability and are dependant on a fold's curvature, lithology, and location on the fold (Figure 2.2B) (Watkins et al., 2018). Lastly, the **burial** of the rocks can form regional fractures because of the increase in vertical stress (Figure 2.2D) (Bisdom, 2016).

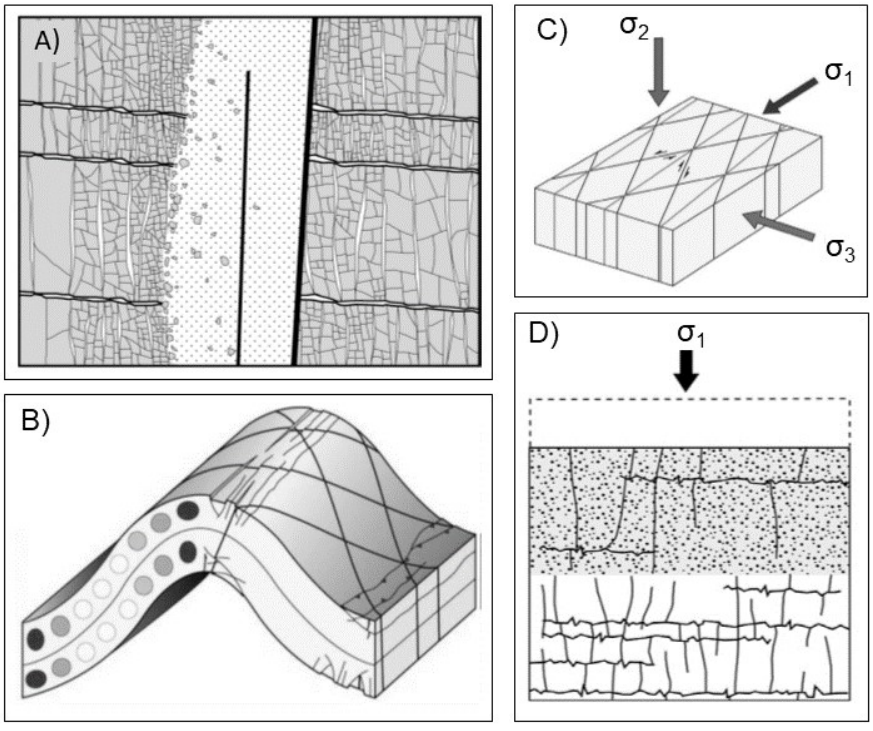

Figure 2.2: Four fracture drivers: A) fault-related fractures, B) example of a fold with its related fractures, C) far-field stress fractures, where σ2 is vertical, D) fractures related to burial. Modified from A) Billi et al., 2003, B) Ahmadi et al., 2019, C) Jiang et al., 2016 and D) Lavenu et al., 2014.

3

Geological setting

The canton of Geneva is located in the Geneva Basin, which is part of the foreland of the Jura fold-and-thrust belt. The basin is bounded by the Jura mountains in the northwest and the Salève mountain in the southeast (see Figure 1.1).

3.1. Tectonic and structural history

The sedimentary succession of the Geneva Basin overlies a crystalline basement that formed during the Variscan orogeny (480-250 Ma) and is characterised by half-grabens and strike-slip faults, filled with sediments from the Permian and Carboniferous (Guglielmetti and Moscariello, 2021; Matte, 2003; Moscariello, 2019; Rusillon, 2018) as shown on Figure 3.1.

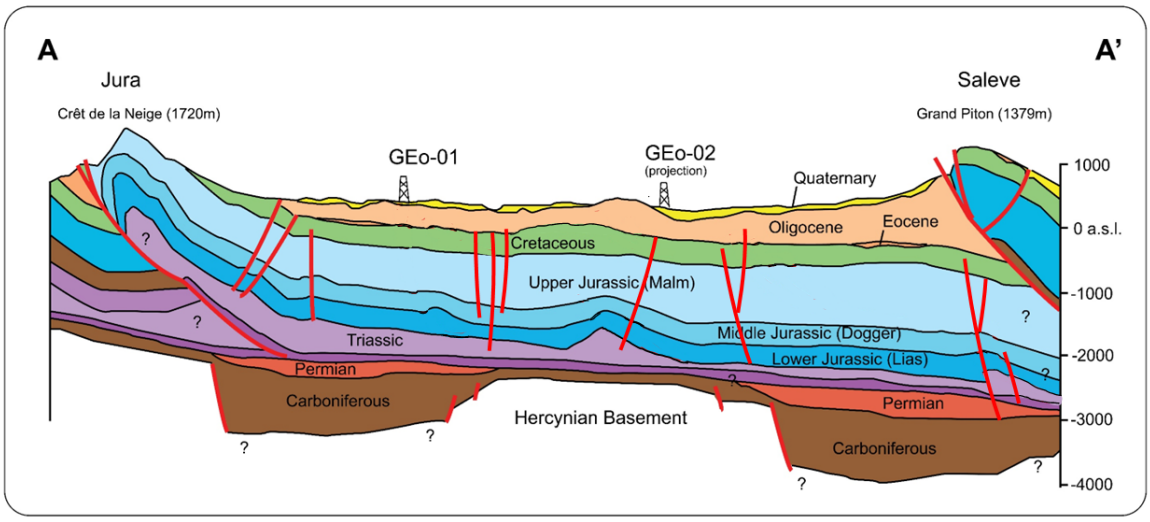

Figure 3.1: NW-SE cross-section through the Geneva Basin, showing the basement, overlying sediments and thrusting of the Jura and Salève mountains (modified from Koumrouyan, 2019; Moscariello, 2019).

The Jurassic sediments rest unconformably on top of this basement and form a thick succession of marls and limestones deposited at the northern margin of the Tethys ocean. The Alpine compression began at the end of the Mesozoic, closing the Tethys ocean and causing an uplift of the foreland basin, which is marked by a regional erosion surface on top of the Mesozoic sediments (Moscariello, 2019). This NW-SE Alpine shortening accommodated in low-amplitude folding in the Mesozoic and Cenozoic cover of the basin (see Figure 3.1) (Clerc et al., 2015; Planes et al., 2019), and an overall arc-shaped thrusting of the Alps (Sommaruga et al., 2017).

The basin is affected by four major fault systems (the Vuache, Cruseilles, Le Coin and Arve), which are basement-related normal faults reactivated as reverse faults that propagated through the overlying sediments (Figure 1.1,Signer and Gorin, 1995). The Vuache fault is a sinistral system (Clerc et al., 2015), of which the northeastern half decoupled from its southwestern counterpart, playing a role in the structuration of the basin and the distribution of the Tertiary and Quaternary sediments (Rusillon, 2018; Schori et al., 2019).

At present-day, the European plate remains subducting southward, creating a regional maximum horizontal stress in E-W to NW-SE direction. Earthquakes are not uncommon in the region and the four faults are believed to be active (Atunes et al., 2020; Clerc et al., 2015).

3.2. Stratigraphy

The Mesozoic and Cretaceous sediments form the largest part of the stratigraphic sequence, increasing in thickness towards the south. The rocks form the primary reservoir targets for geothermal exploitation and are reached by both GEo-01 and GEo-02. Moreover, these units are partly outcropping around the basin or its surrounding mountains.

3.2.1. Jurassic

The Triassic rocks are overlain conformably by the Jurassic rocks. They mark a marine transgression, with the Liassic being characterised by carbonates, marls and organic material and the Dogger by deep carbonates (Clerc et al., 2015). The environment of deposition transitioned to a more shallow marine for the Malm, characterised by shallow carbonate platforms (Moscariello, 2019). All are well observed in outcrops in the area and reached by the Humilly-2 well (Rusillon, 2018).

3.2.2. Cretaceous

The Jurassic rocks are overlain by the Cretaceous deposits, which are the focus of this study and shown in detail in Figure 3.2. Both the GEo-01 and GEo-02 well reach the succession, and the rocks are exposed in the nearby Jura Mountains. They are typically composed of massive limestones and marls, deposited in a shallow marine environment subjected to small-scale sea level fluctuations. The descriptions below are based on the work of Haas et al., 2022, Strasser et al., 2016 and Chablais and Rusillon, 2017, 2019. Only formations that are covered by the GEo-01 and GEo-02 image logs are described in detail.

Goldberg Formation

This formation is Early to Middle Berriasian in age and is characterised by massive dolomites to limestones, alternated with marls. A wide range of facies is associated with the deposits, which are hypersaline, brackish, lacustrine, tidal-flats, beaches, lagoons and shoals. Thicknesses vary from 5 to 30m. Only GEo-02 covers this formation.

Pierre-Châtel Formation

The transition from the Goldberg to the Pierre-Châtel formation is marked by a sharp transgressive surface. Oolitic and bioclastic limestones are typical for this formation, which varies in thickness from 14 to 42m. The associated environments are subtidal dunes with intervals of lacustrine and lagoonal deposits. Locally, this formation has been karstified. The formation is only covered by GEo-02 and not by GEo-01.

Vions Formation

This formation is comprised of marls and limestones with presence of quartz, iron oxides and organic material, with common traces of bioturbation and plant remnants. Thicknesses are around 40 to 50m and only GEo-02 covers this formation.

Chambotte Formation

The Late Barriasian Chambotte formation is characterised by massive limestone beds with ooids and bioclasts, representing a shallow marine environment. The thickness ranges from 10 to 25m. The formation is fully covered by GEo-02 and the bottom 3m of GEo-01.

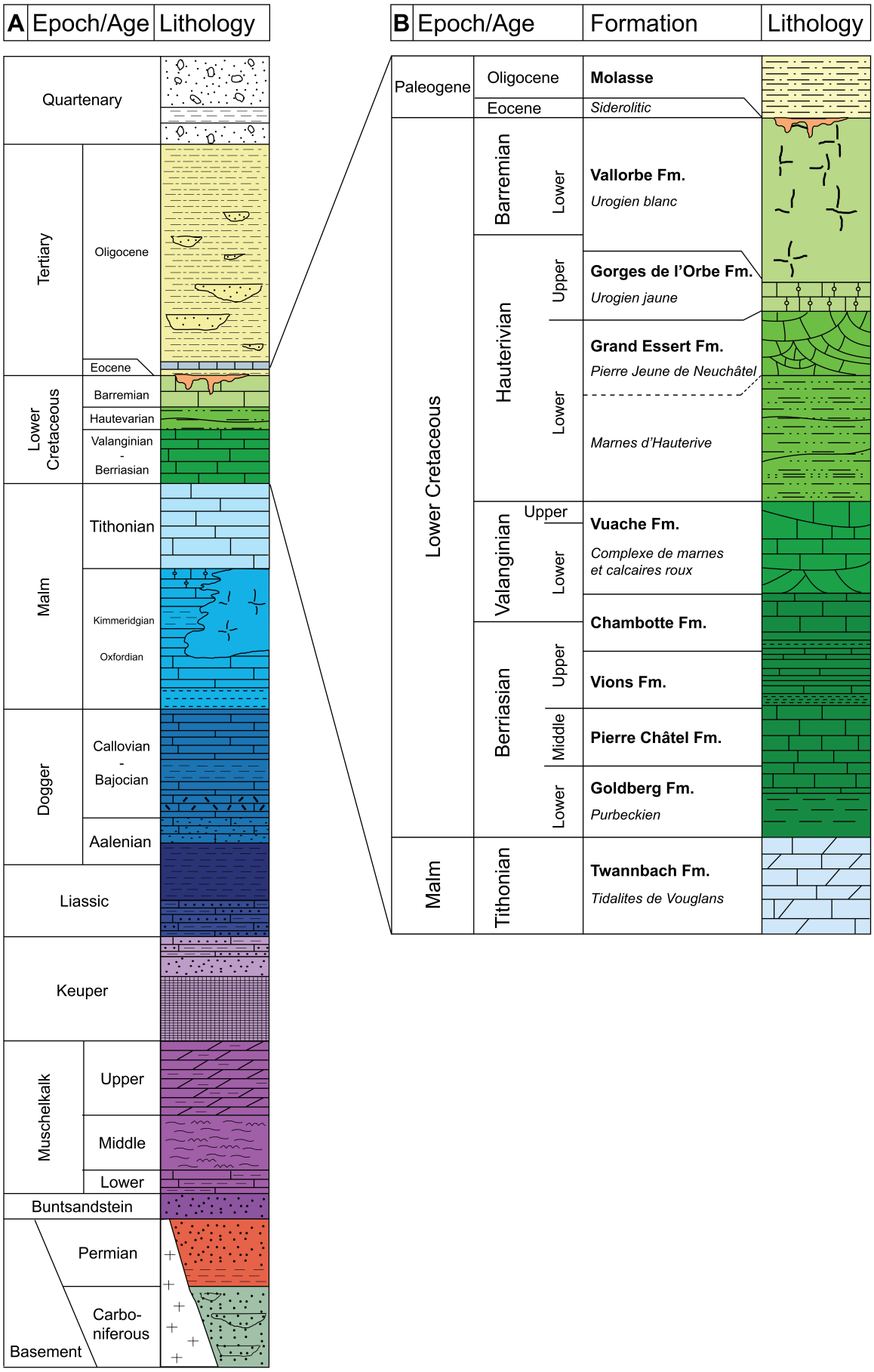

Figure 3.2: Stratigraphic column of A) the basin and B) the Cretaceous rocks (modified from Moscariello, 2019 and Rusillon, 2018).

Vuache Formation

This formation is Valanginian in age and comprises reddish sandy to marly limestones that got deposited in an open shelf. Its thickness ranges from 10 up to 60m. In places, it shows hummocky crossbedding, oolite grainstones and ammonites. The formation is covered by both GEo-01 and GEo-02.

Grand Essert Formation

Two members are associated with this formation: the *Marnes d'Hauterive* and the *Pierre Jeune de Neuchâtel*. The former is the lower member and is a fossil-rich limestone alternated with quartz-rich marls, which have been deposited in an open-marine environment without the influence of waves and tides. The latter is the upper member and is typed by cross-bedded limestones. Tidal currents strongly influenced these deposits, as indicated by the sedimentary structures. Both the members are rich in fossils and the total thickness ranges from 20 to 90m. Both wells cover this formation.

The Cretaceous includes two more formations: the Gorges de l'Orbe Formation and the Vallorbe de l'Orbe Formation. Both are characterised by limestones and marls. However, these are not covered by the image logs of GEo-01 or GEo-02.

The top of these Lower Cretaceous sediments is marked by a major subaerial erosional surface, but it is believed that the small-scale sea-level fluctuations prevailed during the Early Cretaceous, depositing limestones and marls (Moscariello, 2019 and Moscariello et al., 2020). However, during the Eocene, the Alpine orogeny caused an uplift of the basement. The rocks exhumed, got eroded and their presence is nowadays only recognised in the infill of karst structures (Du Couto et al., 2021 and Moscariello et al., 2020).

3.3. Geothermal setting

Over the past years, the geothermal potential of the Geneva Basin has been evaluated extensively. The recent work of Chelle-Michou et al., 2017 shows the basin has a geothermal gradient of 25-30◦C/km, which is suitable for direct heat use or electricity generation. Their subsurface models show various positive and negative anomalies, indicating subsurface fluid circulation, driven by the recharge from the neighbouring Jura Mountains (Guglielmetti and Moscariello, 2021 and Driesner, 2021).

The Upper Jurassic and Lower Cretaceous units form the primary reservoir targets for the GEothermie2020 project. For most of the Jurassic rocks, primary porosity (ϕ in %) and permeability (K in mD) are relatively low, with values between 2 - 5% and 0.01 - 10 mD respectively. The same applies to the Lower Cretaceous rocks, with ϕ <8% and K 0.001 - 10 mD. Additionally, the Cretaceous rocks have high lithological variability due to the different sedimentological environments.

However, secondary porosity and permeability from fracture networks could account for better conditions in these units. Flow rates from the Lower Cretaceous reservoirs in GEo-01 show values of 50 l/s at 34◦C (Moscariello, 2019), which is sufficient for the development of geothermal heat.

4

Data

4.1. Well data

Four exploration wells were planned to be drilled by the SIG and UNIGE as part of the GEothermie2020 project. The first well, GEo-01, finished in 2018 and reached the top of the Chambotte Fm. with a depth of 533 m(MD). The second well, GEo-02, finished in 2020 and reached the top of the Upper Jurassic rocks with a depth of 1455 m(MD) (see Figure 1.1 for the locations). Image logs and geophysical data are obtained for both wells, as shown in Figure 4.2. The other two wells are planned to be drilled in the upcoming years.

4.1.1. Image logs

Image logs provide a continuous 360° view of the borehole wall and are either obtained by optical borehole imaging (OBI) or acoustic borehole imaging (ABI). OBI is obtained by a camera with a light source, measuring the colour spectrum. ABI uses a rotating transductor emitting an acoustic signal that gets reflected by the borehole wall. The amplitude and transit time of the reflected signal are recorded and converted into two separate images (J.H.Williams and Johnson, 2004) and are used to generate a caliper log. Examples of each image log are shown in Figure 4.1.

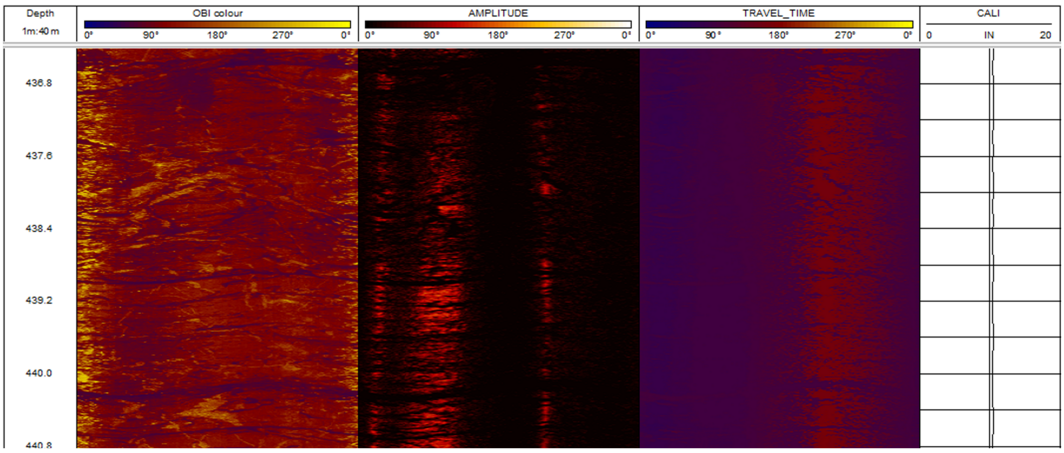

Figure 4.1: Available image logs for GEo-01: OBI, Amplitude and Travel-time. A caliper log is generated from the ABI logs.

Borehole image data is indispensable in the energy industry and form the standard for fracture analysis in many projects. Image logs provide reliable and direct data on subsurface fractures, cover large intervals and processing software are well established (Lorenz and Cooper, 2020). Running an image log might be favoured over drilling a core, since it is faster, hence less expensive.

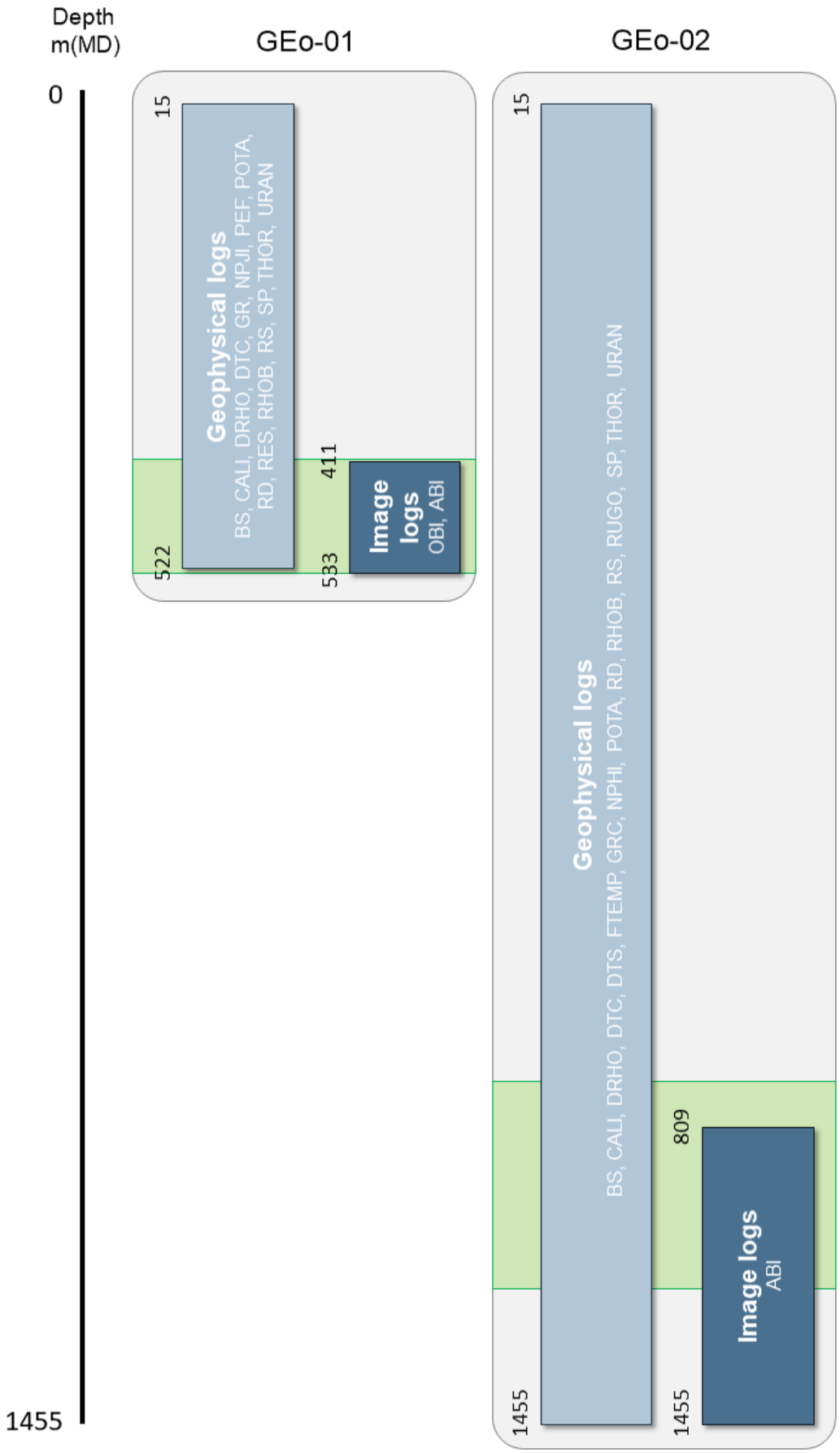

Figure 4.2: All available geophysical and image logs with according depth intervals for GEo-01 and GEo-02. The green intervals indicate the Cretaceous rocks, according to the two lithological reports (Chablais and Rusillon, 2017, 2019).

On the other hand, the vertical resolution of image logs is generally on a mm to cm scale, which is too large to capture all fracture characteristics. Fractures parallel to the wellbore could be underinterpreted since they might not be represented in the well. Additionally, bedding parallel fractures are difficult to distinguish from bedding and might be misinterpreted (Lorenz and Cooper, 2020). chapter 6 addresses these and a number of other issues related to the interpretation of image logs.

4.1.2. Geophysical logs

Geophysical logs include caliper, bulk density, sonic, Gamma Ray, photoelectric factor, resistivity, bulk density, and spontaneous potential. These logs are not the main focus of the study but are used in software settings and complementary to the fracture-picking process.

4.2. Available interpretations

In addition to the raw well data, various interpretations are available online or were provided by the UNIGE/SIG: including lithological reports for both wells (Chablais and Rusillon, 2017, 2019) and four fracture interpretations from GEo-01 (by the SIG, Jorge, 2022; Koumrouyan, 2019; Lo, 2019). The fracture interpretations hold each interpreter's fracture picks and classification and are available either in WellCAD or as a text file.

4.3. Seismic data

Two seismic lines are available, nearly crossing GEo-01 (pink lines in Figure 1.1). The first is called GG-87-02 and runs NW-SE for 3.7km. The second is called SIG-2015-L08 and runs NE-SW for 5.6km.

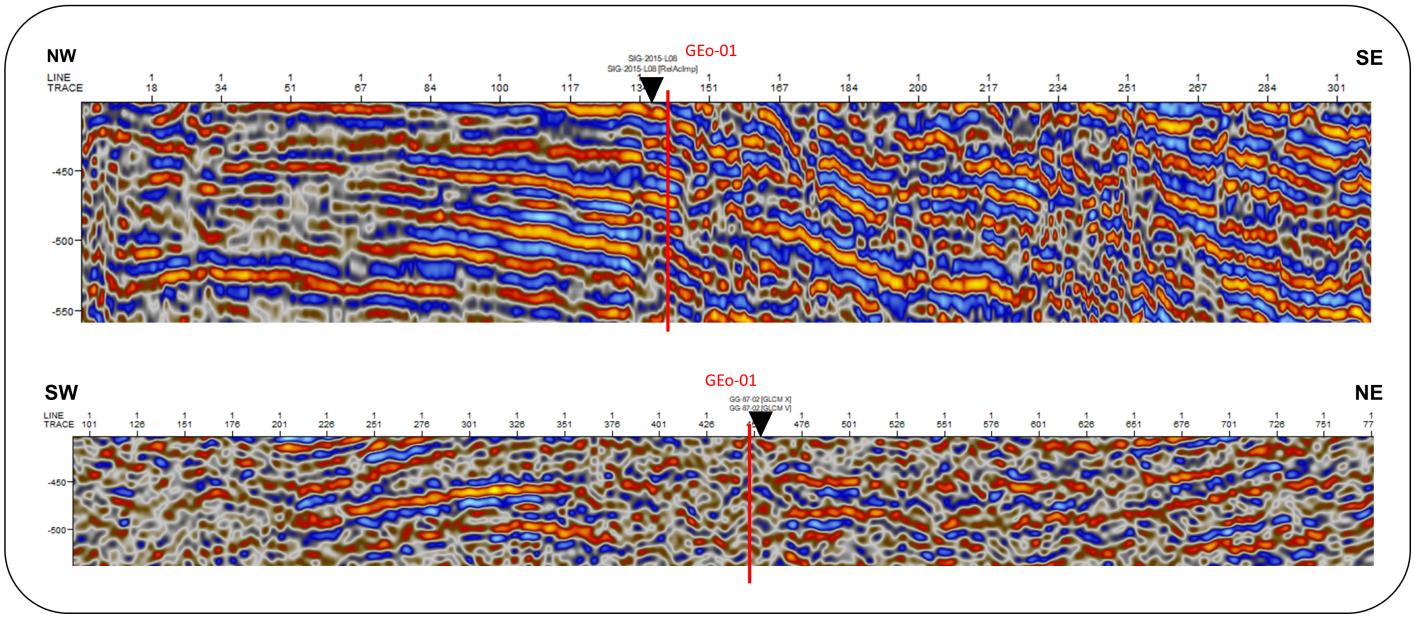

Figure 4.3: Two seismic lines, running NW-SE and NE-SW. The red line indicates the location of GEo-01 and the black triangles indicate the location of the other seismic line.

5 Methods

5.1. Workflow

Figure 5.1 presents the workflow and results of the project. It consists mainly of two phases:

1. a **statistical analysis** on interpretations from GEo-01, resulting in recommendations for fracture picking;
2. a fracture analysis of GEo-01 and GEo-02 and **correlation to the geological history** of the basin.

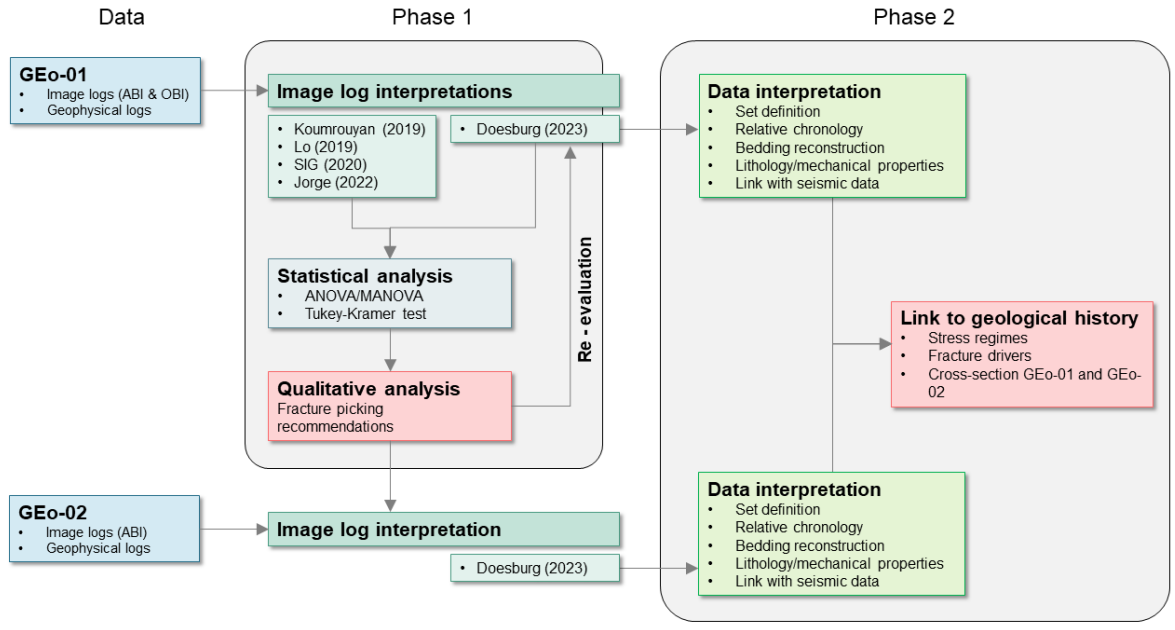

Figure 5.1: Workflow of the project.

For this study, a new fracture interpretation of GEo-01 was performed. This new interpretation and the four pre-existing interpretations provided input for the statistical analysis of phase 1 to investigate the differences amongst interpreters. Based on the results from this analysis, a list of recommendations for fracture picking was created to reduce uncertainties in interpretation. Consequently, the interpretation of GEo-01 was re-evaluated, and GEo-02 was interpreted following these recommendations.

In phase 2, the optimized fracture data from GEo-01 and GEo-02 were analyzed to define sets, and determine possible fracture drivers and successive tectonic regimes. Based on the drivers, tectonic regimes, cross-section, and literature, the fracture history of the basin could be reconstructed.

5.2. Fracture picking in WellCAD

Fracture interpretations were executed in WellCAD. The first step was to prepare a workspace, and the second step was to manually identify all structures (referred to as picking). Picks can be displayed as sinusoids on the image logs, planes in a 3D borehole view, or tadpoles indicating the dip angle and direction (Figure 5.2). The colour palette and amplitude/travel-time scale could be adjusted to modify the image log and highlight different structures.

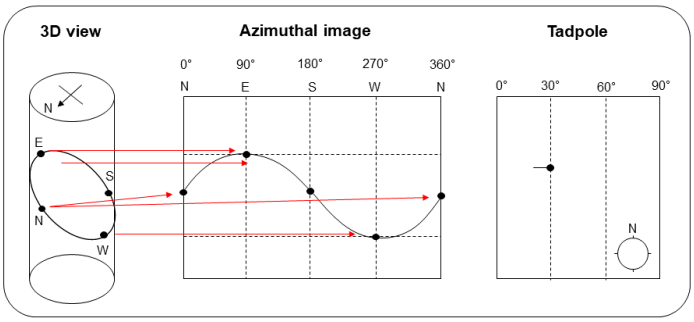

(a)

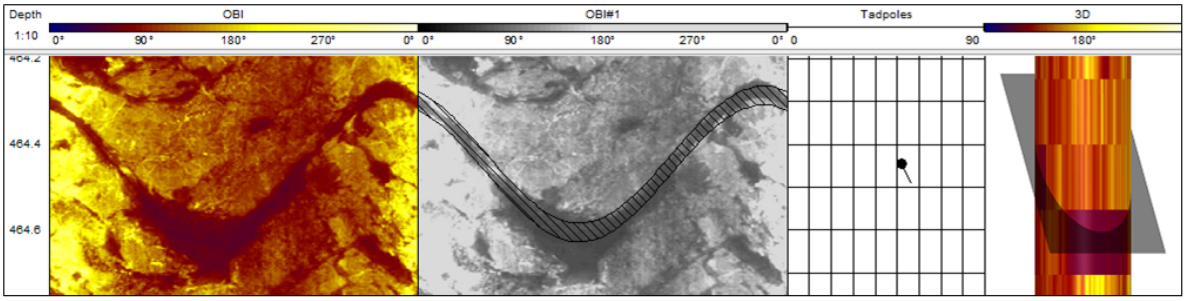

(b)

Figure 5.2: (a) 3D planes represented as sinusoids on an image log striking N-S, dipping 30° towards the west, modified from Serra, 1983. (b) Examples of GEo-01: sinusoid, tadpole, and 3D representation of a structure.

The next step was to assign a classification to each pick. The classification of fractures on image logs is based on the morphology of electric or acoustic properties, rather than mechanical markers or displacement indicators (such as striation in the field). Figure 5.3 lists the five structure categories used in this study, the observational criteria, and examples from GEo-01. Mineralized fractures appear reflective/bright on an OBI and to not show on the ABI logs. Open/shear fractures appear transmissive/dark on the OBI and are low amplitude/dark on the Amplitude log. Bedding can appear both reflective and transmissive on the OBI, depending on the deposited material. It is mostly shallow dipping (<20°) and repetitive or gradually changing over large intervals. The induced fractures appear transmissive/dark on the OBI and are low amplitude/dark on the Amplitude log. They often appear irregular and asymmetric, with high dip angles. A fifth category was created for structures that could not be classified with confidence.

The bedding picks were used to identify sub-seismic scale folds and faults, and to create local reconstructions of the subsurface. These reconstructions, in combination with fault observations from the image logs, lithological reports, the seismic lines and previous work (Lo, 2019; Moscariello, 2019), were incorporated into a new NW-SE cross-section between GEo-01 and GEo-02.

The fracture picks were corrected for the dip angle of the bedding: so-called backtilting, with the average bedding orientation per meter. Fracture sets were defined, based on clusters on the stereonet, common displacement observations on the image logs and indications on relative chronology. Initially, all data were plotted as a pole on a stereoplot using the Stereonet software. Fractures dipping <10° were excluded from the database because the orientation of such shallow dipping planes has a high level of uncertainty. Outliers (fractures with non-recurring orientations) were removed manually. In the next step, contours were generated on the stereoplot by Stereonet, representing the density of fracture orientations. Clusters of local maxima were identified based on the contours. This was done manually, and boundaries approximately followed the shape of the contours. These clusters were then compared to observations of displacement and relative chronology on the image log, leading to the definition of fracture sets. Due to the scarcity of observations regarding displacement and chronology, it is assumed that fractures with comparable orientations experienced similar displacements. The sets are taken as indicators for paleostress orientations as described in chapter 2.

Lastly, a cross-section was created to capture the basin's structural elements like folds and faults. The results of the bedding picking, fault observations on image logs, lithological reports, the seismic lines and previous work (Lo, 2019; Moscariello, 2019) were incorporated into a NW-SE oriented cross-section between GEo-01 and GEo-02.

Structures	Observation criteria
Open/shear fracture or joint	• Transmissive (dark) on OBI • Low amplitude on Amplitude log
Mineralized fracture or vein	• Reflective (bright) on OBI • Not visible on Amplitude log • Not visible on Travel-time log
Induced fracture	• Transmissive (dark) on OBI • Low amplitude on Amplitude log • High angle (>85°) • Often asymmetric shape

Bedding	• Transmissive or reflective (dark or bright) on OBI, depending on the material
	• Dip angle related to the regional dip angle
	  • Often low dip angle (<20°)
	  • Repetitive, or a gradual change in dip direction
	• Cannot cross-cut any other structure

Not classified	If a pick could not be classified with confidence or did not met any the criteria of any other structure

(a)

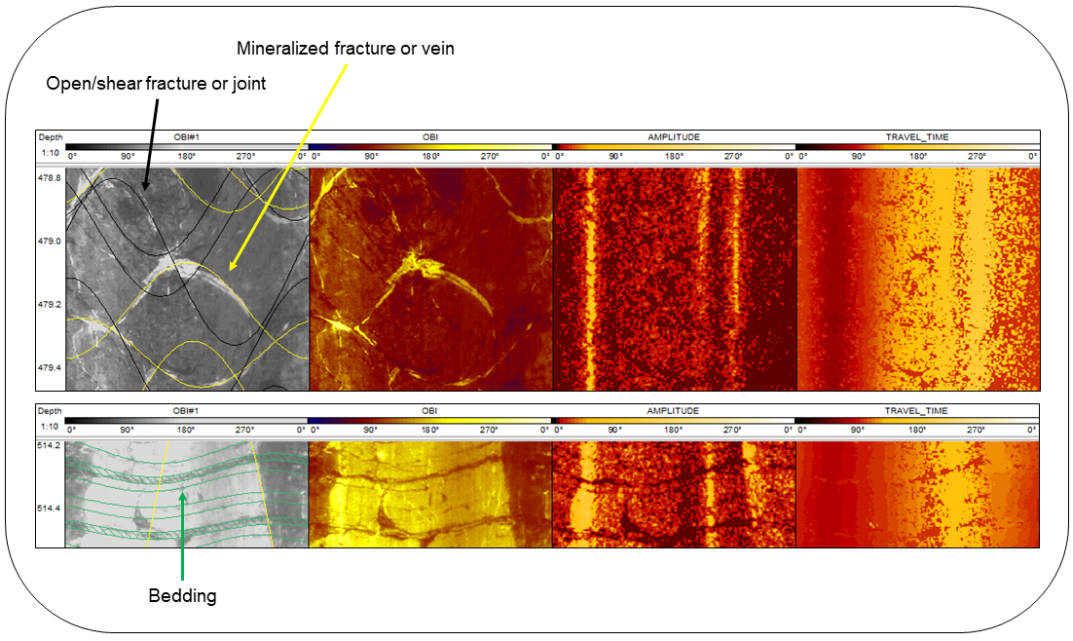

(b)

Figure 5.3: (a) Classification of structures and the criteria for picking on image logs. (b) Workspace in WellCAD of GEo-01. Left to right: OBI with examples of 'open/shear fractures or joints' (black), 'mineralized fracture or vein' (yellow), and 'bedding' (green), OBI, amplitude log, travel-time log.

5.3. Statistical analysis

Statistical analysis compared five fracture interpretations of GEo-01 and highlighted similarities and differences. The workflow of this analysis is presented in Figure 5.4.

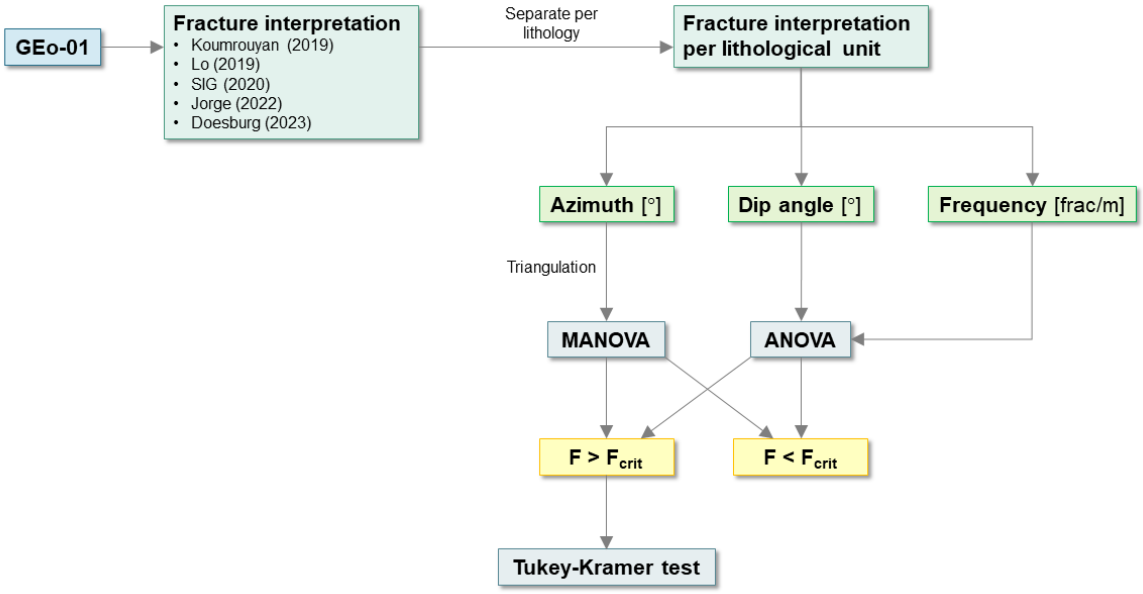

Figure 5.4: Workflow of the statistical analysis.

5.3.1. Data separation

In order to highlight the effect of mechanical rock properties on interpretations, the data was subdivided into intervals based on the lithological description of Chablais and Rusillon, 2017 (see Table 5.1). Additionally, fractures and veins were considered separately in this analysis to highlight the difference in picking of various structures. Fractures that were classified as induced fractures were diverted from the dataset since this study focuses on natural fractures.

Table 5.1: Subdivision of GEo-01, based on the lithological report of Chablais and Rusillon, 2017. The table gives the tags used in this report (A - O), the corresponding depth, formation, and a brief lithological description.

Tag	Depth [m]	Formation	Description
A	412 - 414	Urogien Blanc	**Bioclastic limestone**, recrystallised, pyrite
B	414 - 423	Urogien Blanc	**Bioclastic to oolithic limestone**, recrystallised, crushed, calcite veins
C	423 - 427	Urogien Blanc	**Peloidal bioclastic limestone**, oolithic, fine sand, pyrite and glauconite
D	427 - 432	Pierre Jeune	**Bioclastic lime- to sandstone**, pyrite and glauconite, **marl- to sand intervals**, completely crushed
E	432 - 453	Pierre Jeune	**Bioclastic lime- to sandstone**, pyrite and glauconite, calcite veins, **intervals of marl- to sand**
F	453 - 456	Marnes d'Hauterive	**Marls and sandstones**, pyrite
G	456 - 458	Marnes d'Hauterive	**Marls and sandstones**, pyrite and glauconite
H	458 - 460	Marnes d'Hauterive	Fine **limestone with sand**, pyrite and glauconite, **sand- to marl intervals**
I	460 - 475	Marnes d'Hauterive	Alternation of **fine marly limestones and sandstones**
J	475 - 480	Marnes d'Hauterive	Bioclastic limestone, marl- to sand with biodetrics, pressure vein-fissures
K	480 - 495	Marnes d-Hauterive	**Marly limestone with sand**
L	495 - 512	Marnes d'Hauterive	**Sandstone marls** to marly sandstones, **intervals of bioclastic limestone** with sand, filled fractures
M	512 - 516	Marnes d'Hauterive / Vuache	Marly to sandy limestone, bioclastic limestone, recrystallised, oolithed debris, calcite veins
N	516 - 526	Vuache	**Oolithic limestone**, pyrite, bioclastic (grainstone) limestone
O	526 - 533	Vuache / Chambotte	**Bioclastic limestone**, fractures

5.3.2. ANOVA and MANOVA

ANOVA (Analysis of Variance) and MANOVA (Multivariate Analysis of Variance) methods have been used in this study. These are statistical methods to determine if there is a significant difference in means between several groups, in this case, the interpreters. Two hypotheses were tested:

- null hypothesis: there is no difference in the means of all interpreters;
- alternative hypothesis: the mean of at least one interpreter is significantly different.

To perform ANOVA or MANOVA, a minimum of 10 data points is required, and a significance level (denoted as α) must be defined. A value of 0.05 has been chosen, meaning there is a 5% chance of unjustly rejecting the null hypothesis. One of the outcomes of the ANOVA and MANOVA tests is the P-value. If the P-value is larger than α, the null hypothesis cannot be rejected, and there is no difference in group means. If the P-value is smaller than α, the null hypothesis is rejected, meaning at least one group significantly differs from the others. ANOVA is applied if only one independent variable is present, while MANOVA is applied if more than one independent variable is present. Appendix A shows the calculations for each method in detail.

The ANOVA and MANOVA methods were performed on each fracture characteristic separately:

- **Azimuth:** the azimuth is a circular measurement (where 360° is the same as 0°, or North). However, the ANOVA method does not account for that since it assumes a linear scale. Hence, the azimuth values were converted to x and y values using trigonometry, resulting in two independent variables instead of one and MANOVA could be applied (Figure 5.5, Landler et al., 2022);
- **Dip:** ANOVA was performed on the dip of the fractures and veins;
- **Frequency:** ANOVA was performed on the frequency per meter.

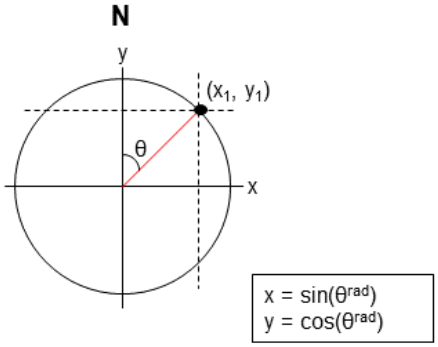

Figure 5.5: Trigonometric conversion from an angle to two linear points, modified from Jammalamadaka, 2001.

5.3.3. Tukey-Kramer test

ANOVA and MANOVA highlight if one interpreter significantly differs from the others, but the analyses do not provide information on which interpreter(s) differ(s) from the others. If the null test gets rejected, post hoc tests are generally performed to identify which interpreter(s) differ. The Tukey-Kramer test was used in this study to test every pairwise combination of interpreters. A P-value for every possible combination of pairs was calculated. A P-value smaller than α means the two interpreters are statistically significantly different. The results indicate which pair of interpreters agree or disagree with each other per given interval and are presented in chapter 6.

5.4. Qualitative analysis

A qualitative analysis was performed to explore the relationship between the results of the statistical analysis and various factors, including the quality of the image logs, rock properties, methodology/software usage, or a combination of those.

The analysis began by examining the differences between interpreters in terms of classification, orientation and frequency. Some findings were specific to certain intervals, while others were consistently observed. For interval-specific observations, a detailed investigation was conducted, considering the quality of the image log, the classification of structures and geomechanical properties, to identify possible relationships. In cases where findings were identified across multiple intervals, a closer examination was carried out to understand the workflow of all interpreters and the classification scheme they used. This approach allowed to find relationships between interpretations, the image log, rock properties and methodology/software usage. The results of these analyses were incorporated into a list of recommendations and a workflow for fracture picking from image logs.

6

Comparison of five interpretations

The first part of the objective of this study is to reduce uncertainties in fracture interpretation. Utterly unique, five fracture interpretations, executed by five different people, are available from one dataset (GEo-01), making it possible to analyze differences between interpretations statistically. This chapter presents the five interpretations, the results from the statistical analysis and the list of recommendations.

6.1. Five interpreters

Figure 6.1 presents an overview of the five interpretations. For the statistical analysis, it was necessary to restructure the classification schemes from all interpreters, to enable a fair comparison.

Koumrouyan, 2019 used WellCAD and classified a structure based on its visibility on the OBI, ABI or both. The study picked 803 open/shear fractures and 161 mineralized fractures. The bedding was defined during a second phase and counted 261 picks. The **SIG, 2020** used WellCAD and picked 573 open/shear fractures, 73 mineralized fractures and did not pick any bedding. **Lo, 2019** used Techlog, unlike the other four. Since Techlog was not available during this study, the picking data was converted and processed as text files. Lo, 2019 picked 406 open/shear fractures and 152 mineralized fractures. The bedding was not manually picked, but defined based on orientation, which resulted in 488 bedding picks. **Jorge, 2022** used WellCAD, revising the picks from Koumrouyan, 2019. A total of 460 picks were removed and the remaining part was reclassified into 377 open/shear fractures and 127 mineralized fractures. **Doesburg, 2023** (this study) used WellCAD and picked 607 open/shear fractures, 213 mineralized fractures, 195 bedding and 15 others.

Interpreter	Software	Open/shear fracture		Mineralized fracture		Bedding		Other	
M. Koumrouyan (2019)	WellCAD	Fracture traversante non-marquee Fracture traversante marquee Fracture non-traversante non-marquee Fracture non-traversante marquee	85 273 55 131	Vein traversante Vein non traversante	79 82	Bedding	261		
K. Lo (2019)	Techlog	Fault Open fracture Sealed fracture	31 374 1	Cemented fracture Vein	1 151	Bedding	488		
Services Industriels de Genève (SIG) (2020)	WellCAD	Fracture ouverte Fracture traversante Fracture non traversante	14 547 12	Fracture avec remplissage minéralisé	73				
S. Jorge (2022)	WellCAD	Fracture traversante non-marquee Fracture traversante marquee Fracture non-traversante non-marquee Fracture non-traversante marquee	69 219 29 60	Vein traversante Vein non traversante	72 55				
This study (M. Doesburg (2023))	WellCAD	Open/shear fracture or joint	607	Mineralized fracture or vein	213	Bedding	195	Induced fracture Undefined	4 11

Figure 6.1: Overview of the five interpretations: used software, subdivision into the four categories (open/shear fracture, mineralized fracture, bedding, and other), the number of picks, and colour codes used in the report.

6.2. Differences in interpretations

Stereoplots and frequency plots of all five interpretations are shown in Figure 6.2 for open/shear fractures and Figure 6.3 for mineralized fractures. From a first-order analysis, some key differences among the interpretations emerge.

The number of open/shear fracture picks ranges from 378 (Jorge, 2022) to 607 (Doesburg, 2023) and of mineralized picks from 73 (SIG, 2020) to 213 (Doesburg, 2023). Notable, Doesburg, 2023 and Koumrouyan, 2019 classified 195 and 216 structures as bedding, respectively. While the other three interpreters initially did not classify any structures as bedding. Lo, 2019 defined bedding during a later stage, based on a dip angle below 43.0° and related to a fold, which resulted in 488 bedding picks. It is striking that these picking counts are relatively far out and that two out of five interpreters have not interpreted any bedding. Especially the interpretation of bedding is crucial in the identification of sub-seismic scale folds and faults, which can be possible fracture drivers.

In general, all stereoplots in Figure 6.2 show dipping directions towards the SE. However, dip angles of Lo, 2019 and Jorge, 2022 are overall higher compared to the other three interpreters. Moreover, the stereoplot of Lo, 2019 shows one main fracture cluster dipping SE; although the stereoplots of Koumrouyan, 2019 and SIG, 2020 show two main clusters dipping S and NE and the stereoplots of Jorge, 2022 and Doesburg, 2023 show three and five clusters, respectively. Similar trends are recognised in the mineralized fractures (Figure 6.3). The general dip direction of the mineralized fractures is towards the NW, still Lo, 2019 and Jorge, 2022 show higher overall dip angles compared to the other three interpreters. The stereoplot of Lo, 2019 shows one main cluster, while the stereoplots of the others show multiple clusters. All these differences in stereoplot projections represent a wide variety in fracture orientations, and thereby presumably different stress regimes. Furthermore, stereoplot clusters can represent fracture sets. Therefore, these stereoplot clusters are likely to lead to different set definitions by each interpreter.

Large differences show in open/shear fracture frequency (Figure 6.2), especially between 418-435m, 493-498m and 513-518m. On the contrary, all interpreters have high fracture frequencies between 490-493m and 528-533m and low frequencies between 413-418m, 435-438m and 493-498m. For the mineralized fracture frequency (Figure 6.3), large differences in frequency are found between 443-453m and 525-533m. Overall agreement on high frequency is between 453-463m, 473-583m and 495-501m and none of the interpreters picked mineralized fractures between 413-425m and 483-493m. These differences and similarities are noteworthy and important to consider as fracture frequency is related to fracture drivers and the mechanical properties of the rock.

Given all the differences between the five interpretations, it was expected that these differences led to discrepancies in the reconstructions of the fracture history of the basin. Koumrouyan, 2019 concludes that the fractures are fault-driven, related to a flower structure intersecting the well. The findings are in line with the work of Clerc et al., 2015. Lo, 2019, on the other hand, relates the natural fractures to two tectonic events: a strike-slip event with σ_H trending ESE and a reverse regime with σ_H trending ENE. However, as already mentioned in that report, the two tectonic events do not seem to fit in the regional tectonic context. Jorge, 2022 finds a mismatch in tectonic regimes: while the fractures imply a normal regime, the faults imply a strike-slip regime. From the SIG, 2020 only the fracture-picking data set was available, without an interpretation in terms of fracture history.

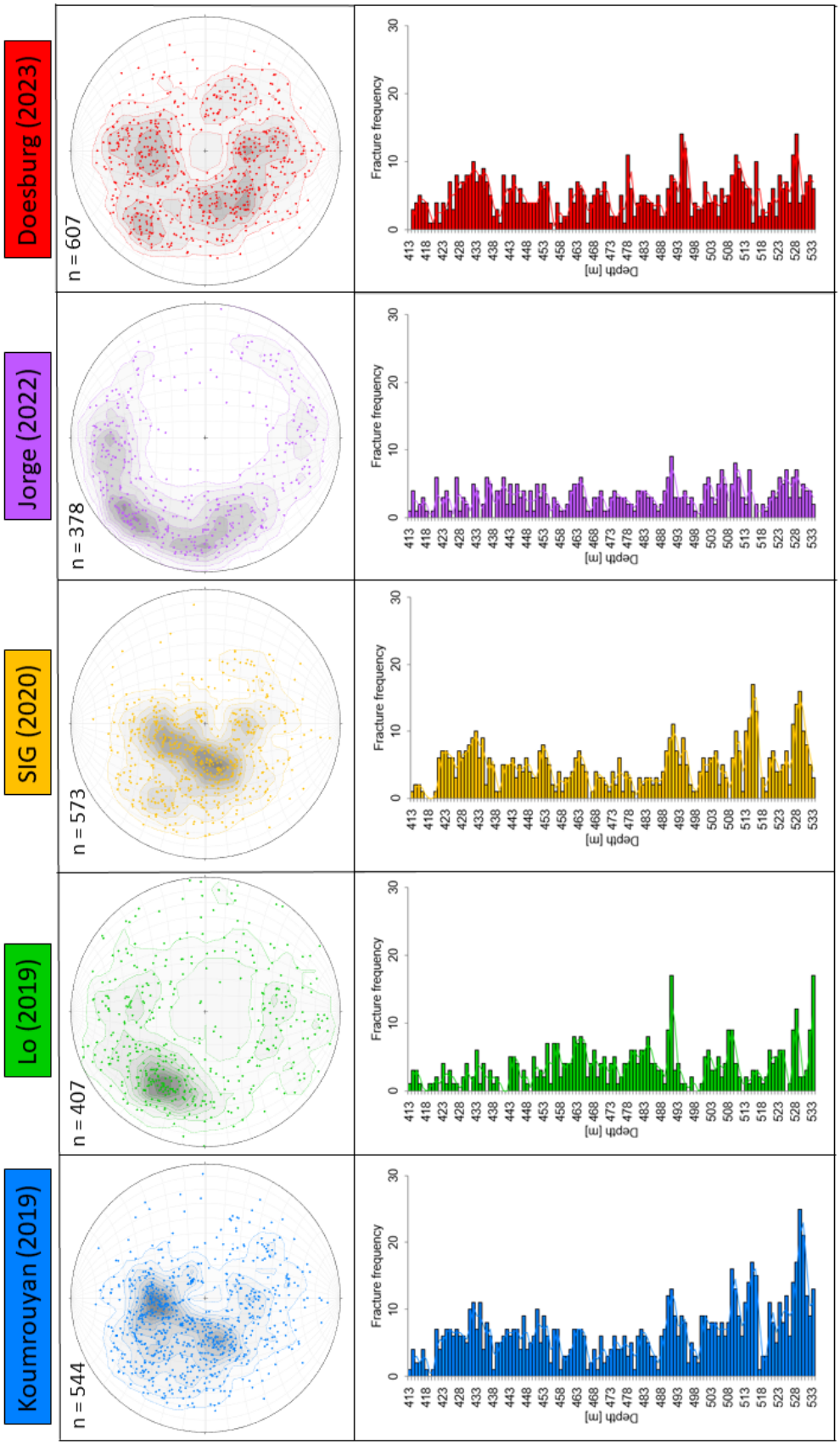

Figure 6.2: Stereoplots and fracture frequency vs. depth plots from the **open/shear fracture** interpretations.

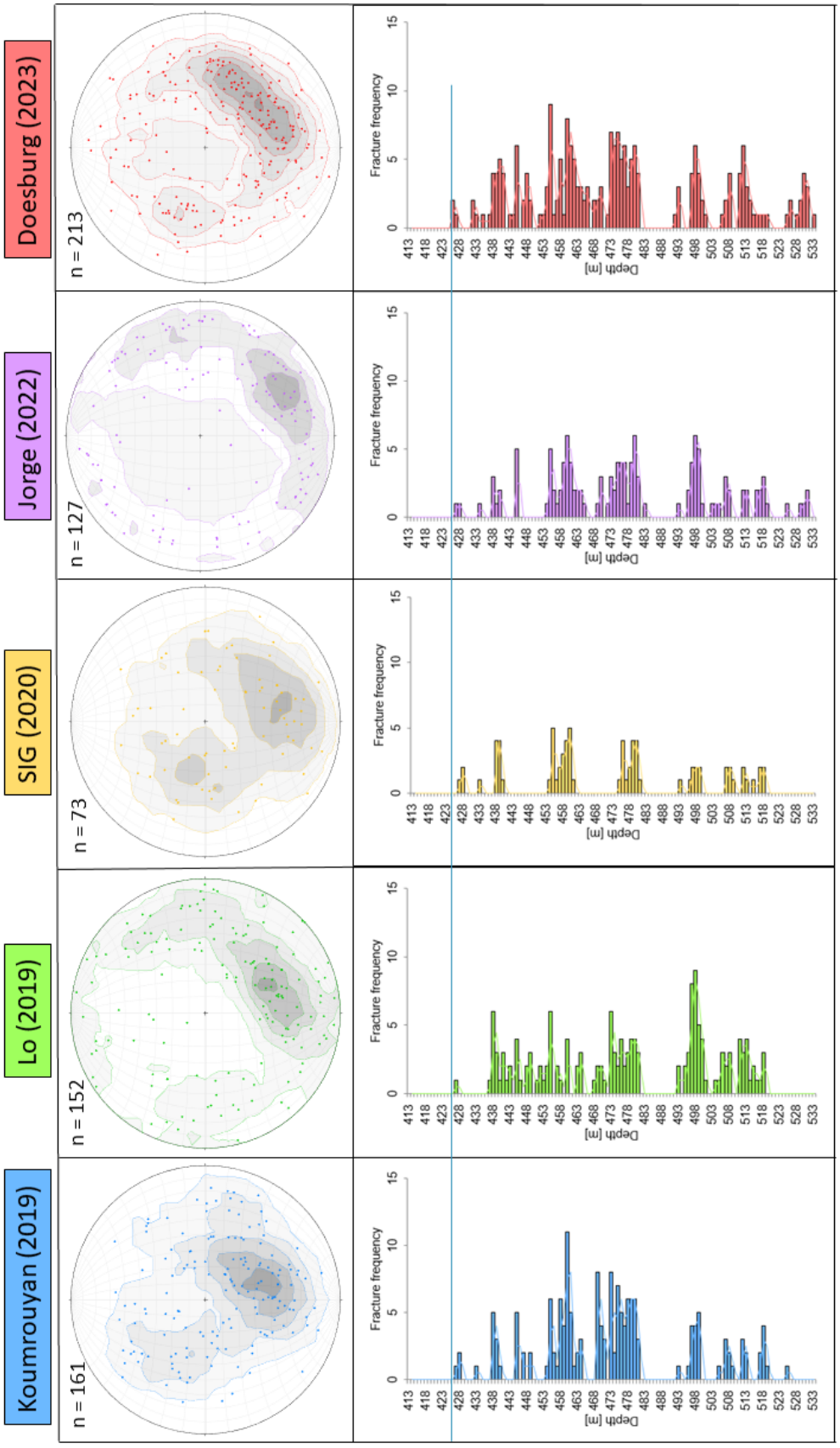

Figure 6.3: Stereoplots and fracture frequency vs. depth plots from the **mineralized fracture** interpretations.

6.3. Results statistical tests

6.3.1. ANOVA/MANOVA test

Figure 6.4 shows that overall there is more agreement in the mineralized fractures than in the open/shear fractures. However, it should be noted that for the mineralized fracture intervals A, B, C, D and O there is not enough data (NED) to perform the statistical test. This means that it is unknown whether the interpreters are in agreement or not. Alternatively, this could be interpreted as a high level of agreement between the interpreters as none of them picked any fractures in these intervals.

The **azimuth** shows the most agreement for both fracture types. All interpreters agree in 11/15 intervals for the open/shear fractures, and in 9/15 intervals for the mineralized fractures. For both the open/shear fractures and the mineralized fractures, the **dip** shows the least agreement. For the open/shear fractures, there are only 3/15 intervals where all interpreters agree in the dip. These are intervals A, G, and H. For the mineralized fractures in only 2/15 intervals, all interpreters agree on the dip. These are M and N. For **frequency**, all interpreters agree in 7/15 intervals for the open/shear fractures, and in 9/15 intervals for the mineralized fractures.

Least agreement in all three categories (azimuth, dip and frequency) is found in intervals D, E, L and M. A first-order analysis does not show any correlation to the OBI, complexity map, lithology or stiffness (Alhamad, 2021).

The thickness of the interval does not seem to influence the results of the statistical analysis. An example is interval M; showing much disagreement in the open/shear fractures, but much agreement in the mineralized fractures.

6.3.2. Tukey-Kramer test

The high level of agreement in **azimuth** is confirmed by the graphs in Figure 6.5. Between each possible interpreter pair, the thick green lines in the star diagram represent a high level of agreement. Moreover, the percentages in the tables show that each pair agrees for at least 80% of the intervals in the open/shear fractures and at least 90% in the mineralized fractures.

On the contrary, the **dip** shows very little agreement for both the open/shear fractures and the mineralized fractures. The thin red and orange lines in the star diagrams represent a low level of agreement. In particular, Lo, 2019 and Jorge, 2022 show high disagreement with the other three interpreters. As denoted in the table, Lo, 2019 agrees for 40-70% of the intervals and Jorge, 2022 agrees for only 20-40% of the intervals. On the other hand, the level of agreement between the two is much higher: 73% for the open/shear fractures and 100% for the mineralized fractures.

The agreement in **frequency** is different for the open/shear fractures and for the mineralized fractures, and the star diagram of the two fracture types looks dissimilar. The majority of lines are green, representing an overall high level of agreement, but several pairs are connected by orange lines, representing a low level of agreement. The tables describe that for the open/shear fractures Koumrouyan, 2019 disagree with Lo, 2019 and Jorge, 2022 in 50% of the intervals, but for the mineralized fractures, they agree in 92% and 100% of the intervals. Similarly, the SIG, 2020 and Doesburg, 2023 agree in 69% of the intervals of the mineralized fractures, but agree in all intervals of the open/shear fractures.

Combining all results from the Tukey-Kramer test, the SIG, 2020 and Koumrouyan, 2019 have the highest overall agreement with 95% of all intervals. Koumrouyan, 2019 and Jorge, 2022 have the lowest overall agreement with 67% of all intervals. Jorge, 2022 has the least agreement; 70% with Doesburg, 2023 and 75% with the SIG, 2020, but 94% with Lo, 2019.

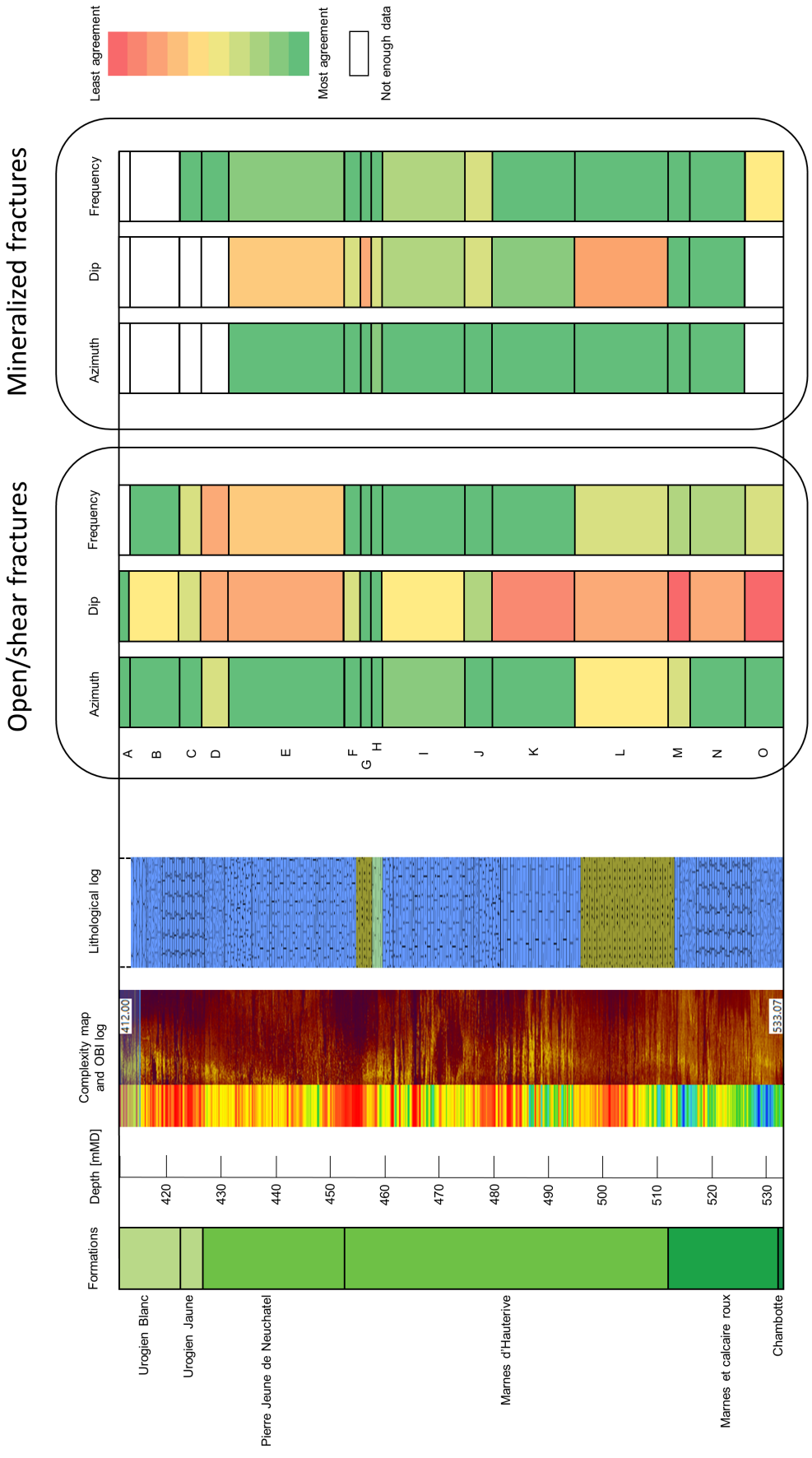

Figure 6.4: The last two columns summarize the results of the ANOVA/MANOVA tests. The color scale represents agreement among the five interpreters (red: least agreement, green: most agreement, white: NED). The first five columns give formations, depth, complexity log (generated automatically by WellCAD) and OBI, lithological log, and stiffness log from Alhamad, 2021. The letters correspond to subsection 5.3.1. Note that the red to green colors do not provide any information on who of the interpreters disagree. The detailed results of all tests are presented in Appendix A.

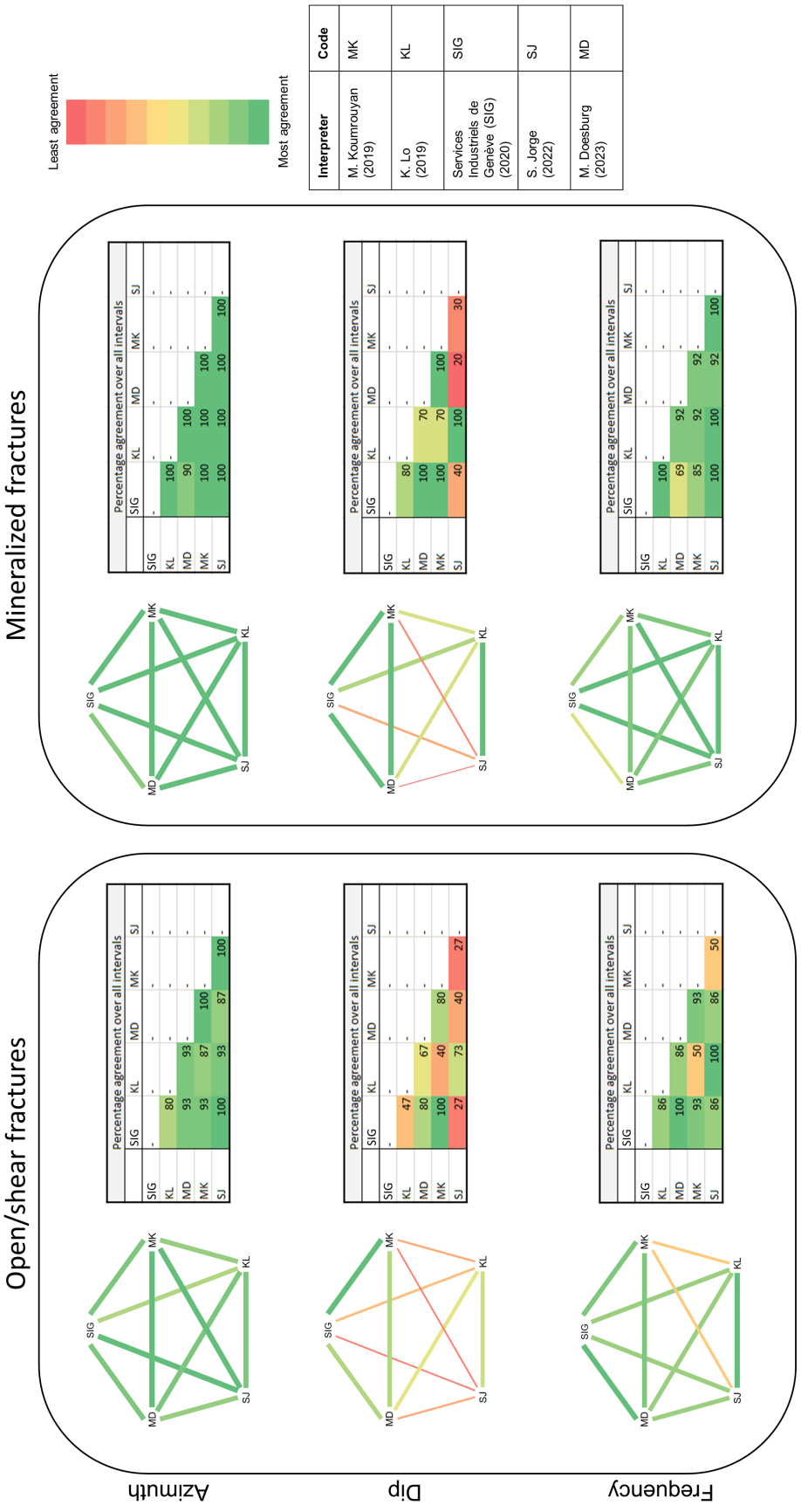

Interpreter	Code
M. Koumrouyan (2019)	MK
K. Lo (2019)	KL
Services Industriels de Genève (SIG) (2020)	SIG
S. Jorge (2022)	SJ
M. Doesburg (2023)	MD

Figure 6.5: Level of agreement between each possible interpreter pair for the open/shear fractures and the mineralized fractures. Separated by property: azimuth, dip and frequency. Note that the star diagram and table are two different representations of the same results. The numbers in the table give what percentage of intervals agree. The color scale represents agreement among the five interpreters (red: least agreement, green: most agreement). The table on the right gives the interpreters and the corresponding codes.

6.4. Qualitative analysis

This section repeats the main findings that emerge from the statistical analysis and discusses possible reasons for differences between the interpretations (see Appendix B for the detailed analysis). Screenshots from WellCAD are added as examples. Note that in these figures, all interpreters have used different colours for their classification and that Lo, 2019 is not presented because the interpretation was not available as WellCAD file.

6.4.1. Differences in frequency

Figure 6.1, 6.2 and 6.3 show that there are large differences not only in the total number of picks but also in the frequency with depth. These differences are caused by a number of reasons.

Workflow/approach of the interpreter

The use of different approaches in classification contributed to significant variations in the number of picks. Koumrouyan, 2019 and Doesburg, 2023 manually picked 261 and 195 bedding, respectively. On the other hand, Lo, 2019 initially did not define bedding but later classified 488 structures as bedding, based on their orientation. Jorge, 2022 and the SIG, 2020 did not classify any bedding.

Doesburg, 2023 and Lo, 2019 picked all structures, including non-continuous sinusoids. On the other hand, Koumrouyan, 2019; SIG, 2020 and Jorge, 2022 included the continuity of sinusoids in their classifications, distinguishing between continuous and non-continuous structures. This difference in approach resulted in different picking numbers.

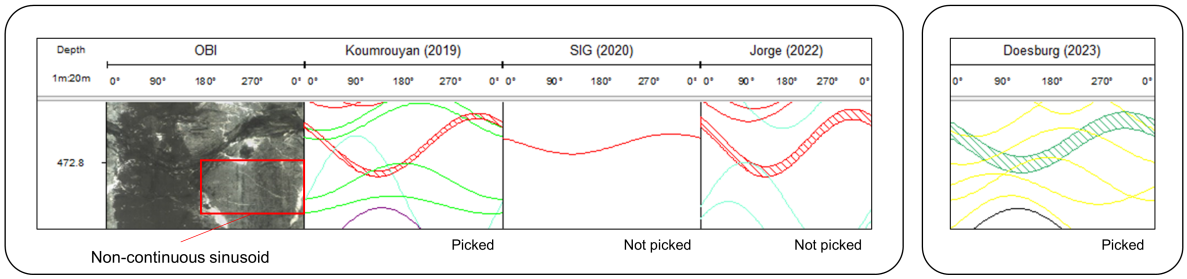

Figure 6.6: Example of a non-continuous sinusoid, picked by Koumrouyan, 2019 and Doesburg, 2023, while not picked by Jorge, 2022 and the SIG, 2020.

While Lo, 2019 only picked structures with high confidence, Doesburg, 2023 picked all structures. This difference in approach may result in under- or over-interpretation of fractures. It is worth noting that if confidence is not defined based on specific properties, it can become arbitrary and influenced by an interpreter's prior knowledge and experience.

Image log

Strong disagreement occurs in intervals where marl and limestone alternate (as reported by Chablais and Rusillon, 2017, 2019).

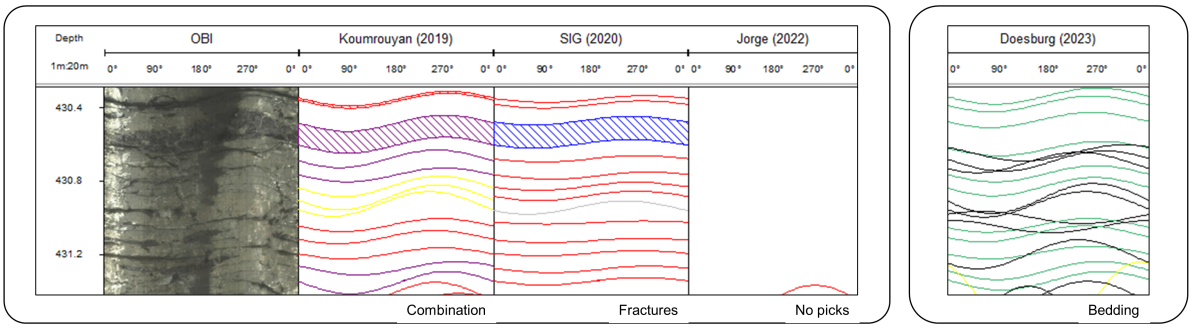

Figure 6.7: Example of a an interval where marl and limestone alternate. Jorge, 2022 does not pick any structures, Koumrouyan, 2019 picks a combination of structures, SIG, 2020 picks fractures and Doesburg, 2023 picks bedding.

Intervals with a high repetition of structures lead to over- and under-picking of structures and significant differences in fracture frequency.

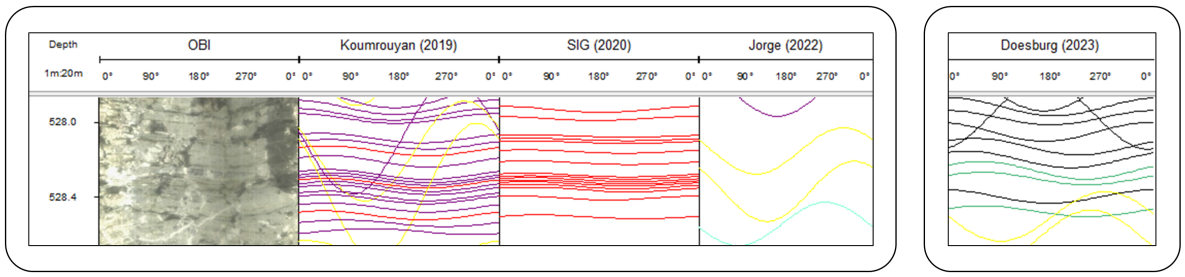

Figure 6.8: Example of a high repetition of structures. Koumrouyan, 2019; SIG, 2020 picked significantly more than Jorge, 2022 and Doesburg, 2023.

In areas with a lot of bedding and/or open/shear fractures, mineralized fractures may be under-interpreted.

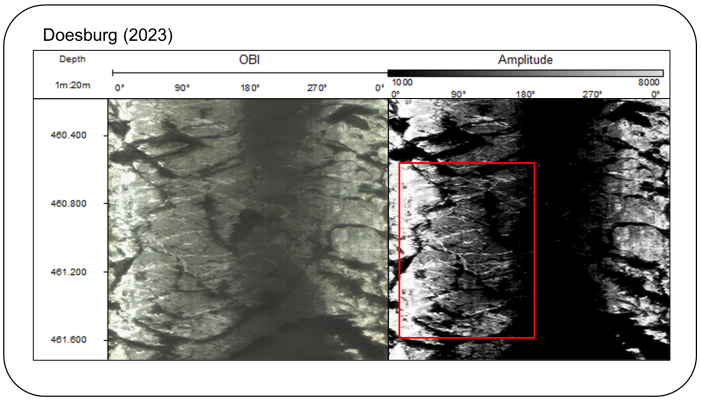

Figure 6.9: Example where bedding and open/shear fractures dominate, resulting in under-picking of the mineralized fractures. The left image gives the OBI and the right image gives the ABI with adjusted amplitude scale by Doesburg, 2023.

Orientation of fractures

Fractures oriented parallel to the bedding can be misinterpreted and mistaken for bedding.

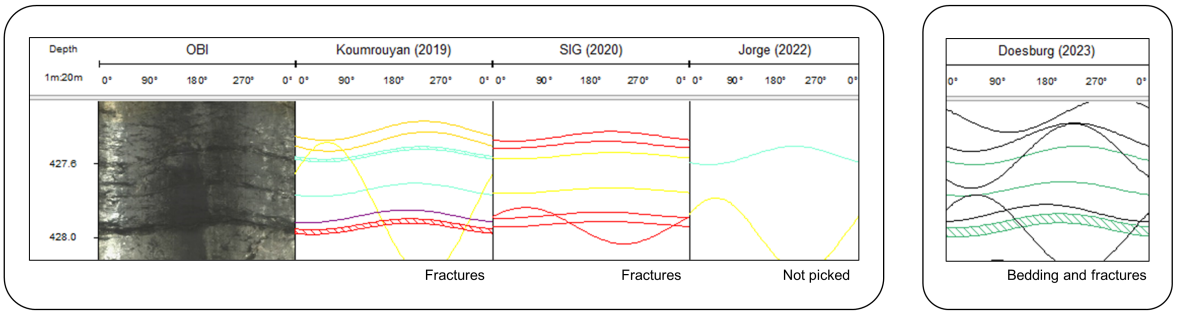

Figure 6.10: Example of possibly bedding parallel fractures. Jorge, 2022 does not pick any structures, Koumrouyan, 2019 and SIG, 2020 pick only fractures and Doesburg, 2023 picks fractures and bedding.

Fractures oriented parallel to the borehole may not be encountered by the image log, resulting in under-interpretation.

6.4.2. Higher level of agreement in the mineralized fractures

The overall agreement between the interpreters is higher in the mineralized fractures, compared to the open/shear fractures for a number of reasons:

Appearance on the image logs

In general, mineralized fractures are easier to pick on the OBI logs as they appear reflective/bright, creating a high contrast to the dark background. On the other hand, open/shear fractures appear transmissive/dark on the OBI logs and lack a similar contrast. This difference in appearance makes mineralized fractures easier to identify, which leads to a higher level of agreement between the interpreters.

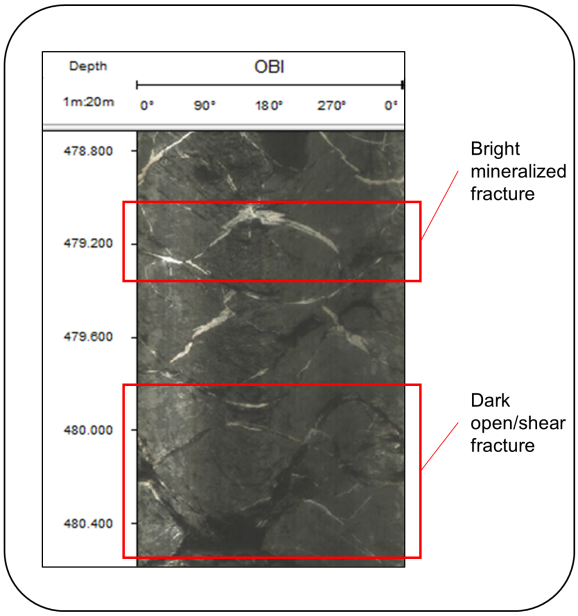

Figure 6.11: Example of a bright sinusoid, classified as a mineralized fracture, and a dark sinusoid, identified as an open/shear fracture.

Bedding and fractures both appear transmissive/dark on the OBI logs, making them look similar. As a result, bedding and fractures are likely to be misclassified or confused. Mineralized fractures look more distinct, making them less likely to be mistaken for bedding. Misclassification of fractures and bedding contributes to a higher disagreement among the interpreters for open/shear fractures.

Limited picking

Especially in the top and bottom of GEo-01, several intervals contained insufficient picks (NED) to perform the ANOVA/MANOVA tests. The absence of picks could indicate either that none of the interpreters picked any mineralized fractures for a specific reason, or that no mineralized fractures are present in those intervals. However, the fact that all interpreters agree on the frequency in intervals marked C and D in Figure 6.4 suggests the latter explanation.

6.4.3. Low agreement in dip angle

Strikingly, the results of the statistical analysis show far more disagreement in dip angle, compared to azimuth or frequency. There are three reasons for this discrepancy:

Caliper log

A proper definition of caliper, depth, and well deviation is essential when importing image logs in WellCAD. This information is crucial for accurately determining the correct dip angle of structures.

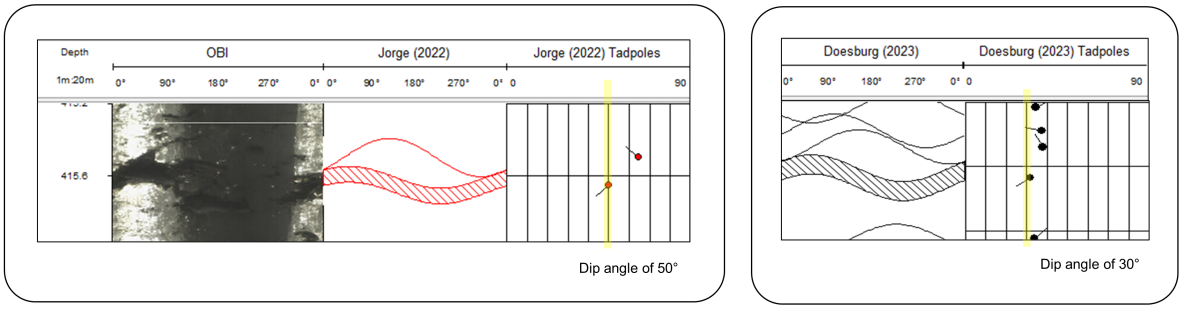

Figure 6.12: Example of two identical sinusoids, picked by Jorge, 2022 on the left and Doesburg, 2023 on the right, resulting in different dip angles

WellCAD calculates dip angles based on the caliper log. If the caliper log is interrupted, dip angles will not be representative.

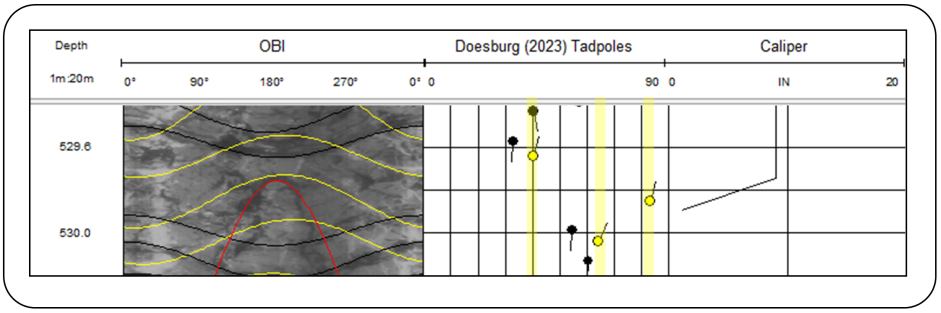

Figure 6.13: Example of three similar oriented mineralized fractures with very different dip angles, related to an interrupted caliper, picked by Doesburg, 2023.

Displaced structures

Fractures may displace other structures, making it impossible to fit a sinusoid accurately. This can result in unrepresentative orientations and unnecessary data scatter.

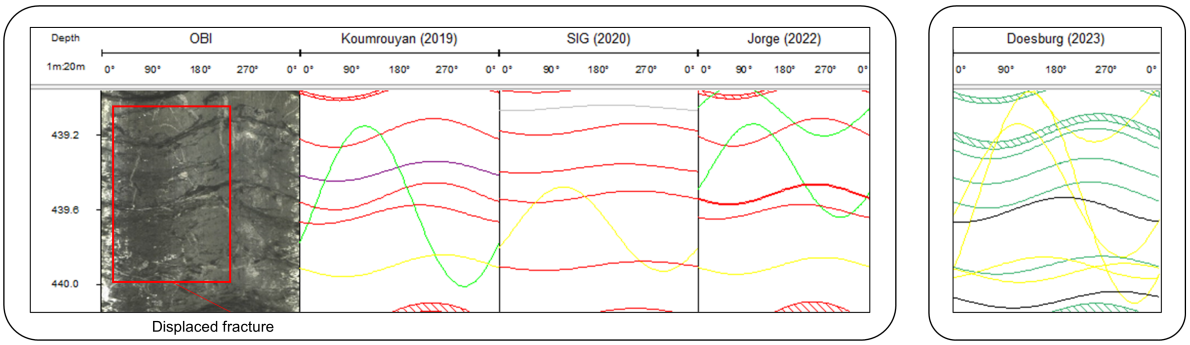

Figure 6.14: Example of a displaced fracture. Koumrouyan, 2019 and Doesburg,2023 fit a similar sinusoid. Jorge, 2022; SIG, 2020 fit alternative sinusoids with lower dip angles.

6.4.4. Low agreement in intervals D, E, L and M

Four intervals show less overall agreement in azimuth, dip or frequency, compared to the rest of the intervals. Several factors contribute to these findings.

Quality of the image log

The quality of the image log can be poor, such as near the edges of the image log, in the proximity of borehole breakouts (identified as dark, irregular shapes), or near faults (see Figure 7.1.4 for more detail). Picking structures in these intervals entails a high level of uncertainty.

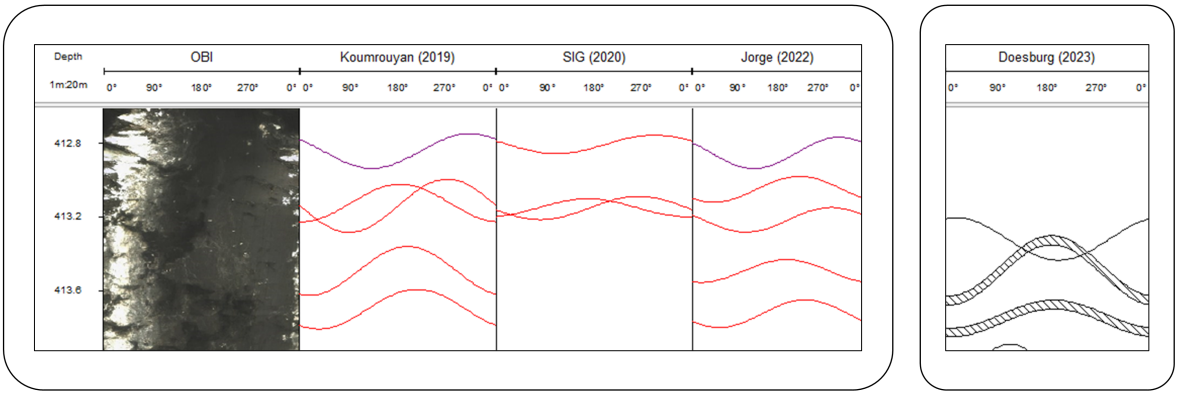

Figure 6.15: Example of low-quality OBI in an interval near the edge of the log. The four interpreters (Jorge, 2022; Koumrouyan, 2019; SIG, 2020 and Doesburg, 2023 all picked different structures.

Certain intervals have high variations in the image log; including appearance, quality, and complexity. Consequently, there are intervals with a high agreement and others with low agreement among the interpreters for both the open/shear fractures and the mineralized fractures.

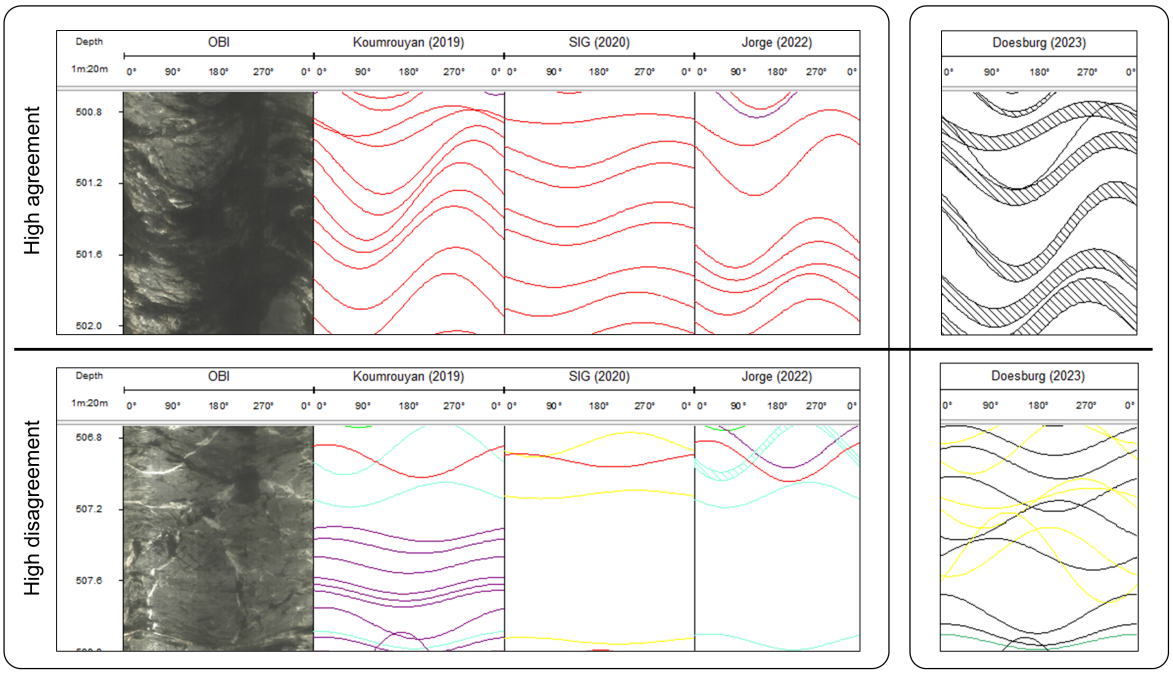

Figure 6.16: Example of an interval with large differences in the OBI. The upper and lower figure are 5m apart and look substantially different. In the upper figure, agreement between the interpreters is high. In the lower figure, agreement between the interpreters is low.

6.5. Recommendations for fracture picking in image logs

The recommendations are subdivided into three phases: 1. importing the data, 2. classification scheme and 3. fracture picking. The three categories are described below, including figures with a schematic workflow.

6.5.1. Phase 1: Importing the data

To import the data and start the fracture-picking process in WellCAD, follow the steps below:

1. Import the image logs, caliper, borehole depth and borehole deviation into the software. While importing the data, it is crucial to define the caliper log properly as this is needed for the software to determine the accurate dip angle. If the caliper is unavailable, the caliper should be defined manually to the bit size in inch or mm. If the caliper is interrupted or deviated in certain intervals, it is advised to mark these intervals.
2. Import any additional logs that are available. These logs can be used complementary in the classification of structures (see subsection 6.5.3 for more detail).

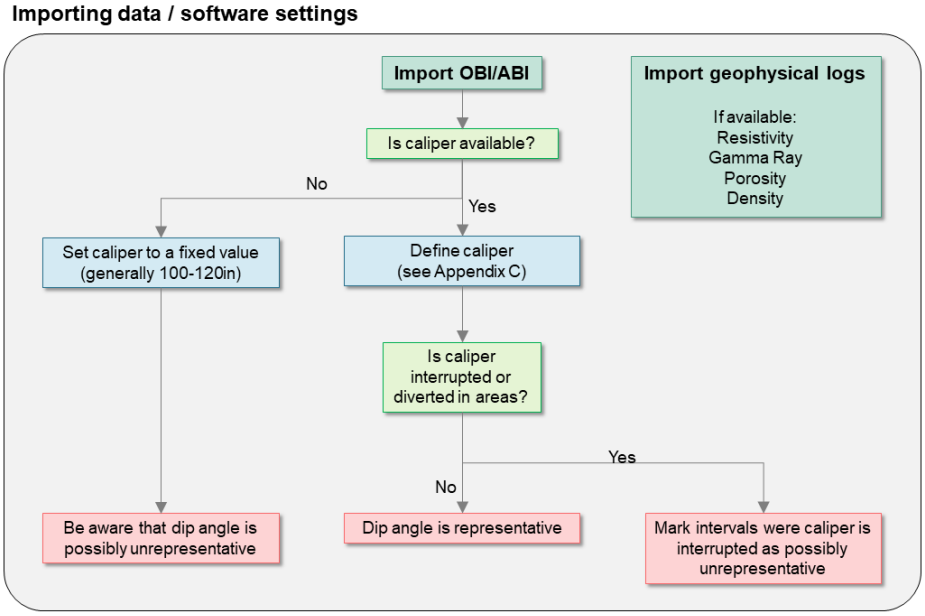

Figure 6.17: Workflow for importing the data and initialization of the workspace.

6.5.2. Phase 2: Classification scheme

A classification scheme should be defined before the start of the picking, in order to maintain consistency in the classification of fractures.

1. Define the criteria for the classification of open/shear fractures, mineralized fractures, bedding, induced fractures and undefined. Figure 6.18 presents the classification used in this study, based on Figure 5.3. It is recommended to adjust this classification scheme according to the available image log data and the objective of the fracture interpretation.
2. Bedding can appear similar to fractures in an image log. Prior knowledge of the bedding orientation or structural geology of the region should be incorporated into the classification of bedding. If no prior knowledge is available, assume that the bedding is horizontal to gently dipping.
3. Create a so-called 'dictionary' in ToadCAD: a tool provided by WellCAD that allows the creation of classification lists and assigning symbols, codes or colors to each category (see the WellCAD manual for detailed instructions). It is possible to create multiple dictionaries and allocate a structure into multiple categories. These additional categories can be used to mark specific structures and/or properties (for example: continuity or confidence) or to visualize specific characteristics, such as orientation in Figure 7.1.

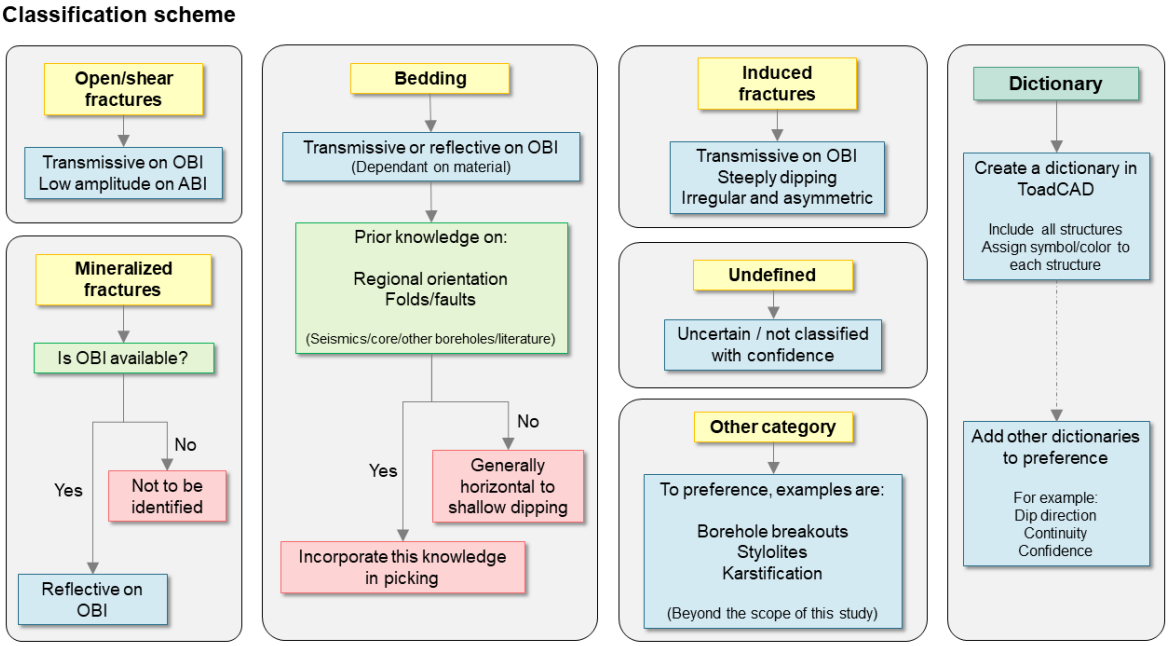

Figure 6.18: The suggested structure classification and criteria. ToadCAD is used to define dictionaries, which are used to classify structures.

6.5.3. Phase 3: Fracture picking

After importing the data and preparing the dictionary, fracture picking can begin, following the workflow of Figure 6.19.

1. Start with an inspection of the image logs and mark intervals where the quality of the images is low.
2. Identify a structure on the image log and fit a sinusoid on top of it. The amplitude and location can be re-adjusted later if needed.
3. Mark non-continuous structures, either using a dictionary or manually.
4. If a fracture shows displacement of another structure, mark the fracture. Regarding the displaced fracture(s), it is important to fit the sinusoid consistently on the highest point of the plane (or any other point of preference).
5. Classify the structure, based on the criteria created in phase 2.
6. If the distinction between a fracture or bedding remains uncertain, inspect available geophysical logs. The most common logs used are:

    - **Gamma Ray** records the presence of naturally occurring radioactive elements. An increase in Gamma Ray is generally caused by a higher shale content of the formation (Shalaby and Islam, 2017).
    - **Resistivity** measures the formations resistivity of electric flow. Open fractures allow drilling mud to infiltrate into the formation and thereby cause a sharp decrease in the resistivity log (Lai et al., 2017).
    - **Density** gives the ratio between the rock mass to its volume. The density will be lowered by the presence of open fractures, and equal or higher by the presence of closed fractures (Dürrast and Siegesmund, 1999).
    - **Sonic log** gives the velocity of waves transmitted through the formation. A decrease in the velocity indicates an open fracture, and an increase indicated a mineralized fracture (Hsu et al., 1987).

    According to Lai et al., 2022, bedding parallel fractures are often discontinuous, unlike tectonic-driven fractures and show low aperture due to the overburden stress. Because of drilling mud infiltrating the formation, the resistivity log will exhibit a sharp decrease.

7. Adjust the scales of the image logs to filter some structures and highlight others. The color scale can be adjusted for all image logs and the property scales can be adjusted for the ABI logs. It is recommended to try various values and repeat this step multiple times with different scales because the effect will depend on the lithology of the rocks, the structure and the image log itself.

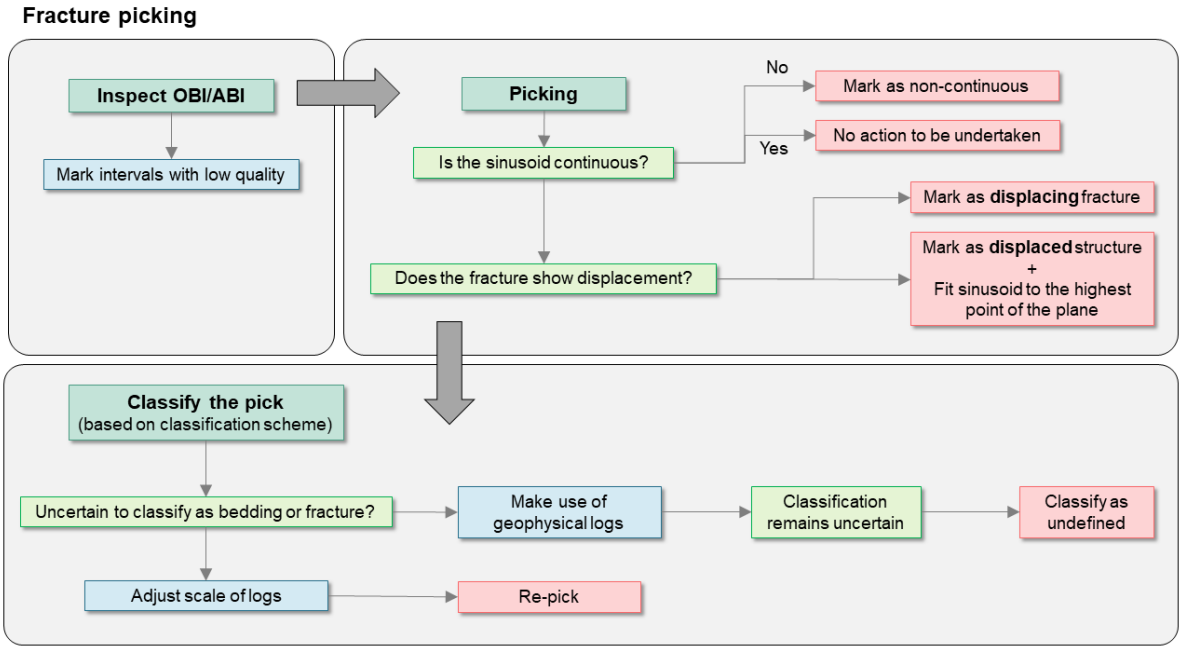

Figure 6.19: Three steps in the fracture picking process: inspection of the image log, picking of a structure and addressing a classification.

The advantage of marking intervals or structures is that, during a later stage of fracture analysis, is to examine the effect of the marked fractures on the bigger fracture population. For example to compare the picking in intervals with low image log quality to the picking in regular intervals. Similarly, marking fractures that show displacement is essential in the determination of the type of movement and relative chronology. Marking structures while picking them is more time efficient than re-inspecting the log multiple times.

Logically, when interpreting or comparing multiple wells, it is recommended to use the same classification scheme for each well. Depending on the image logs and lithologies of the formations, it might be needed to adjust the criteria slightly, for similar reasons as mentioned in subsection 6.5.2.

Although not performed in this study because of the limited time-scope, it is recommended to apply a correction in fracture density for borehole parallel fractures (Tartarotti et al., 1998).

7

Results: fracture sets and cross-sections

This chapter addresses the second part of this study, and presents the results from the picking of GEo-01 and GEo-02 and the set definition in each well. To prevent a clutter of the results, all data was separated into bedding, open/shear fractures, and mineralized fractures (Table 7.1). Picking of induced fractures and undefined structures are not presented, since they are irrelevant to answering the research question.

Table 7.1: Overview of the number of picks per structure.

	GEo-01 (OBI, Amplitude, Transit-time)	**GEo-02 (Amplitude, Transit-time)**
Total number of picks	1030	410
Open/shear fractures	607	211
Mineralized fractures	213	0
Induced fractures	4	6
Bedding	195	176
Undefined	11	17

7.1. Picking and observations in GEo-01

7.1.1. Bedding

In GEo-01, a total of 195 bedding surfaces have been identified. When plotted against depth, these surfaces exhibit an overall clockwise change in dip direction from north (red in Figure 7.1a) at the top, gradually transitioning to south (blue) at the bottom. Though between 430-515m(MD), the majority of the bedding dips towards E-SE. The dip angle also varies with depth, ranging from 0°, increasing up to 60°, and then decreasing back to 10°. This gradual change in dip angle is observed between 440-480 m(MD), forming a bell-shaped curve. Furthermore, the frequency of picks varies over depth, with a higher number of picks in the top half of the well compared to the bottom half.

On the stereoplot, the poles form an arc-shaped distribution, with a cluster in the west between 10-30°. This arc shape emphasizes the trend in orientation observed from the tadpoles.

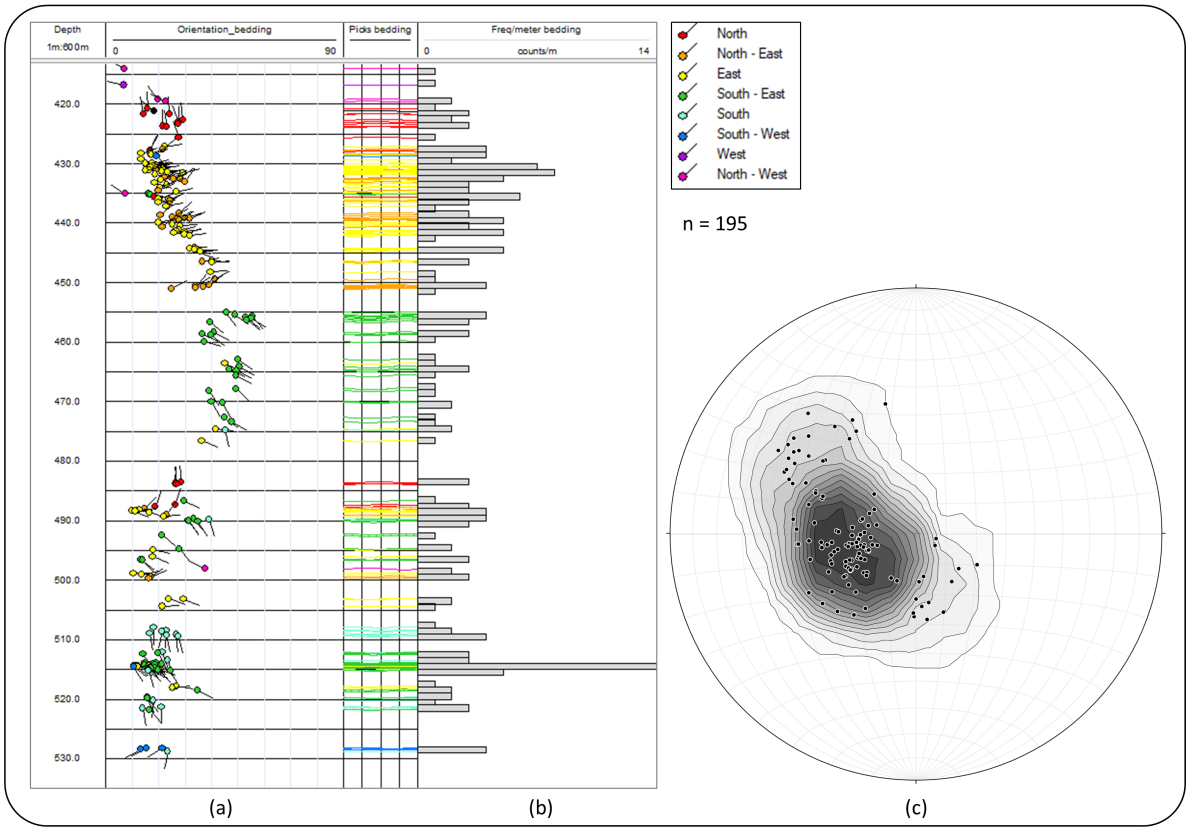

Figure 7.1: Results of the bedding picking in GEo-01. (a) Tadpoles and sinusoids. The colour refers to the dip direction. (b) Bedding frequency per meter. (c) Stereoplot of all picks.

The local subsurface in the vicinity of GEo-01 was reconstructed using the bedding picks. The remarkable variation in dip and dip direction strongly suggested the presence of folds, faults or both. However, the two available seismic lines do not show folds or faults that can be observed at the same scale as the image logs. Therefore, the reconstruction relies solely on the data obtained from the image logs. In contrast, several observations from the image log do suggest the presence of possible faults in GEo-01, as described in more detail in Figure 7.1.4. These potential faults are located around 462, 466, 483 and 502m(MD) and dip east with an angle of 50-70°, but their movement remains unknown.

Four different reconstructions were created, due to the uncertainty of the faults and the unknown movement, and because the bedding orientations do not obviously indicate a specific structure, such as a fold. The four reconstructions are presented as columns in Figure 7.2. **Column A** incorporates all four faults, with steeply dipping bedding between them. The faults may cause local deformation of the bedding (drag), as illustrated in **column B**. However, it should be noted that the potential faults around 462,

466 and 502m(MD) have minimal impact on the orientation of the bedding, while the potential fault at 483m(MD) does seem to affect the bedding. It might be argued that the fault at 483m(MD) may be the only fault present in the subsurface. **Column C** presents a reconstruction with a single fault, resulting in an increase in the dip angle of the bedding due to drag. **Column D** presents a reconstruction similar to the fold-model proposed by Lo, 2019.

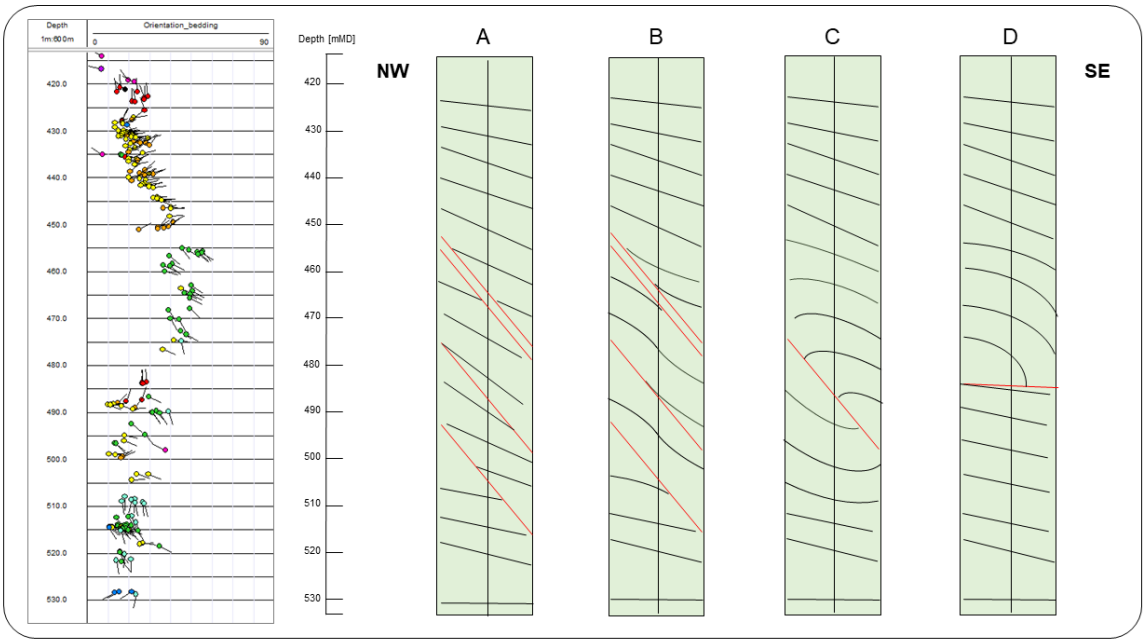

Figure 7.2: Left shows the bedding picks of GEo-01. On the right are four reconstructions of the subsurface, labelled A to D.

7.1.2. Open/shear fractures

A total of 607 open/shear fractures were identified in GEo-01, as presented in Figure 7.3. The unfolded fractures exhibit a range of dip directions in all directions. However, in the bottom 20m of the well, the majority of the fractures dip towards the south. The dip angle of the unfolded fractures varies between 10-50°, with a slight overall increase between 440-490m(MD), ranging between 40-70°. This trend in dip angle is consistent with the observed trend in the bedding orientation (Figure 7.1).

After backtilting, the fractures display a different pattern, characterized by lower dip angles. The poles on the stereoplot show a tighter clustering after backtilting, particularly in the NE direction.

The frequency of fractures shows a slight increase with depth, with peaks around 478, 490-495, 508-512 and 527-529 m(MD). On the other hand, there are low-frequency intervals between 418-422, 437-440 and 455-460 m(MD).

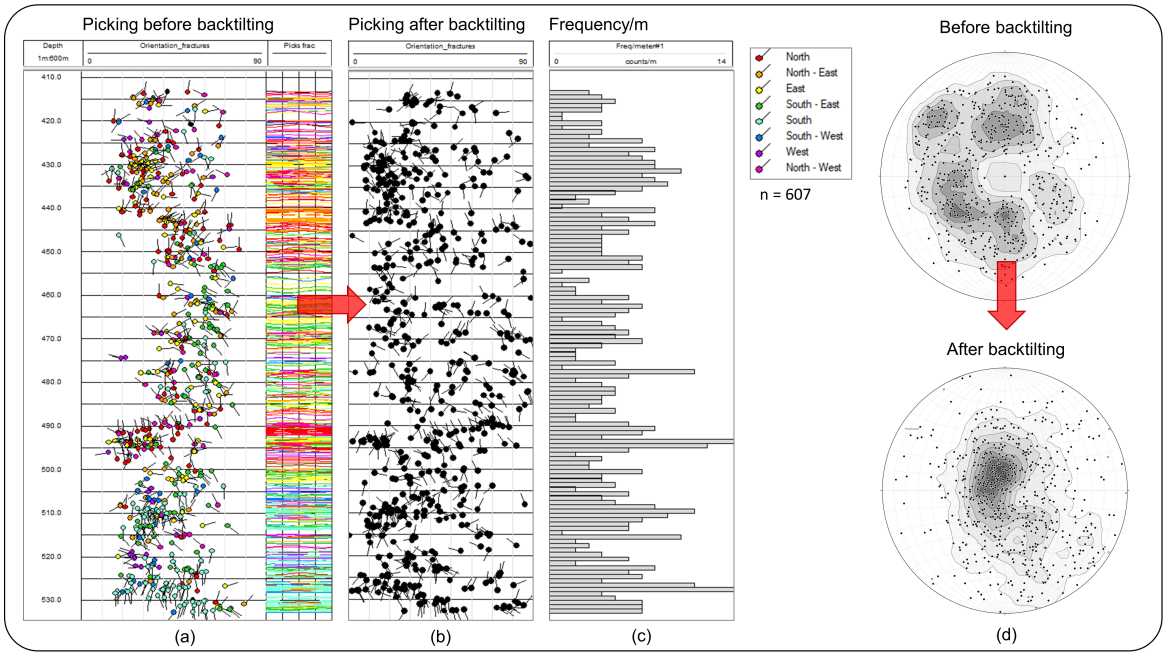

Figure 7.3: Results of the open/shear fracture picking in GEo-01. (a) Tadpoles and sinusoids before backtilting. The colour refers to the dip direction. (b) Tadpoles after backtilting. (c) Fracture frequency per meter. (d) Stereoplot before and after backtilting.

7.1.3. Mineralized fractures

A total of 213 mineralized fractures were identified in GEo-01. Prior to backtilting, the majority of the fractures showed a dip direction towards the W-NW, with dip angles ranging between 30-60°. Interestingly, the unfolded mineralized fractures did not display a similar pattern in orientation, as the bedding and open/shear fractures. After backtilting, the dip orientation of the mineralized fractures remained predominantly W-NW, while the dip angle increased to 50-90°.

In terms of frequency, the mineralized fractures demonstrate frequency highs between 455-480 m(MD), and frequency lows between 41-466, 480-495 and 519-524 m(MD).

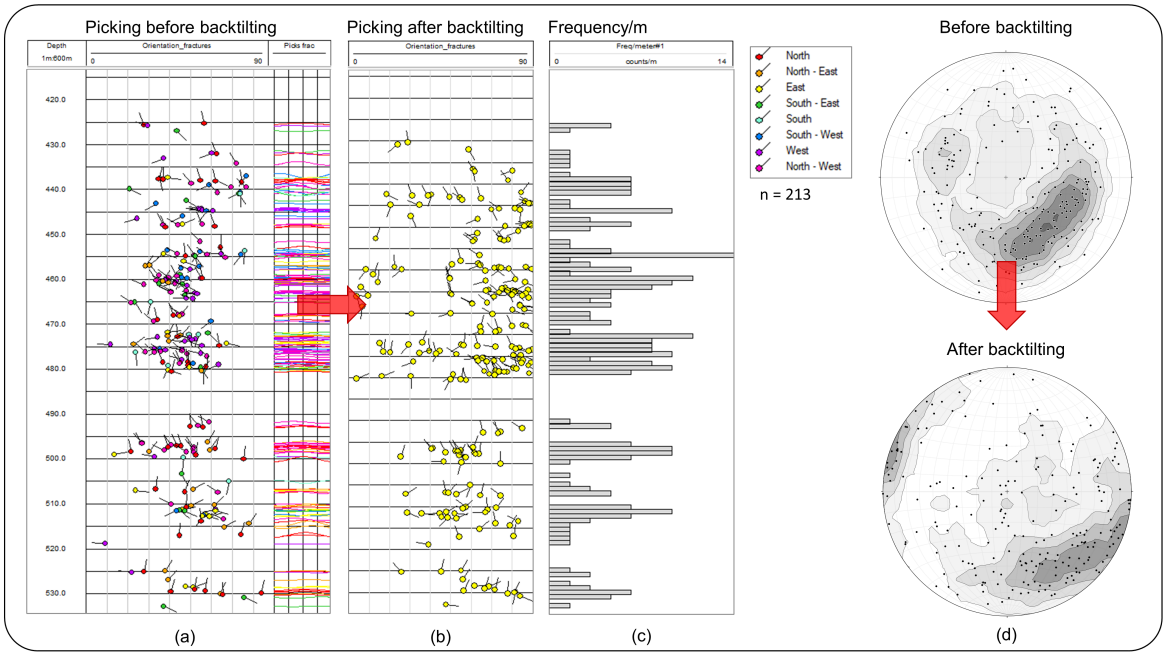

Figure 7.4: Results of the mineralized fracture picking in GEo-01. (a) Tadpoles and sinusoids before backtilting. The colour refers to the dip direction. (b) Tadpoles after backtilting. (c) Fracture frequency per meter. (d) Stereoplot before and after backtilting.

7.1.4. Observations on the image log

A close inspection of the image log allowed for indicators of movement along fractures, indicators of relative chronology and identification of faults. The observations are presented in this section.

Movement along fractures

Even though sparse, some of the fractures in GEo-01 display movement along the fracture planes, either moving bedding or other fractures. By using the 3D-view feature in WellCAD, the picked sinusoids are represented as planes, enabling the determination of whether the displacement is normal or reverse.

A total of 35 observations were made where an open/shear fracture displaced another structure; in 11% the fracture displaced bedding, in 60% the fracture displaced a mineralized fracture and in 29% the fracture displaced another open/shear fracture. Among all observations, 37% is classified as normal displacement, and 63% is classified as reversed displacement. The displacement ranges from centimetres to decimeters in scale.

On the other hand, only 3 observations were made where a mineralized fracture cut bedding and 2 observations were made where a mineralized fracture cuts another mineralized fracture. The mineralized fractures displayed minimal to no displacement.

Several examples are presented in Figure 7.5. The stereoplots can be used in defining fracture sets, which is described in more detail in subsection 7.3.1.

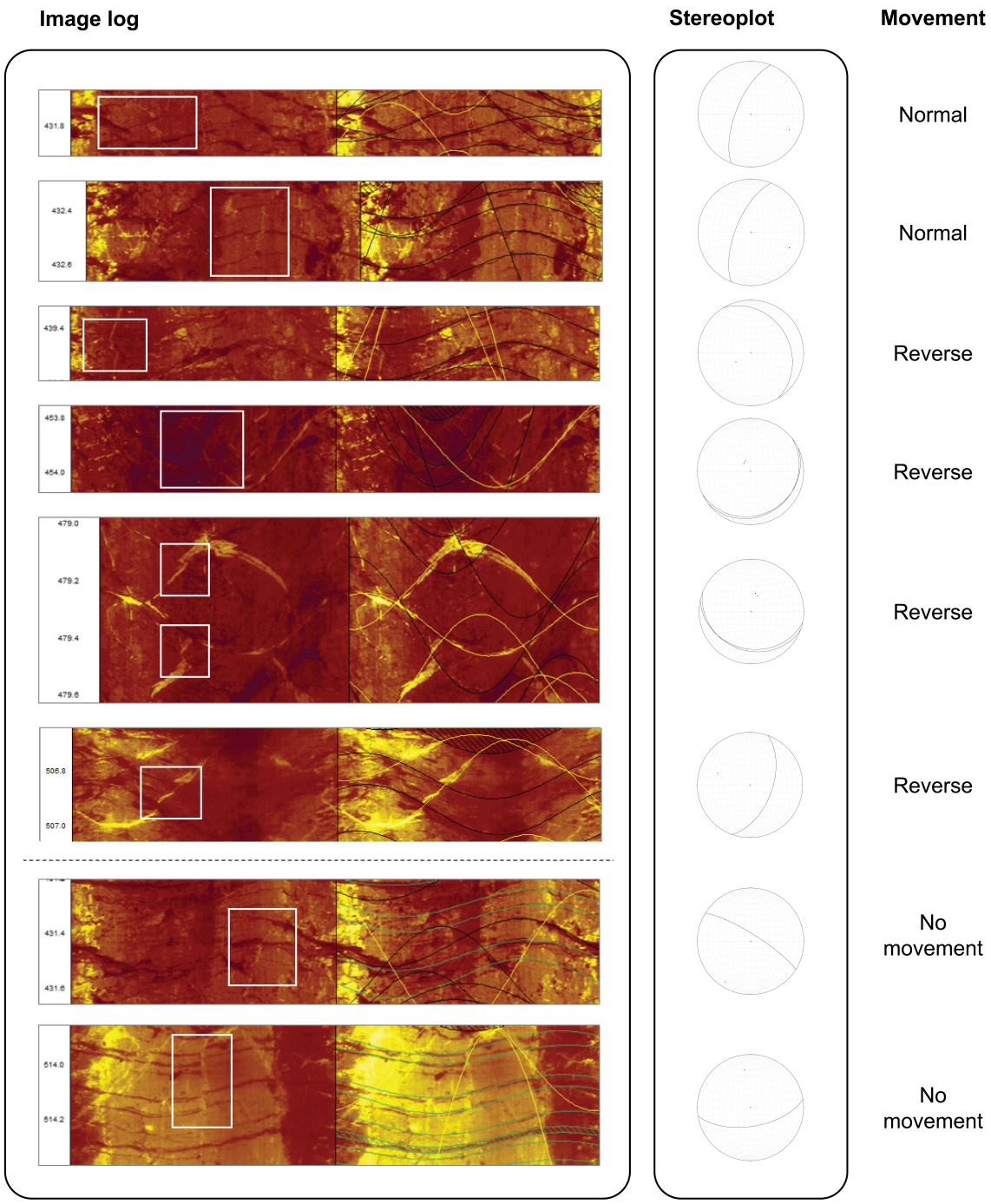

Figure 7.5: Examples of observations of movement along fracture planes in the OBI logs of GEo-01: OBI without and with interpreted structures, stereoplots and the movement. Above the dashed line are examples of open/shear fractures displacing structures, and below the dashed line are examples of mineralized fractures without any displacement.

Relative chronology

Observations regarding the relative chronology of fractures are presented in Figure 7.6 and 7.7.

While 21 observations were made where an open/shear fracture crosscuts a mineralized fracture, only 10 observations were made where an open/shear fracture crosscuts another open/shear fracture of which half was dubious.

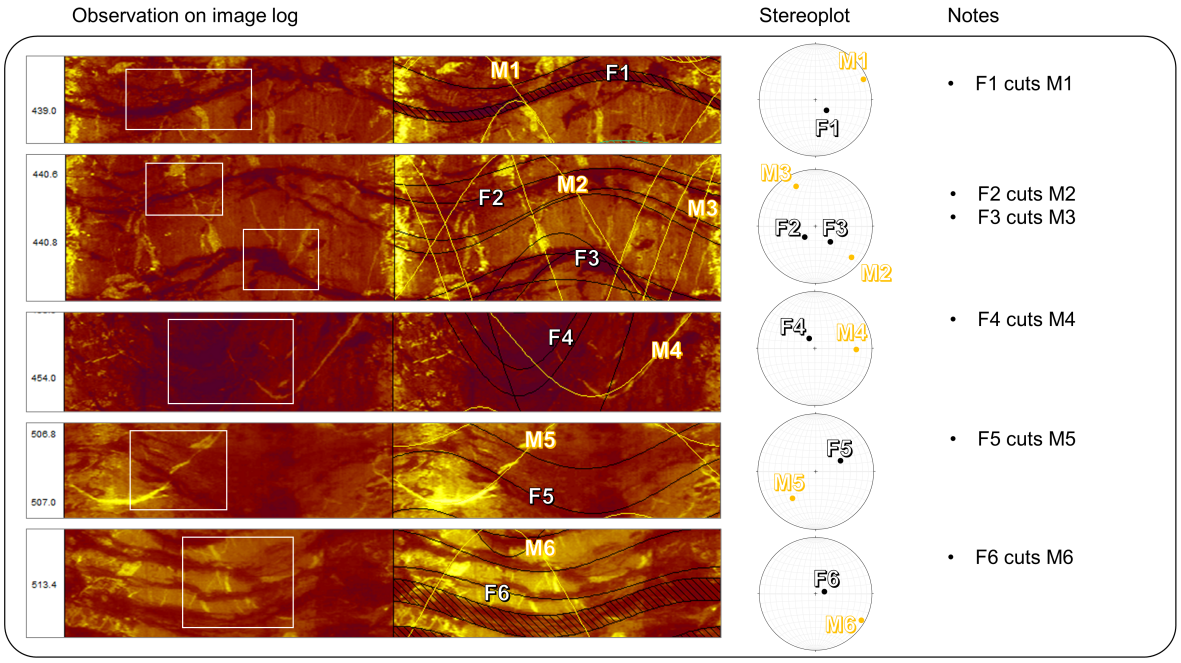

Figure 7.6: Examples of cross-cutting relationships between mineralized and open/shear fractures, indicating the relative chronology.

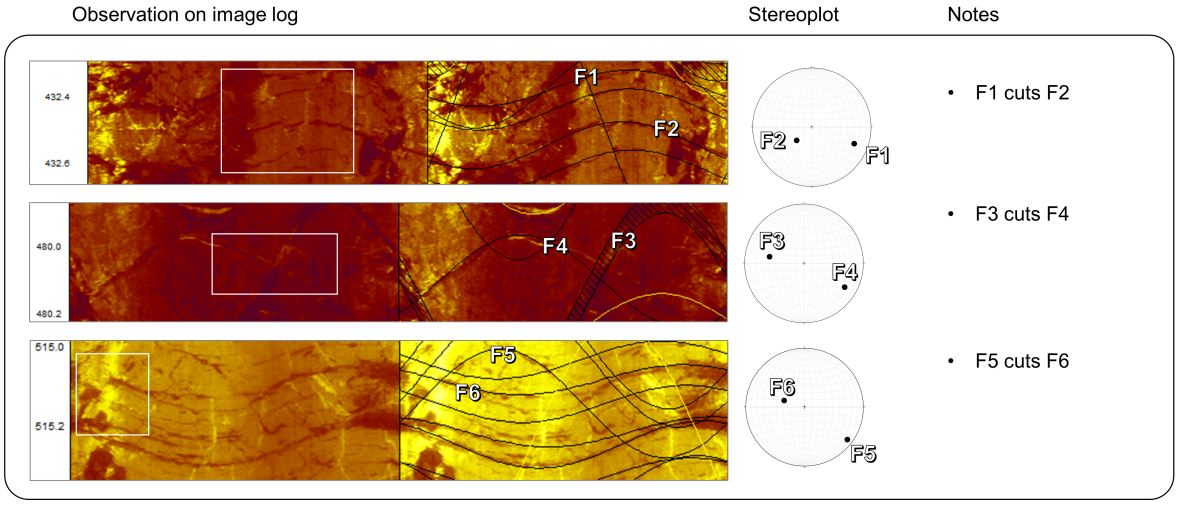

Figure 7.7: Examples of cross-cutting relationships between open/shear fractures, indicating the relative chronology.

Fault identification

A closer examination of the GEo-01 image logs shows several locations of potential faults. All four dip 50°-70° towards the east (see Figure 7.8).

The interpretation of these faults is based on several factors. Firstly, the sinusoids appear much darker and thicker compared to the fractures. Secondly, there is a noticeable difference in the image log above and below these sinusoids; potentially indicating a change in bed texture caused by displacement along these potential faults. Thirdly, there is an abrupt change in certain geophysical log responses (Khoshbakht et al., 2009). Especially resistivity increased significantly, which could suggest the presence of open fractures or faults (Lai et al., 2017; Shalaby and Islam, 2017).

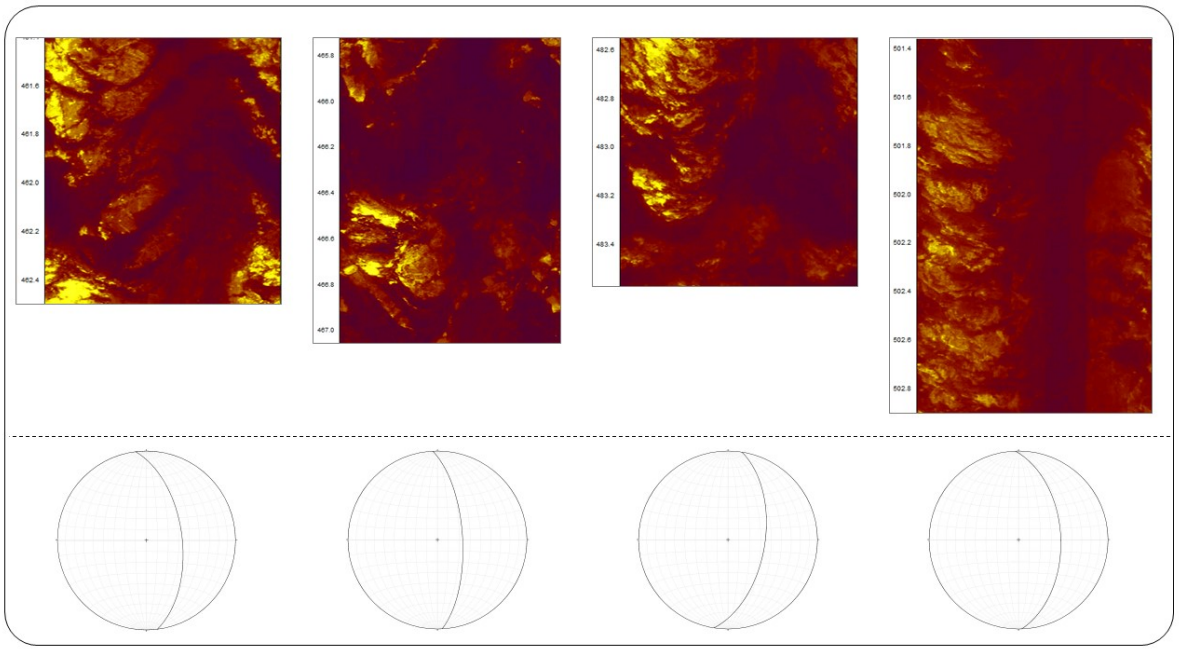

Figure 7.8: Four OBI log intervals of GEo-01, indicating the presence of faults, including stereonets. Displacement along the faults remains unconstrained.

7.2. Picking and observations in GEo-02

7.2.1. Bedding

In GEo-02, a total of 176 bedding structures were picked. When plotted against depth, the bedding remains fairly constant, dipping towards the E-SE with an angle between 10-20° (Figure 7.9). The vast majority of the bedding is picked in the middle part of the well, between 855-940m(MD). Above and below this interval, the bedding picks are limited.

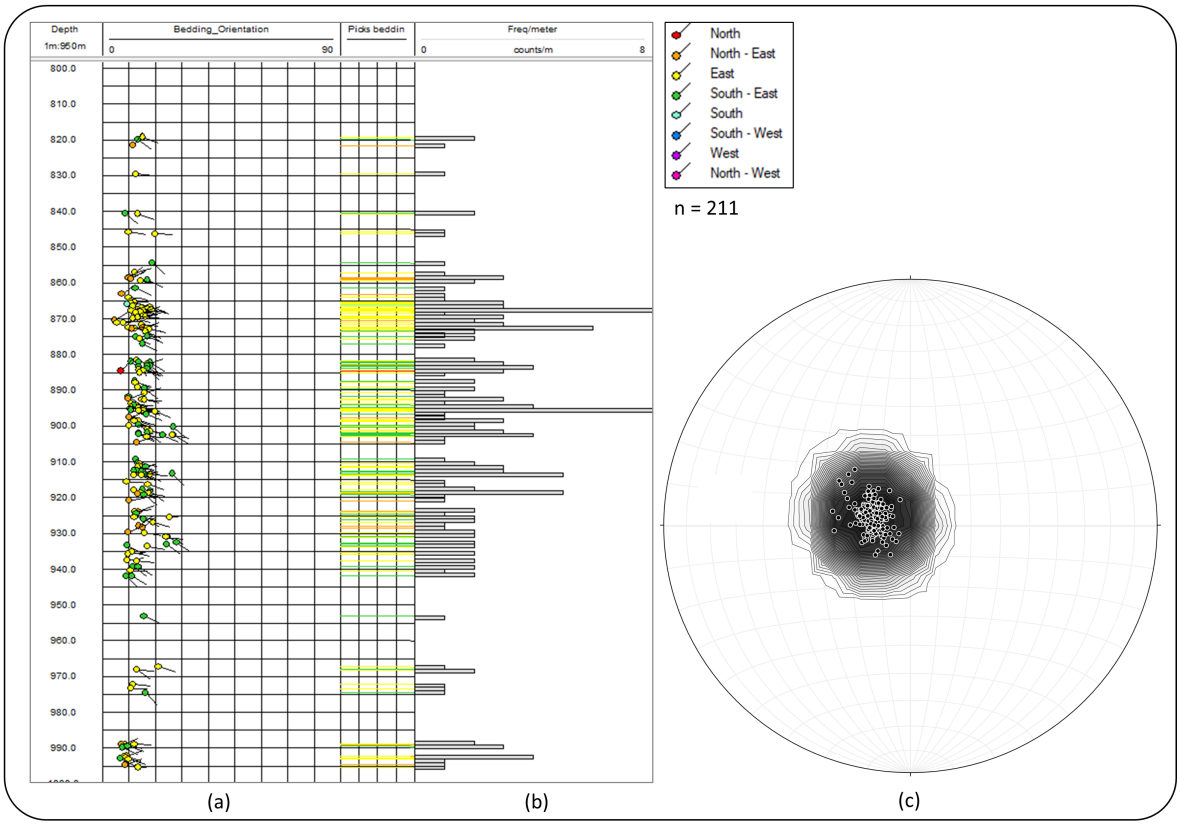

Figure 7.9: Results of the bedding picking in GEo-02. (a) Tadpoles and sinusoids. The color refers to the dip direction. (b) Bedding frequency per meter. (c) Stereoplot of all picks.

The bedding picks were integrated into a local reconstruction of the subsurface near GEo-02, as depicted in Figure 7.10. The bedding orientation remains relatively constant over the full borehole depth, slightly dipping towards the SE. For simplicity, it is assumed that the bedding orientation remains constant in intervals without any picking data.

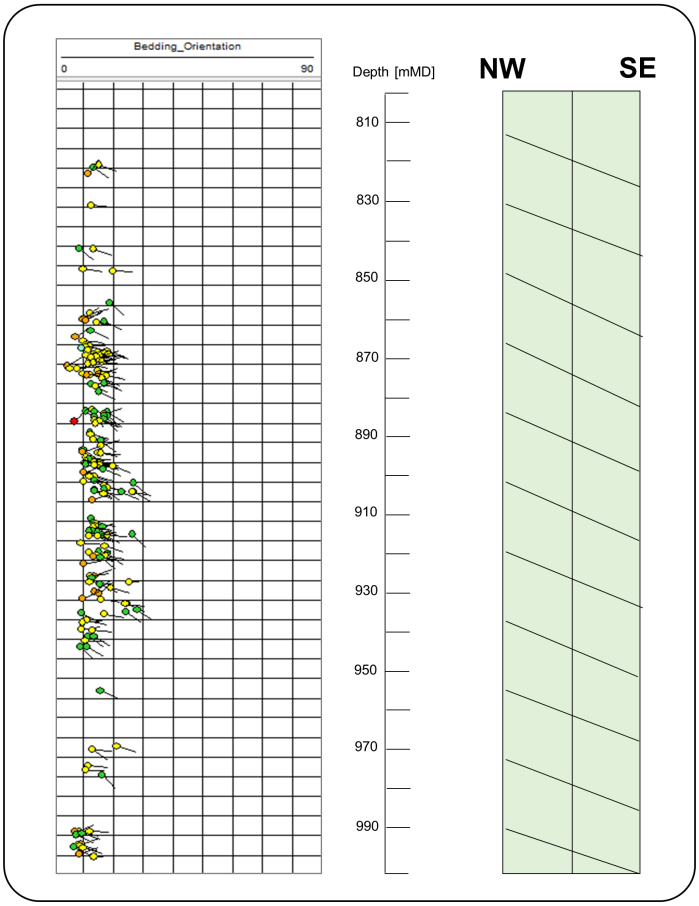

Figure 7.10: Left shows the bedding picks of GEo-02 and right shows the simplified reconstruction of the bedding in the interval of the image log, oriented NW-SE.

7.2.2. Open/shear fractures

A total of 211 open/shear fractures are picked in GEo-02 and are presented in Figure 7.11. Before backtilting, the tadpoles and stereoplot of the fractures show dip angles up to 70° and are distributed in all directions. However, the majority of fracture dip towards the east. After backtilting, the fractures dip predominantly towards the NW with an angle of 10-40°. Notable is the absence of picks in the upper 40m of the well and between 905-918m(MD).

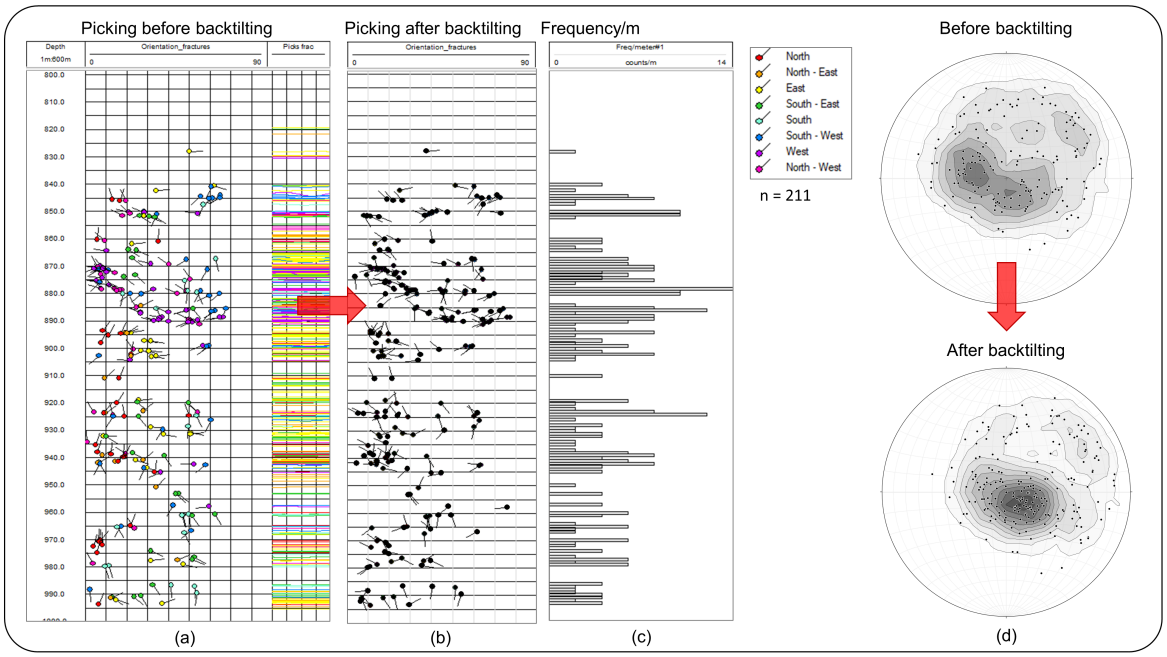

Figure 7.11: Results of the open/shear fracture picking in GEo-02. (a) Tadpoles and sinusoids before backtilting. The color refers to the dip direction. (b) Tadpoles after backtilting. (c) Fracture frequency per meter. (d) Stereoplot before and after backtilting.

7.2.3. Observations on the image log

Indications of movement or relative chronology could not be observed from the ABI logs of GEo-02. Four cross-cutting relationships where observed as shown in Figure 7.12. From these, it is not possible to withdraw any new information regarding movement or relative timing.

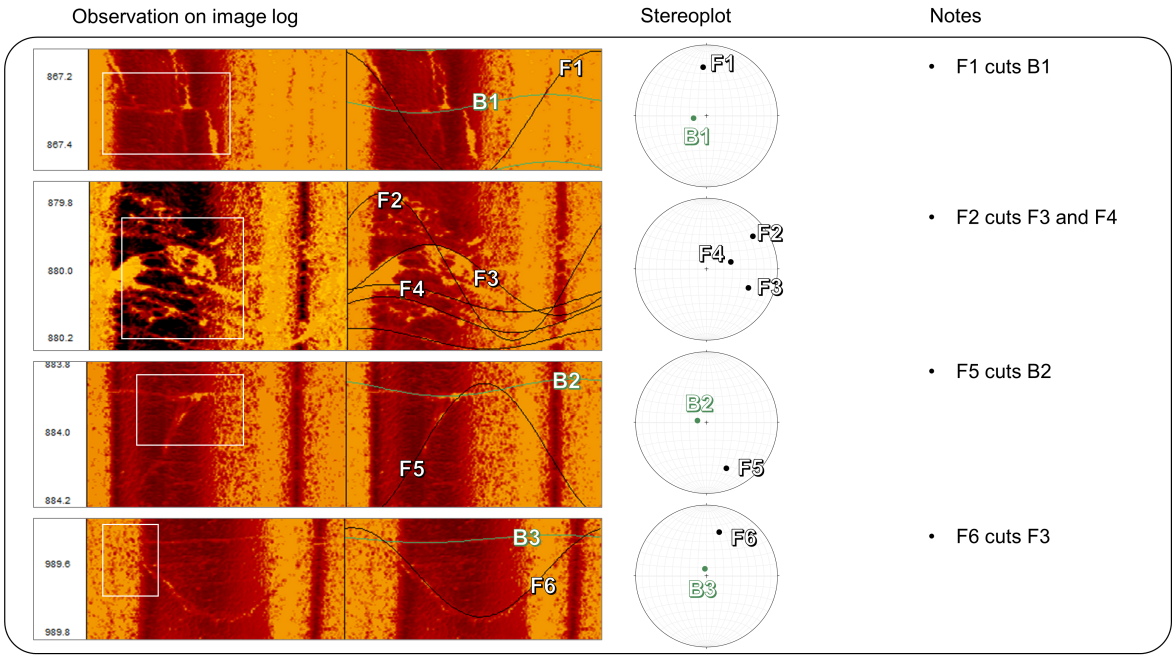

Figure 7.12: Examples of two structures cross-cutting in GEo-02. No movement could be constrained.

7.3. Interpretation in terms of fracture sets and associated stress regimes

The orientation and movement of the backtilted fractures, in combination with relative chronology were used to define fracture sets and interpret associated stress regimes.

7.3.1. Sets and stress regimes in GEo-01

In GEo-01, the fracture orientations generally follow the same trend as the bedding orientations (comparing Figure 7.1 with Figure 7.3). This trend indicates that at least part of the fractures must pre-date the bed tilting.

A total of five fracture sets were defined in GEo-01, which are shown in Figure 7.13. The mineralized fractures are defined as **Set 1**, and several observations show that these fractures clearly pre-date all other fractures. The mineralized fractures show minimal to no shearing displacement and are therefore classified as veins. Veins typically form with σ_3 oriented perpendicular to the fracture plane. The veins are oriented N040-080° and steeply dipping, meaning that σ_3 would be oriented NW-SE. The actual orientation of σ_1 could not be constrained, meaning the veins could have formed in a normal (σ_1 oriented vertically) or strike-slip regime (σ_1 oriented horizontal, perpendicular to σ_3).

The timing of Sets 2,3, and 4 is based on the few indicators of relative chronology from GEo-01 (Figure 7.7). **Set 2A and 2B** are interpreted as a pair of conjugates (Figure 7.13). Both sets are oriented roughly NW-SE, dipping 20-40° in opposite directions and display reverse movement. This orientation and movement would imply a reverse regime with σ_1 oriented NE-SW and σ_3 horizontal.

Set 3 is interpreted as a set of polymodal fractures, dipping 50 to 80° and timed in between Set 2 and Set 4. Polymodal fractures form with σ_1 oriented vertically, indicating a normal regime.

Set 4A and 4B form the largest sets, and are interpreted as another conjugate pair. The sets are oriented NE-SW, dip 10-50° in opposite directions and both show reverse movement based on the image logs. The conjugate set would have formed within a reverse regime with σ_1 oriented NW-SE and σ_3 oriented vertically.

The last set (**Set 5**) is characterized by steeply dipping fractures that display no movement and clearly postdate any of the other sets. The fractures are defined as a set of joints oriented N030-080°. These fractures are only observed between 463-493 m[MD] (see Appendix D). As depicted in Figure 8.1, four faults are located around 462, 464, 482, and 502m[MD] in GEo-01. This set is therefore likely related to the presence of the faults. Because this set formed the latest and is fault-related. This implies that the faults either formed during this stage propagated, or have gotten reactivated (Kim et al., 2004).

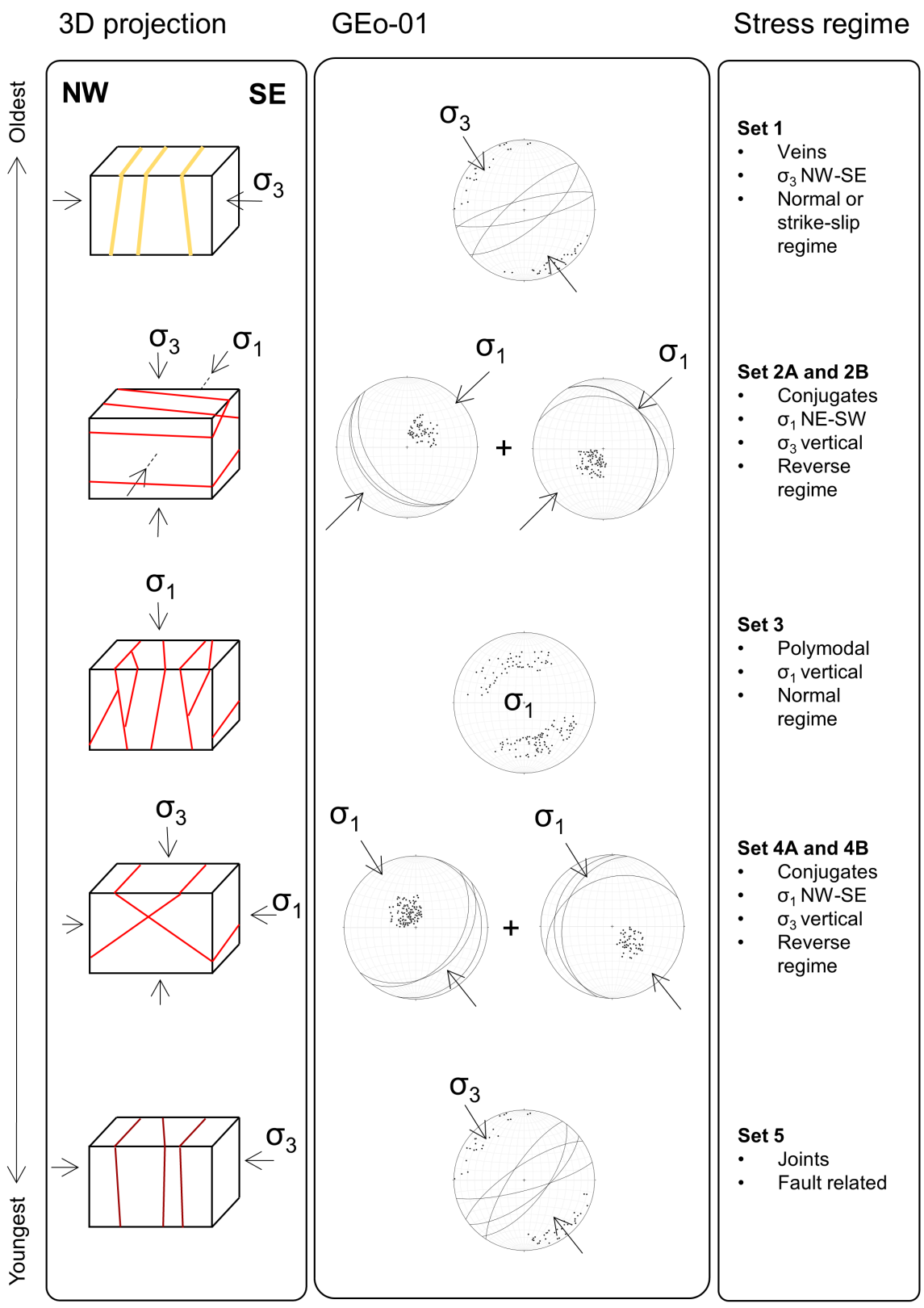

Figure 7.13: Interpretation of the GEo-01 fractures in terms of sets and associated stress regimes. Five sets were recognized in the well, ordered to chronology in this figure. The image gives a simplified 3D representation of each set, the stereoplot data, and the associated orientation of σ_1, σ_3, or both.

7.3.2. Sets and stress regimes in GEo-02

In GEo-02, no clear indications of displacement or relative chronology were observed. The absence of displacement observations suggests that either all fractures should be classified as joints or that displacement is not recognized from the image log. There are several reasons to support the latter assumption. Firstly, ABI logs generally have lower resolution and detect fewer fractures compared to OBI logs (Gaillot et al., 2007). This is evident in GEo-01, where the OBI logs exhibit a significantly higher resolution than the ABI logs. Secondly, it is generally assumed that one of the principal stresses is oriented vertically, following Anderson's theory (Fossen, 2016). If all fractures were joints, a substantial portion would not align with this theory. Additionally, classifying all fractures as joints would not align with the regional geological context, especially considering the proximity of GEo-01, which is only 7km away. Such distinct fracture populations would require an exceptionally complex geological history to explain. For these reasons, it is assumed that the fractures are not all joints, but that the displacement was not captured by the borehole and could not be observed.

Fracture sets were therefore defined based on clusters of orientations on the stereoplot, leading to the definition of the three sets as in Figure 7.14). Because no observations were made that indicated relative chronology between the fractures, the timing of the sets remains unconstrained.

Set 1 is oriented NE-SW, shallow dipping towards the NW. **Set 2** is oriented ENE-WSW ad dipping shallowly towards the NNW. Possibly, Set 1 and 2 make up a pair of conjugates, but due to the absence of movement indications, this cannot be concluded. However, these sets show a close resemblance in orientation to Set 4 in GEo-01, and in both wells, these sets form the majority of the fracture population. Therefore, it might be argued that indeed Set 1 and Set 2 form a pair of conjugates. If so, the conjugate pair would have formed in a reverse regime with σ_1 oriented NW-SE and σ_3 oriented vertically. **Set 3** dips towards the SW with an angle of 40-70° and forms a small fraction of the full fracture population. Because movement is unknown, the stress regime remains unconstrained

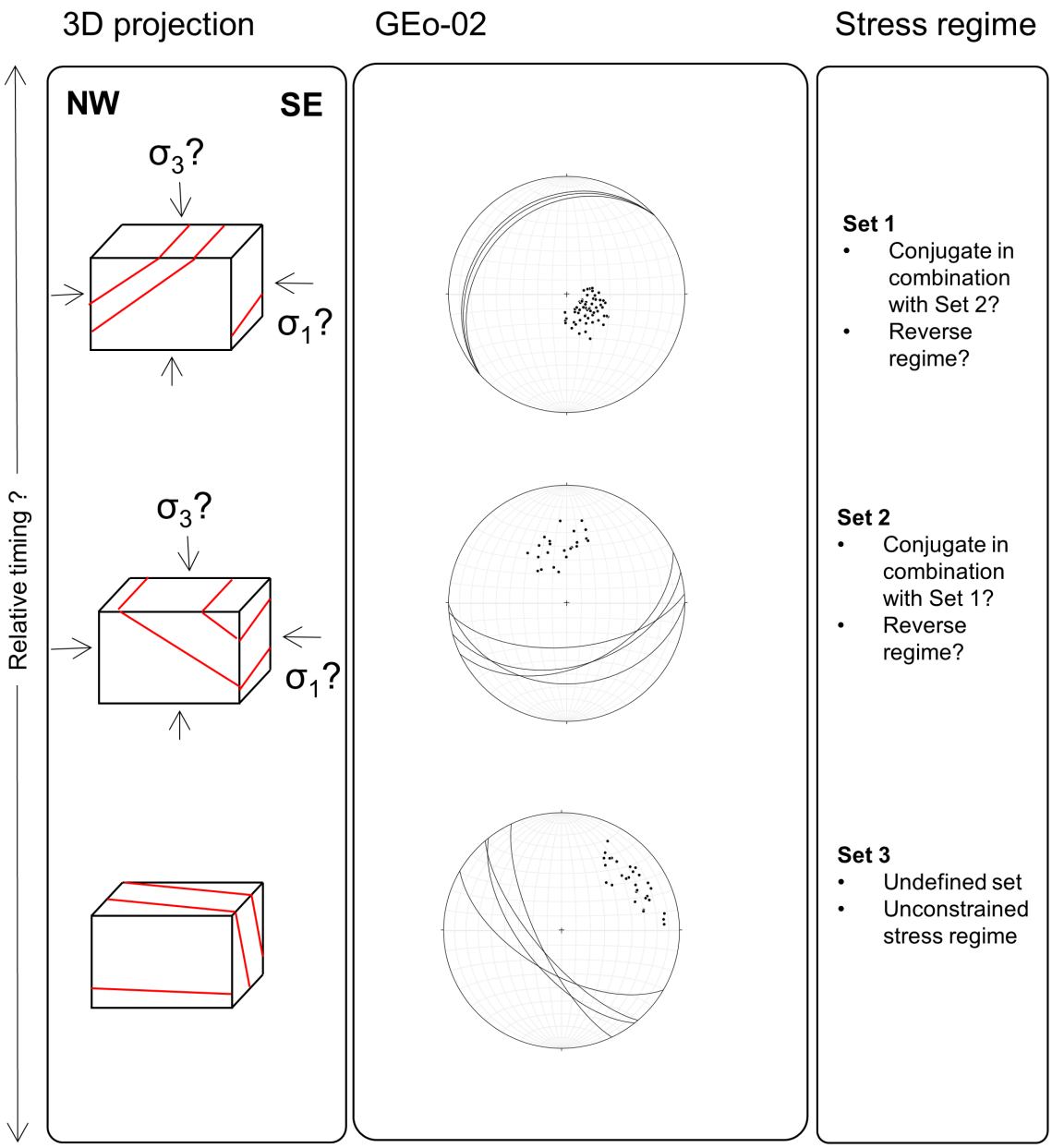

Figure 7.14: Interpretation of the GEo-02 fractures in terms of sets and associated stress regimes. Three sets were interpreted in the well, solely based on clusters of orientations in the stereoplot. The image gives a simplified 3D representation of each set, the stereoplot data, and a suggestion for the associated orientation of σ_1 and σ_3.

8

Discussion

This study aims to reconstruct a reliable fracture history of the Geneva Basin. The improved fracture picking data, information on relative timing, and an understanding of the geological history are integrated into this chapter to provide a reliable evolution of fractures in the Geneva Basin, followed by a discussion on the limitations and uncertainties of the work.

8.1. Cross-section between GEo-01 and GEo-02

Out of the four reconstructions of GEo-01 (Figure 7.10), it could not be concluded with certainty which reconstruction represents the subsurface best. The seismics do not capture structures at this scale, the fault observations and their movement remain uncertain and the bedding orientations do not provide a clear explanation. Lo, 2019 and Moscariello, 2019 have interpreted several faults with similar orientations near the well. On the other hand, Clerc et al., 2015 and Planes et al., 2019 mention the presence of small-scale folds.

Despite the uncertain nature of the subsurface near GEo-01, the reconstructions of GEo-01 and GEo-02 were integrated into the large-scale cross-section from Koumrouyan, 2019; Moscariello, 2019 (Figure 3.1). The new cross-section is shown in Figure 8.1 and connects the two wells.

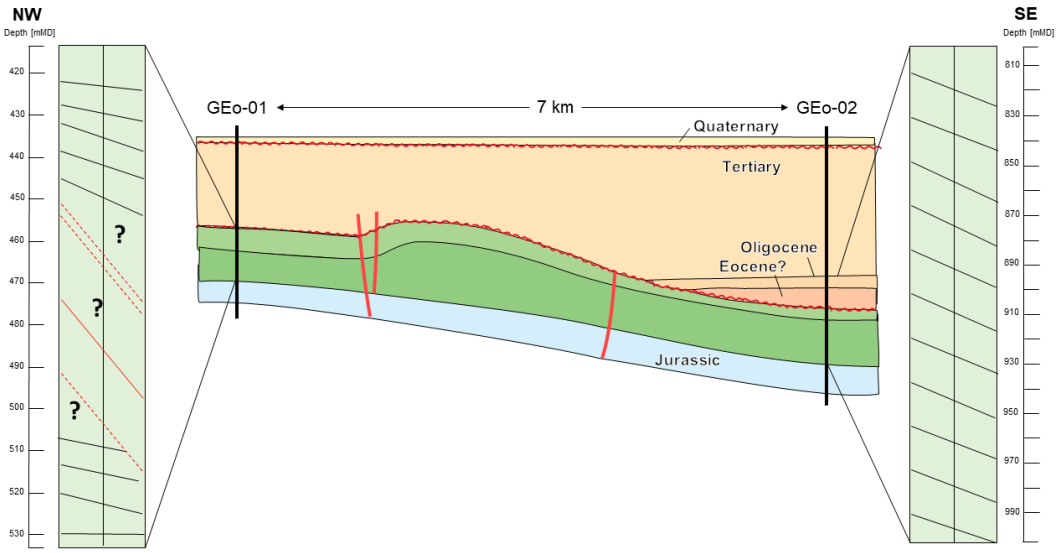

Figure 8.1: Cross-section between GEo-01 and GEo-02, based on the large-scale cross-section of Moscariello, 2019 and the lithological reports of the two wells (Chablais and Rusillon, 2017, 2019). The two columns present the subsurface reconstructions, based on the bedding picks in chapter 7. The image is not to scale.

8.2. Stress regimes in the Geneva Basin

The fracture sets of GEo-01 and GEo-02 are compared and correlated in terms of stress regimes.

- Set 1 in GEo-01 consists of steeply dipping veins associated with a normal or strike-slip regime. This set is abundant in GEo-01 and not related to local structures such as folds or faults. It is assumed that this set is also present in GEo-02, although it could not be identified on the ABI logs.
- Set 2A and 2B in GEo-01 are interpreted as a pair of conjugate fractures formed under a reverse regime, with σ_1 oriented NE-SW. They are clearly observed in GEo-01 but seem less developed in GEo-02.
- Set 3 in GEo-01 is interpreted as polymodal fractures linked to a normal stress regime. However, these polymodal fractures are not observed in GEo-02.
- Set 4A and 4B in GEo-01 are interpreted as another pair of conjugate fractures formed under a reverse regime, with σ_1 oriented NW-SE. It is possible that Sets 1 and 2 in GEo-02 represent the same pair of conjugates, but this is uncertain as it is not supported by any indications of movement.
- Set 5 in GEo-01 is characterized by a pair of joints, likely associated with the presence of faults. The absence of these joints in GEo-02 and the lack of evidence of faults in that well confirm this interpretation.
- Set 3 in GEo-02 forms steeply dipping NW-SE oriented fractures. This set is not recognized in GEo-01, and since it is less abundant than the other sets, it will be considered as having local significance and will not be discussed hereinafter.

To summarize, this study identified four Mesozoic to Cenozoic stress regimes in the basin, interlinked to the fracture sets: 1) a normal or strike-slip regime, 2) a NE-SW reverse regime, 3) a normal regime, and 4) a NW-SE reverse regime. A fifth fracture set is related to faults.

8.3. Integration to the geological history

The proposed succession of events is largely consistent with paleostress reconstructions in the nearby Jura Mountains from Homberg et al., 1999, Homberg et al., 2002, and Polasek, 2020. All three studies mention an abundant fracture population related to the Late Miocene NW-SE fold-and-thrust tectonics, which is considered the main deformation event of the region. It is possible that the conjugate pair of Set 4 in GEo-01 represent this NW-SE compression in the Geneva Basin.

Besides this main deformation event, Homberg et al., 2002; Homberg et al., 1999 and Polasek, 2020 identify several other, pre-orogenic, fracture sets in the Jura Mountains. The veins observed in GEo-01 seem to be in accordance with an Oligocene NW-SE extension reported by Homberg et al., 2002. The set of NW-SE oriented conjugates observed in GEo-01 might be related to a pre-folding NE-SW compression phase, as suggested by the work of Homberg et al., 1999. This study suggests that the change in stress orientations (NE-SW in this event to NW-SE in the fold-and-thrust event) is related to a decoupling along the Vuache fault. As a result, the basin acted as a rigid indenter of the Jura and caused a deflection of the stress field. The work of Lo, 2019 on GEo-01 previously suggested this theory but had not found evidence supporting it. The polymodal fracture set is not recognized in any of the other studies, nor GEo-02. For that reason, either this set may occur only locally, although the exact formation mechanisms remain unidentified, or is not identified on the stereoplots.

Set 5 is related to faulting near GEo-01. This finding is consistent with that of Koumrouyan, 2019, who found a similar relationship between fractures and faults between 460 and 480 m[MD]. The work argues that the faults formed in a NW-SE compressional stress field which is in accordance with the relative chronology in this study.

8.4. Correlation between fractures and lithology

In terms of stratigraphy, the succession of four regimes would be consistent with the formations encountered in the basin and the two erosional surfaces topping the Mesozoic and Oligocene rocks.

Interestingly, the results of this study, Lo, 2019 and Koumrouyan, 2019 all found a clockwise rotation in the dip direction of the fractures with depth: dipping north in the top and south in the bottom of GEo-01. Both Lo, 2019 and Koumrouyan, 2019 suggest this might be caused by contrasting mechanical properties of the different stratigraphic layers, causing local stress deflections. The image logs of GEo-01 and GEo-02 include mainly the same Cretaceous formations, so it is assumed that both wells should have similar contrasts in mechanical properties. However, the fractures in GEo-02 do not show the same pattern in the dip direction as observed in GEo-01, which makes the correlation of rock mechanical properties to stress orientations unlikely. Furthermore, the veins do not exhibit such a rotation. It is assumed that if all fractures show a clockwise rotation caused by mechanical properties, the veins would exhibit a similar pattern. The absence of such a pattern implies that the clockwise rotation in orientation is caused by a local stress perturbation, that only occurred after the formation of the veins. One possible explanation for these stress perturbations is the presence of faults. While there does not appear to be a direct correlation between the clockwise rotation and the potential faults observed on the image log, it is possible that the rotation is associated with faults beyond the coverage of the image logs.

8.5. Limitations and recommendations for future research

8.5.1. Statistical analysis

Despite this study's best aims to reduce uncertainties, the statistical analysis itself is not excluded from uncertainties or limitations. The chosen method for the statistical analysis was ANOVA/MANOVA, the most powerful test for circular data according to the work of Landler et al., 2022. A potential weakness in these tests is the p-value, now set to 0.95. Although this is a value that is commonly used and provides a certainty level of 95%, the p-value can also be obtained by theoretical approaches (such as Monte Carlo simulation), making the tests more robust.

It could be interesting to investigate the effect of the different interpretations on the outcomes of geomodels. This study proves that interpretations are significantly different, but the exact effect on subsequent modelling remains unexplored. If the effect appears to be significant, considerably more work will need to be done to reduce uncertainties in interpretation. It should be noted that three different fracture models are available from the Geneva Basin, based on three out of the five fracture interpretations. Lo, 2019 created a fracture model based on her own fracture interpretation, Alhamad, 2021 created a model based on the interpretation of Koumrouyan, 2019, and Jorge, 2022 created a model based on a re-interpretation of the work of Koumrouyan, 2019. However, the three models cannot simply be compared, because all three have used different methodologies. Lo, 2019 and Alhamad, 2021 base their paleo-tectonic stresses on a fault interpretation of the seismic lines, assuming the faults and fractures are related to the same deformation event. While Lo, 2019 applies a geomechanics-based stochastic simulation, Alhamad, 2021 applies a pure geomechanical approach. Jorge, 2022 defines the paleo-stresses based on a combination of fault interpretations from the seismic lines and fracture interpretations from the borehole data. The major limitation in these three studies is that all three consider only one tectonic regime responsible for fracture formation. However, the findings of this study demonstrate that in GEo-01, the fractures are formed by a succession of events, and the majority of fractures were formed prior to the development of faults. It would be interesting to investigate the potential impact of using only fracture data as input for modeling, without incorporating fault interpretations.
It was decided to manually define the boundaries of a set based on the shape of the contours. This approach is sufficient if data shows minimal scatter and well-defined clusters. However, the fracture data analyzed in this work did show a wide range of orientations, making it difficult to define distinct clusters. A more favourable approach would have been to establish set boundaries using a statistical method, such as described by Lacombe et al., 2011. The statistical approach used by Lacombe et al., 2011 involves assigning weight to data points, identifying cluster centra through probability density models and classifying fractures based on their distance from a cluster centre. Implementing a similar approach would make the set definition less arbitrary and more robust.

8.5.2. Understanding of the fracture history

Not all fracture sets are observed at both well locations. For some sets, this is explained in terms of data or local stress perturbations, but for Sets 2 and 3 in GEo-01, it remains dubious why the sets are observed in GEo-01 and not in GEo-02. Especially for Set 2, it is unlikely that this set is absent near GEo-02 because it forms such a large population in GEo-01, and the set has been identified in the nearby Jura Mountains by Homberg et al., 1999. That study interpreted that Set 2 prevailed since the fold-and-thrust tectonics, which implies it might be present throughout the basin. Homberg et al., 1999 also mentions a minor development of reverse fractures due to the proximity of active thrusts. A possible explanation for the absence of this set in GEo-02 could thus be related to its distance to the Jura fold-and-thrust. However, the question to be asked is whether the discrepancy in fracture abundance between GEo-01 and GEo-02 can be solely attributed to their distance to the Jura thrust. Another explanation could be that this set is present in the subsurface of GEo-02 but has gotten overshadowed by the other structures on the stereonet. A third explanation could involve a combination of both factors.

The polymodal fractures of Set 3, on the other hand, forms a much smaller population in GEo-01 and has not been recognized in any other literature. Either the set only occurs locally, or the discrepancy is related to the wide range of orientations in polymodal fracturing. The characteristic distribution of polymodal fractures on a stereoplot might be hard to recognize, easily overshadowed by other sets or seen as outliers. Data from outcrops (in preparation: Hupkes, 2023; Zekic, 2023) or other (to be drilled) wells is required to predict the distribution of these sets throughout the Geneva Basin.

The relative chronology of events could be reconstructed, although evidence is limited. Fracture data from outcrops (in preparation: Hupkes, 2023; Zekic, 2023) or other (to be drilled) wells could provide more definitive evidence. Furthermore, detailed 3D seismic data has been acquired throughout the basin and is yet to be processed and interpreted. Seismic data is a powerful tool to represent the subsurface and can be used to detect faults or folds and investigate their relationship to fractures.

Furthermore, it is important to highlight that a higher number of fractures were identified in GEo-01 compared to GEo-02, even though GEo-02 covers a larger depth interval. Gaillot et al., 2007 mentions that in general, fewer fractures are picked on ABI logs compared to OBI logs. Therefore, this discrepancy in fracture frequency may not be solely attributed to any geological aspect but is also partly influenced by the available data.

8.6. Importance of the research

Interpretations are based on data that is indirect, scarce, and of poor quality. They are biased by a person's experience, prior knowledge, and workflow and are, therefore, inherently uncertain. Nevertheless, interpretations form the basis of geomodels and can ultimately influence decision-making in a project. Reducing uncertainty is thus extremely valuable, especially in the early stages of a project. In recent years, uncertainty analysis has gained interest in geosciences (Bárdossy and Fodor, 2001). But so far, no attempt was made to investigate the uncertainty associated with fracture interpretation from image logs.

The results of the statistical analysis prove that the five interpretations from GEo-01 significantly differ. As elaborately described in chapter 6 the interpreters show large differences in picking numbers and frequency, which can be attributed to the classification approach, the lithology, the image log and the orientation bias of the well. An accurate fracture frequency is crucial for developing fracture models, which typically involve multiple depth intervals to capture variations in fracture density with depth.

The interpreters show an overall higher agreement in the mineralized fractures compared to the open/shear fractures. Mineralized fractures generally show more contrasting colours with the background rock, making them easier to identify compared to open/shear fractures. Since mineralized fractures generally do not contribute to an enhanced fluid flow in a reservoir, and as fracture models usually consider only one tectonic event, fracture models primarily focus on open/shear fractures. Likewise, Alhamad, 2021; Jorge, 2022; Lo, 2019 only include open fractures in their models. It is therefore presumed that the picking of mineralized fractures will have little impact on geomodels.

Lo, 2019 and Jorge, 2022 demonstrate significant differences in dip angles compared to Koumrouyan, 2019; SIG, 2020 and Doesburg, 2023. The primary factors contributing to this discrepancy are software settings and discontinuities in the caliper log. The dip angle plays a crucial role in the determination of the orientations of the paleo-principal stresses. Consequently, the dip angle not only influences the understanding of stress regimes within the basin but also forms the foundation of geomodels.

Certain intervals show a significantly lower level of agreement compared to other intervals. This low level of agreement can be attributed to various factors that negatively impact the quality of the image log. By identifying and marking these specific intervals, it becomes possible to assess the influence of low-quality image logs on the overall fracture population.

The list of recommendations provides a tool to reduce uncertainties in fracture interpretations from image logs. Specifically in the Geneva Basin, where two more wells are planned to be drilled in terms of the GEothermie2020 project, but probably also in a much broader context.

8.6.1. Implications for the GEothermie2020 project

This study will have important implications for the Geothermie2020 project. The analysis of the five interpretations and the resulting recommendations have led to a more reliable fracture dataset from the two available wells. Previously, a detailed inspection of the image log had not been performed, but it has now provided new insights into the relative chronology between fractures and the type of movement they exhibited. This allowed for the definition of fracture sets, leading to the interpretation of four successive stress regimes in the Geneva Basin. The timing of these events had not been established before. Lo, 2019 mentioned the NE-SW and NW-SE compression events, but has been unable to demonstrate their relative timing. The results of this study provided evidence for their timing, supporting the work of Homberg et al., 1999 in the Jura Mountains.

The improved understanding of the geological history made it possible to deduct the paleo-principal stress directions. In many modelling approaches, these principal stresses provide the foundation for fracture prediction. Since most models rely on a single tectonic event, it is recommended to model a NW-SE reverse regime based on the largest fracture set identified in this study. Notably, Alhamad, 2021 and Jorge, 2022 have used a normal regime, although Jorge, 2022 acknowledged the poor fit with the data. On the other hand, Lo, 2019 incorporated two tectonic events (a strike-slip event and a reverse event) but did not constrain their chronology. Updating one of the pre-existing models with the proposed stress orientations could have large implications for fracture prediction in the basin.

Furthermore, the results of this study suggest that the observed clockwise rotation with depth in open/shear fractures may not be as closely related to geomechanical properties as suggested by Lo, 2019 and Koumrouyan, 2019. Instead, it is possible that local stress perturbations might be related to faulting, although further research is required before implementing this idea into a model.

The relationship between fracture Set 5 from GEo-01 and the presence of faults had previously been proposed by Koumrouyan, 2019. This relationship is particularly important because the faults contribute to a local increase in fracture frequency, which might create preferential flow pathways for fluids. Such considerations should be taken into account in the GEothermie2020 project to contribute to the successful development of geothermal energy in Geneva.

9

Conclusions

The objective of this research was to answer the following question:

'How to reduce uncertainties in fracture interpretation from borehole images to optimize fracture data acquisition and provide a reliable structural history in the Geneva Basin?'

A statistical analysis of the five fracture interpretations revealed areas of disagreement among the interpreters. A qualitative analysis followed, investigating possible explanations for these differences. As a result, a workflow was developed for fracture interpretation on image logs, concerning data quality, software settings, workflow and the integration of pre-existing knowledge of stratigraphy. The workflow was applied to the interpretations of GEo-01 and GEo-02, leading to a more reliable fracture database.

An analysis of the resulting fracture data, in combination with observations of displacement and relative chronology, led to the definition of five fracture sets in GEo-01 and 3 sets in GEo-02. These sets were interpreted to have formed during four successive stress regimes. The first regime is a normal or strike-slip regime, creating NE-SW oriented nearly vertical veins. The second regime is a reverse one with σ_1 oriented NE-SW and characterized by a pair of conjugates. The third regime remains dubious and might only occur locally near GEo-01. It is typified by polymodal fracturing, formed in a normal regime. The last regime is reverse, with σ_1 oriented NW-SE, creating a second pair of conjugates. The latter forms the majority of fractures, which is believed to be related to the Late Miocene fold-and-thrust tectonics. One set is fault-related and is only observed in GEo-01.

The findings of this study hold two important implications. Firstly, they contribute to the reduction of uncertainties in future fracture interpretations, particularly for the GEothermie2020 project, and potentially in a much broader context. Secondly, the study provides a better understanding of fracture formation in the basin. These findings can be used to update pre-existing fracture models, in order to predict flow in the Cretaceous rocks, which are considered the primary reservoirs for the GEothermie2020 project. Since primary porosity and permeability are relatively low in these rocks, natural fractures will play a crucial role by forming pathways for fluids to flow.

Bibliography

Ahmadi, R., Mercier, E., Trigui, H., & Ouali, J. (2019). Relatiosnhip between fracture patterns and fold kinematics; the case study of jebel sehib, a typical fault-propagation fold of southern tunisia. *Journal of African Earth Sciences*, *152*, 23–35.

Alhamad, M. (2021). Msc. thesis: Fracture network prediction in the geneva basin: A geothermal case study. *Delft University of Technology*.

Allen, P., & Allen, J. (2013). *Basin analysis: Principles and application to petroleum play assessment*. Wiley-Blackwell.

Andre-Ghapgou, M. (2021). Msc. thesis: Characterization of fractured and karstified limestone reservoir for aquifer thermal energy storage (ates). *Université de Neuchâtel*.

Atunes, V., Planes, T., Zahradnik, J., Obermann, A., Alvizuri, C., Carrier, A., & Lupi, M. (2020). Seismotectonics and 1-d velocity model of the greater geneva basin, france–switzerland. *Geophysical Journal International*, *221*, 2026–2047.

Bárdossy, G., & Fodor, J. (2001). Traditional and new ways to handle uncertainty in geology. *Natural Resources Research*, *10*(3), 179–187.

Billi, A., Salvini, F., & Storti, F. (2003). The damage zone-fault core transition in carbonate rocks: Implications for fault growth, structure and permeability. *Journal of Structural Geology*, *25*, 1779–1794.

Bisdom, K. (2016). Burial-related fracturing in sub-horizontal and folded reservoirs: Geometry, geomechanics and impact on permeability. *Delft University of Technology*.

Bistacchi, A., Mittempergher, S., Martinelli, M., & Storti, F. (2020). On a new workflow for the statistical and spatial analysis of fracture data collected with scanlines (or the importance of stationary). *Solid Earth Discussions*.

Blenkinsop, T. (2008). Relationships between faults, extension fractures and veins, and stress. *Journal of Structural Geology*, *30*(5), 622–632.

Bond, C. (2015). Structural model creation: The impact of data type ad creative space on geological reasoning and interpretation. *Geological Society Londen Special Publications*, *421*(1).

Chablais, J., & Rusillon, E. (2017). Geo-01: Litholog de forage - litholog report (llr). *Hydro-Geo Environment - Geothermie 2020*.

Chablais, J., & Rusillon, E. (2019). Geo-02: Litholog de forage - litholog report (llr). *Hydro-Geo Environment - Geothermie 2020*.

Chelle-Michou, C., Do Couto, D., Moscariello, A., Renard, P., & Rusillon, E. (2017). Geothermal state of the deep western alpine molasse basin, france-switzerland. *Geothermics*, *67*, 48–65.

Clerc, N., Rusillon, E., Moscariello, A., Renard, P., Paolacci, S., & Meyer, M. (2015). Detailed structural and reservoir rock typing characterisation of the greater geneva basin, switzerland for geothermal resource assessment. *World Geothermal Congress, Melbourne, Australia*.

Driesner, T. (2021). Heatstore: Final report on tools and workflows for simulating subsurface dynamics of different types of high temperature underground thermal energy storage. *Geothermica - ERA NET Cofund Geothermal*.

Du Couto, D., Garel, S., Moscariello, A., Daher, S., & Littke, R. (2021). Origins of hydrocarbons in the geneva basin: Insights from oil, gas and source rock organic geochemistry. *Swiss Journal of Geosciences*, *114*(11).

Dürrast, H., & Siegesmund, S. (1999). Correlation between rock fabrics and physical properties of carbonate reservoirs. *International Journal of Earth Sciences*, *88*, 392–408.

Fossen, H. (2016). *Structural geology* (2th ed.). Cambridge University Press.

Gaillot, P., Brewer, T., Pezard, O., & Yeh, E. (2007). Borehole imaging tools - principles and applications. *Scientific Drilling*, *5*.

Guglielmetti, L., & Moscariello, A. (2021). On the use of gravity data in delineating geologic features of interest for geothermal exploration in the geneva basin (switzerland): Prospects and limitations. *Swiss Journal of Geosciences*, *114*(15).

Haas, M., Carraro, D., Ventra, D., Plötze, M., De Haller, A., & Moscariello, A. (2022). Integrated stratigraphic, sedimentological and petrographical evaluation for cern's future circular collider subsurface infrastructure (geneva basin, switzerland-france). *Swiss Journal of Geosciences*, *115*(16).

Healy, D., Blenkinsop, T., Timms, N., Meredith, P., Mitchell, T., & Cooke, M. (2015). Polymodal faulting: Time for a new angle on shear fracture. *Journal of Structural geology*, *80*, 57–71.

Homberg, C., Bergerat, F., Philippe, Y., Lacombe, O., & J.Angelier. (2002). Structural inheritance and cenozoic stress fields in the jura fold-and-thrust belt (france). *Tectonophysics*, *357*, 137–158.

Homberg, C., Lacombe, O., J.Angelier, & Bergerat, F. (1999). New constraints for indentation mechanisms in arcuate belts from the jura mountains, france. *Geology*, *27*(9), 827–830.

Hsu, K., Brie, A., & Plumb, R. (1987). A new method for fracture identification using array sonic tools. *Journal of Petroleum Technology*, *39*, 677–683.

Hupkes, J. (2023). Phd thesis - in preparation. *Delft University of Technology*.

Jammalamadaka, S. R. (2001). *Topics in circular statistics* (5th ed.). World Scientific.

J.H.Williams & Johnson, C. (2004). Acoustic and optical borehole-wall imaging for fractured-rock aquifer studies. *Journal of Apllied Geophysics*, *55*, 151–159.

Jiang, L., Qiu, Z., Wang, Q., Guo, Y., Wu, C., Wu, Z., & Xue, Z. (2016). Joint development and tectonic stress field evolution in the southeastern mesozoic ordos basin, west part of north china. *Journal of Asian Earth Sciences*, *127*, 47–62.

Jorge, S. (2022). Msc. thesis: Fracture characterisation in carbonate reservoirs for geothermal production. *Delft University of Technology*.

Khoshbakht, F., Memarian, H., & Mohammadnia, M. (2009). Comparison of asmari, pabdeh and gurpi formation's fractures, derived from image log. *Journal of Petroleum Science and Engineering*, *67*(1-2), 65–74.

Kim, Y., Peacock, D., & Sanderson, D. (2004). Fault damage zones. *Journal of Structural Geology*, *26*, 503–517.

Koumrouyan, M. (2019). Msc. thesis: Geomechanical characterisation of geothermal exploration borehole: Implication for the geo-01 well, in geneva. *Université de Neuchâtel*.

Lacombe, O., Bellahsen, N., & Mouthereau, F. (2011). Fracture patterns in the zagros simply folded belt (fars, iran): Constraints on early collisional tectonic history and role of basement faults. *Geological Magazine*, *148*(5-6), 940–963.

Lai, J., Liu, B., Li, H., Pang, X., Liu, S., Bao, M., & Wang, G. (2022). Bedding parallel fractures in fine-grained sedimentary rocks: Recognition, formation mechanisms, and prediction using well log. *Petroleum Science*, *19*, 554–569.

Lai, J., Wang, G., Fan, Z., Wang, Z., Cheng, J., Zhou, Z., Wang, S., & Xiao, C. (2017). Fracture detection in oil-based drilling mud using a combination of borehole image and sonic logs. *Marine and Petroleum Geology*, *84*, 195–214.

Landler, L., Ruxton, G., & Malkemper, E. (2022). The multivariate analysis of variance as a powerful approach for circular data. *Movement Ecology*, *10*(21).

Laubach, S., & Olson, J. (2009). Mechanical and fracture stratigraphy. *AAPG Bulletin*, *93*(11), 1413–1426.

Lavenu, A., Lamarche, J., Salardon, R., Gallois, A., Marie, L., & Gauthier, B. (2014). Relating background fractures to diagenesis and rock physical properties in a platform-slope transect. example of the maiella mountain (central italy). *Marine and Petroleum Geology*, *51*, 2–19.

Lecompte, M. The geothermie2020 program: Supporting the development of geothermal resources use in gevena canton. In: In *Aapg 3rd hydrocarbon geothermal cross over technology workshop*. (3). 2019.

Lo, H. (2019). Msc. thesis: Discrete fracture network modelling in the geneva basin (lower cretaceous carbonates): Implication for geothermal exploration. *Université de Genève*.

Lorenz, J., & Cooper, S. (2020). *Applied concepts in fractured reservoirs* (1st ed.). John Wiley Sons, Ltd.

Matte, P. (2003). The variscan collage and orogeny (480-290 ma) and the tectonic definition of the armorica microplate: A review. *Terra Nova*, *13*(2), 122–128.

Moscariello, A. (2019). Exploring for geo-energy resources in the geneva basin (western switzerland): Opportunities and challenges. *Swiss Bulletin für Angewandte Geologie*, *24*(2), 105–124.

Moscariello, A., Guglielmetti, L., Salé, S., Haller, A., Eruteya, O., Lo, H., Clerc, N., Makhloufi, Y., Couto, D., Oliveira, G., Perozzi, L., Filho, F., Hollmuller, P., Quiquerez, L., Bono, C., Martin, F., & Meyer,

M. (2020). Heat production and storage in western switzerland: Advances and challenges of intense multidisciplinary geothermal exploration activities, an 8 years progress report. *World Geothermal Congress, Reykjavik, Iceland*.

Planes, T., Obermann, A., Antunes, V., & Lupi, M. (2019). Ambient-noise tomography of the greater geneva basin in a geothermal exploration context. *Geophysical Journal International*, *220*(1), 370–383.

Polasek, D. (2020). Kinematic and hydrogeological role of the jura mountains'haute-chaine fracture network. *MSc Thesis Univesity of Geneva*.

Rusillon, E. (2018). Characterisation and rock typing of deep geothermal reservoirs in the greater geneva basin (switzerland and france). *Université de Genève*.

Schaaf, A., & Bond, C. (2019). Quantification of uncertainty in 3-d seismic interpretation: Implications for deterministic and stochastic geomodeling and machine learning. *Solid Earth*, *10*(4), 1049–1061.

Schori, M., Zwaan, F., Scheurs, G., & Mosar, J. (2019). Pre-existing basement faults controlling deformation in the jura mountains fold-and-thrust belt: Insights from analogue models. *Tectonophysics*, *814*.

Serra, O. (1983). *Fundamentals of well-log interpretation*.

Shalaby, M., & Islam, M. (2017). Fracture detection using conventional well logging in carbonate matulla formation, geisum oil field, souther gulf of suez, egypt. *Journal of Petroleum and Production Technology*, *7*, 977–989.

SIG. (2020). Rapport de fin de sondage geo-01. *Unpublished report*, 137–170.

Signer, C., & Gorin, G. (1995). New geological observations between the jura and the alps in the geneva area, as derived from reflection seismic data. *Eclogea Geologicae Helvetiae*, *88*(2), 235–265.

Sommaruga, A., Mosar, J., Schori, M., & Gruber, M. (2017). The role of the triassic evaporites underneath the north alpine foreland. *Tectonics and Hydrocarbon Potential*, 447–466.

Strasser, A., Charollais, J., Conrad, M., Clavel, B., Pictet, A., & Mastrangelo, B. (2016). The cretaceous of the swiss jura mountains: An improved lithostratigraphic scheme. *Swiss Journal of Geosciences*, *109*, 201–220.

Tartarotti, P., Ayadi, M., Pezard, P., Laverne, C., & Larouziere, F. D. (1998). Multi-scalar structure at dsdp/odp site 504, costa rica rift, ii: Fracturing and alteration. an integrated study from core, downhole measurements and borehole wall images. *Geological Society, London, Special Publications*, *136*, 391–412.

Watkins, H., Healy, D., Bond, C., & Butler, R. (2018). Implications of heterogeneous fracture distribution on reservoir quality: An analogue from the torridon group sandstone, moine thrust belt, nw scotland. *Journal of Structural Geology*, *108*, 180–197.

Zekic, S. (2023). Msc thesis - in preparation. *Delft University of Technology*.

A

ANOVA/MANOVA and Tukey-Kramer test

This appendix presents the calculations and results of the ANOVA, MANOVA and Tukey-Kramer results. All calculations have been executed using Microsoft Excel and python.

A.1. Calculations

A.1.1. ANOVA

1. Calculate per group: total count (*n*), mean (X_j), and variance (σ^2)
2. Calculate the overall mean ($\overline{X}$) of all groups
3. Calculate the sum of squares regression (*SSR*) by:

$$\sum_{j=1}^{n}(X_j - \overline{X})^2$$

4. Calculate the sum of squares error (*SSE*) by:

$$\sum_{j=1}^{n}(X_{ij} - X_j)^2$$

5. Calculate the sum of squares total (*SST*) by:

$$SSR + SSE$$

6. Calculate the degrees of freedom (*df*) between the groups, within the groups and total
7. Calculate the mean squares (*MS*) between the groups and within the groups by:

$$\frac{SST}{df_{betweengroups}}$$

and

$$\frac{SSE}{df_{withingroups}}$$

8. Calculate the F value (*F*) by:

$$\frac{MS_{betweengroups}}{MS_{withingroups}}$$

9. Find the critical F value (F_{crit}) from the F-distribution table with $df_{between\ groups}$, $df_{within\ groups}$ and the chosen α value

A.1.2. MANOVA

1. Calculate the total mean vector ($\overline{X}_\mathrm{T}$) by:

$$\begin{bmatrix} \overline{x}_1 \\ ... \\ \overline{x}_k \end{bmatrix}$$

where

$$\overline{x}_p = \frac{1}{n}\sum_{j=1}^{m}\sum_{i=1}^{n_j} x_{ijp}$$

2. and the group mean vector ($\overline{X}_\mathrm{j}$) by:

$$\begin{bmatrix} \overline{x}_{j1} \\ ... \\ \overline{x}_{jk} \end{bmatrix}$$

where

$$\overline{x}_{jp} = \frac{1}{n_j}\sum_{i=1}^{n_j} x_{ijp}.$$

3. Calculate the cross product of *p* and *q*: CP_{pq} by:

$$\sum_{j=1}^{m}\sum_{i=1}^{n_j}(x_{ijp} - \overline{x}_p)^2$$

4. And create the sum of squares cross product matrix ($SSCP_T$):

$$T = \begin{bmatrix} CP_{11} & ... & CP_{1k} \\ ... & ... & ... \\ CP_{k1} & ... & CP_{kk} \end{bmatrix}$$

or by:

$$T = \sum_{j=1}^{m}\sum_{i=1}^{m_j}(X_{ij} - \overline{X}_T)(X_{ij} - \overline{X}_T)^T$$

5. And define the hypothesis (H) and error (E) cross products, in which $T = H + E$:

$$H = \sum_{j=1}^{m} n_j(\overline{X}_j - \overline{X}_T)(\overline{X}_j - \overline{X}_T)^T$$

$$E = \sum_{j=1}^{m}\sum_{i=1}^{n_j}(X_{ij} - \overline{X}_j)(X_{ij} - \overline{X}_j)^T$$

6. Calculate Wilk's Lambda, and reject the null hypothesis of Wilk's Lambda is close to 0:

$$\Lambda = \frac{|E|}{|H + E|}$$

and let:

$$a = n - m - \frac{k - m + 2}{2}$$

$$b = \begin{cases} \sqrt{\frac{k^2(m-1)^2-4}{k^2+(m-1)^2-5}}; & \textit{if } k^2 + (m-1)^2 - 5 > 0 \\ 1; & \textit{if } k^2 + (m-1)^2 - 5 \leq 0 \end{cases}$$

$$c = \frac{k(m-1) - 2}{2}$$

7. Then, if the null hypothesis is true:

$$F = \left(\frac{1 - \Lambda^{1/b}}{\Lambda^{1/b}}\right)\left(\frac{ab - c}{k(m-1)}\right) F_{k(m-1),ab-c}$$

A.1.3. Tukey-Kramer test

1. Find the absolute mean difference between each group, using the output of the ANOVA/MANOVA test.
2. Find the critical value (q_{crit}) from the Studentized Range q table, with α = 0.05, number of groups (k) and degrees of freedom (df_{crit}). Calculate the critical value for differences in mean, with n is the size each group:

$$mean_{crit} = q_{crit}\sqrt{MS_{withingroups}/n}$$

A.1.4. Example

Figure A.1 shows an example of the results of the ANOVA calculations and Figure A.2 shows an example of the results of the Tukey-Kramer test.

Anova: Single Factor						
SUMMARY						
Groups	*Count*	*Sum*	*Average*	*Variance*		
GGE	22	681,04	30,95636364	195,0553385		
KL	6	275,48221	45,91370167	143,2364263		
MD	21	833,75	39,70238095	148,930879		
MK	27	821,62	30,43037037	111,5727652		
SJ	11	536,91	48,81	85,84742		
ANOVA						
Source of Variation	*SS*	*df*	*MS*	*F*	*P-value*	*F crit*
Between Groups	4076,563907	4	1019,140977	7,23525433	4,84856E-05	2,48303405
Within Groups	11550,32792	82	140,8576575			
Total	15626,89182	86				

Figure A.1: Calculations of ANOVA method on the fracture dip data of interval C.

TUKEY HSD/KRAMER			Alpha	0,05					
Groups	*Average*	*Count*	*SS*	*df*	*q-crit*				
GGE	30,95636364	22	4096,162109						
KL	45,91370167	6	716,1821316						
MD	39,70238095	21	2978,617581						
MK	30,43037037	27	2900,891896						
SJ	48,81	11	858,4742						
		87	11550,32792	82	3,944804878				
Q TEST									
Group 1	Group 2	Mean	Std err	q-stat	Lower	Upper	P-value	Mean-crit	Cohen d
GGE	KL	14,95733803	3,86515828	3,869786681	-0,289957206	30,20463327	0,057173611	15,24729524	1,26027
GGE	MD	8,746017316	2,560285951	3,416031445	-1,353811192	18,84584582	0,121485991	10,09982851	0,73692
GGE	MK	0,525993266	2,410349671	0,218222805	-8,982365875	10,03435241	0,99869942	9,508359141	0,04432
GGE	SJ	17,85363636	3,099021006	5,761056904	5,628603182	30,07866955	0,000985321	12,22503318	1,50431
KL	MD	6,211320714	3,884828423	1,598866163	-9,113569401	21,53621083	0,789916532	15,32489011	0,52335
KL	MK	15,4833313	3,787692341	4,087800672	0,541624074	30,42503852	0,038454444	14,94170722	1,30459
KL	SJ	2,896298333	4,259196981	0,680010421	-13,90540269	19,69799936	0,988907801	16,80170103	0,24404
MD	MK	9,272010582	2,441767575	3,797253546	-0,360286059	18,90430722	0,06492481	9,632296641	0,78124
MD	SJ	9,107619048	3,123519577	2,915819422	-3,214056216	21,42929431	0,246672714	12,32167526	0,76739
MK	SJ	18,37962963	3,001848753	6,122770046	6,537922025	30,22133723	0,000395967	11,8417076	1,54863

Figure A.2: Calculations of Tukey-Kramer test on the fracture dip data of interval C

A.2. Results

Calculations were made for each type, characteristics and interval. The Figure A.3 and A.4 below represent the outcomes; green represents $mean_{crit}$ > mean and red represents $mean_{crit}$ < mean.

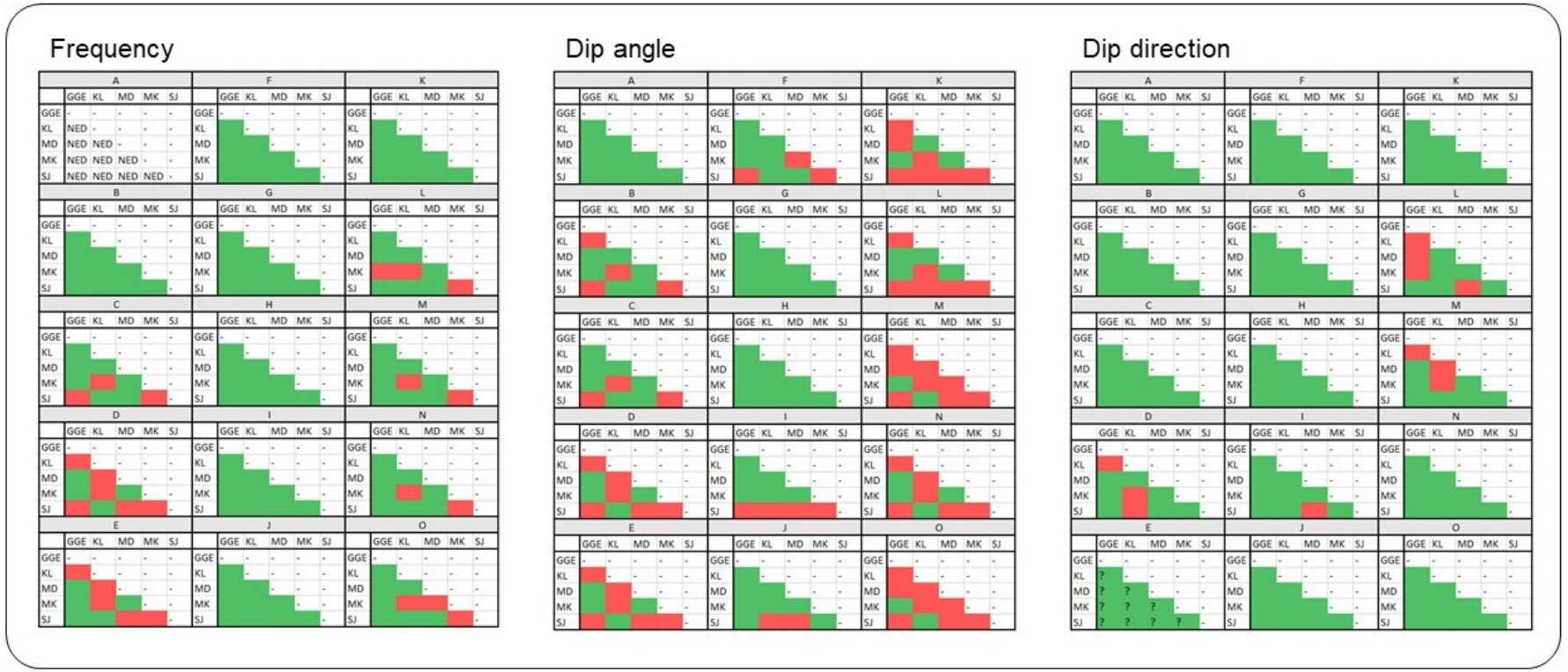

Figure A.3: Results of the Tukey-Kramer test for the open/shear fractures. Calculated per depth interval (A-O, see Table 5.1) and every possible combination of interpreters. Red represents a significant difference, green represents no significant difference, NED stated Not Enough Data and the question mark is where ANOVA/MANOVA implies at least one group is different from the others, but is does not show from the Tukey-Kramer results.

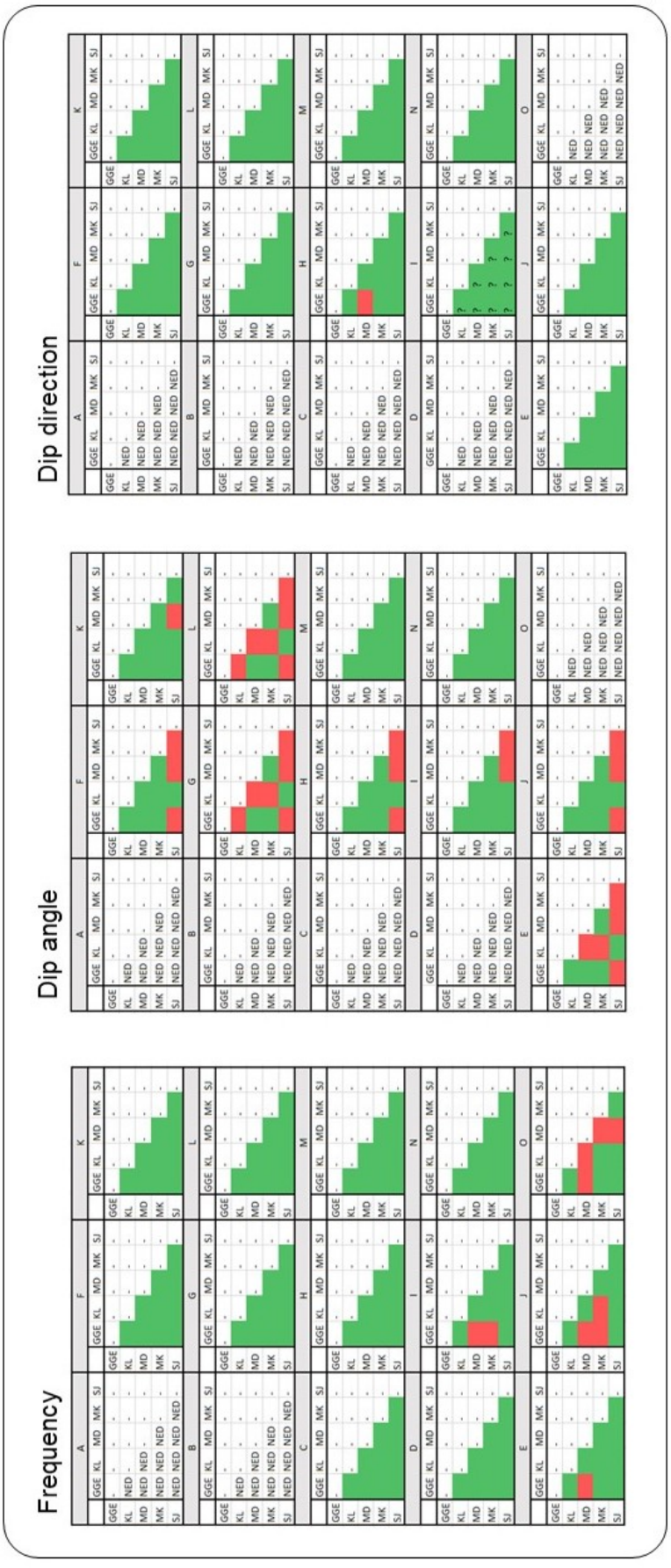

Figure A.4: Results of the Tukey-Kramer test for the mineralized fractures. Calculated per depth interval (A-O, see Table 5.1) and every possible combination of interpreters. Red represents a significant difference, green represents no significant difference, NED stated Not Enough Data and the question mark is where ANOVA/MANOVA implies at least one group is different from the others, but is does not show from the Tukey-Kramer results.

B

Quantitative analysis of interpretations

The figures below (Figure B.1 and B.2) present a quantitative analysis on the interpretations, with possible reasons for (dis)agreement among interpreters and advice for future fracture picking from image log.

		Fractures					
Interval	Depth [m]	Agree	Disagree	NED	Reasons of agreement	Reasons of disagreement	Advice
A	412 - 414	Azimuth / Dip	-	Frequency	The quality of the image log is poor, the interval is small, resulting in few picks per interpreter	-	Picking at the edges of an image log should be done with great uncertainty, if the quality is poor
B	414 - 423	Azimuth / Frequency	Dip	-	The complexity of the image log is high	SJ and KL get deviated dip angles because of software settings	Pay attention to software settings (see REFERENCE TO TEXT OR APPENDIX) and where complexity is high, contrast between colors on the image log is larger, highlighting structures and making them easier to pick
C	423 - 427	Azimuth	Dip / Frequency	-	The complexity of the image log is high	SJ and KL get deviated dip angles because of software settings	-
D	427 - 432	-	Azimuth / Dip / Frequency	-	-	Disagreement in the classification of bedding and fractures	Where limestones alternate with marls and/or sandstones, be aware of the bedding orientation and make use of geophysical logs
E	432 - 453	Azimuth [?]	Dip / Frequency	-	The quality of the image log is very good	Disagreement in the classification of bedding and fractures	-
F	453 - 456	Azimuth / Frequency	Dip	-	The quality of the image log is good, complexity is high, and not much structures are picked	SJ gets deviated dip angles	Picking in marls and fine sandstones can be done with great certainty, if the quality is good and classification clear
G	456 - 458	Azimuth / Dip / Frequency	-	-	The quality of the image log is good, complexity is high, and not much structures are picked	-	-
H	458 - 460	Azimuth / Dip / Frequency	-	-	The quality of the image log is good, and complexity is high	-	-
I	460 - 475	Frequency	Azimuth / Dip	-	The quality of the image log is good	SJ gets deviated dip angles	-
J	475 - 480	Azimuth / Frequency	Dip	-	The quality of the image log is very good, and complexity is high	SJ gets deviated dip angles	-
K	480 - 495	Azimuth / Frequency	Dip	-	The quality of the image log is poor in some areas, resulting in few picks	Disagreement in the classification of bedding and fractures, and SJ and KL get deviated dip angles because of software settings	Picking might be limited and therefore unrepresentative, if the image log quality is poor
L	495 - 512	-	Azimuth / Dip / Frequency	-	-	Large differences in image complexity, disagreement in classification, and SJ and KL get deviated dip angles because of software settings	A change in image log quality and complexity (and possibly lithology), results in very different picking. Keep in mind: is that because the rocks are structurally different or because the data affects the picking of the interpreter? The same applies for veins (SEE NEXT TABLE)
M	512 - 516	-	Azimuth / Dip / Frequency	-	-	Disagreement in the classification of bedding and fractures	Where quality is high and structures are clear, be aware of bedding orientation and be consistent/confident in the classification of structures
N	516 - 526	Azimuth	Dip / Frequency	-	The quality of the image log is poor in some areas, resulting in few picks	SJ and KL get deviated dip angles because of software settings	-
O	526 - 533	Azimuth	Dip / Frequency	-	The quality of the image log is good	Inconsistent caliper log	Structure dips are linked to the caliper log. If this log is inconsistent, this leads to incorrect dip angles

Figure B.1: Possible explanations for the differences in fracture picking by the five interpretations. Columns 1 and 2 give the lithological intervals and their depth. Columns 3 to 5 repeat the results of the statistical analysis, based on Figure 6.4. Columns 6 and 7 give the possible reasons for the (dis-)agreement amongst the interpreters.

		Veins					
Interval	Depth [m]	Agree	Disagree	NED	Reasons of agreement	Reasons of disagreement	Advice
A	412 - 414	-	-	Azimuth / Dip / Frequency	-	-	No picked structures results in NED for the statistical analysis. Either no veins are present, which implies high agreement amongst the interpreters, or they are present, but not picked for other reasons
B	414 - 423	-	-	Azimuth / Dip / Frequency	-	-	-
C	423 - 427	Frequency	-	Azimuth / Dip	Each interpreter picked few veins	-	Agreement in frequency and NED for azimuth/dip could imply limited veins are present
D	427 - 432	Frequency	-	Azimuth / Dip	Each interpreter picked few veins	-	-
E	432 - 453	Azimuth	Dip / Frequency	-	The quality of the image log is good	Disagreement in the number of picked veins, and SJ and KL get deviated dip angles because of software settings	If many other structures (bedding, fractures) are present, vein picking may be downplayed. This is in agreement with the picking in F/G/H/I/J. Adjusting software settings could highlight veins (see REFERENCE TO TEXT OR APPENDIX)
F	453 - 456	Azimuth / Frequency	Dip	-	The quality of the image log is good, complexity is high and not much other structures present	SJ gets deviated dip angles	-
G	456 - 458	Azimuth / Frequency	Dip	-	The quality of the image log is good, complexity is high and not much other structures present	SJ and Kl get deviated dip angles	-
H	458 - 460	Frequency	Azimuth / Dip	-	The quality of the image log is good, and complexity is high	Disagreement in the number of picked veins, and SJ gets deviated dip angles	-
I	460 - 475	Azimuth (?)	Dip / Frequency	-	The quality of the image log is good	Disagreement in the number of picked veins, SJ gets deviated dip angles	-
J	475 - 480	Azimuth	Dip / Frequency	-	The quality of the image log is very good, and complexity is high	Disagreement in the number of picked veins, SJ gets deviated dip angles	-
K	480 - 495	Azimuth / Frequency	Dip	-	Each interpreter picked few veins	SJ gets deviated dip angles	-
L	495 - 512	Azimuth / Frequency	Dip	-	Varying quality of the image log	SJ and Kl get deviated dip angles	See PREVIOUS TABLE
M	512 - 516	Azimuth / Dip / Frequency	-	-	Each interpreter picked few veins	-	-
N	516 - 526	Azimuth / Dip / Frequency	-	-	Each interpreter picked few veins	-	-
O	526 - 533	-	Frequency	Azimuth / Dip	-	Disagreement in the number of picked veins	-

Figure B.2: Possible explanations for the differences in vein picking by the five interpretations. Columns 1 and 2 give the lithological intervals and their depth. Columns 3 to 5 repeat the results of the statistical analysis, based on Figure 6.4. Columns 6 and 7 give the possible reasons for the (dis-)agreement amongst the interpreters. The question marks are intervals where the ANOVA/MANOVA outcome suggested a significant difference, while the post hoc test gave no difference amongst any pair of interpreters.

C

WellCAD settings

This appendix shows screenshots of the most important settings in WellCAD.

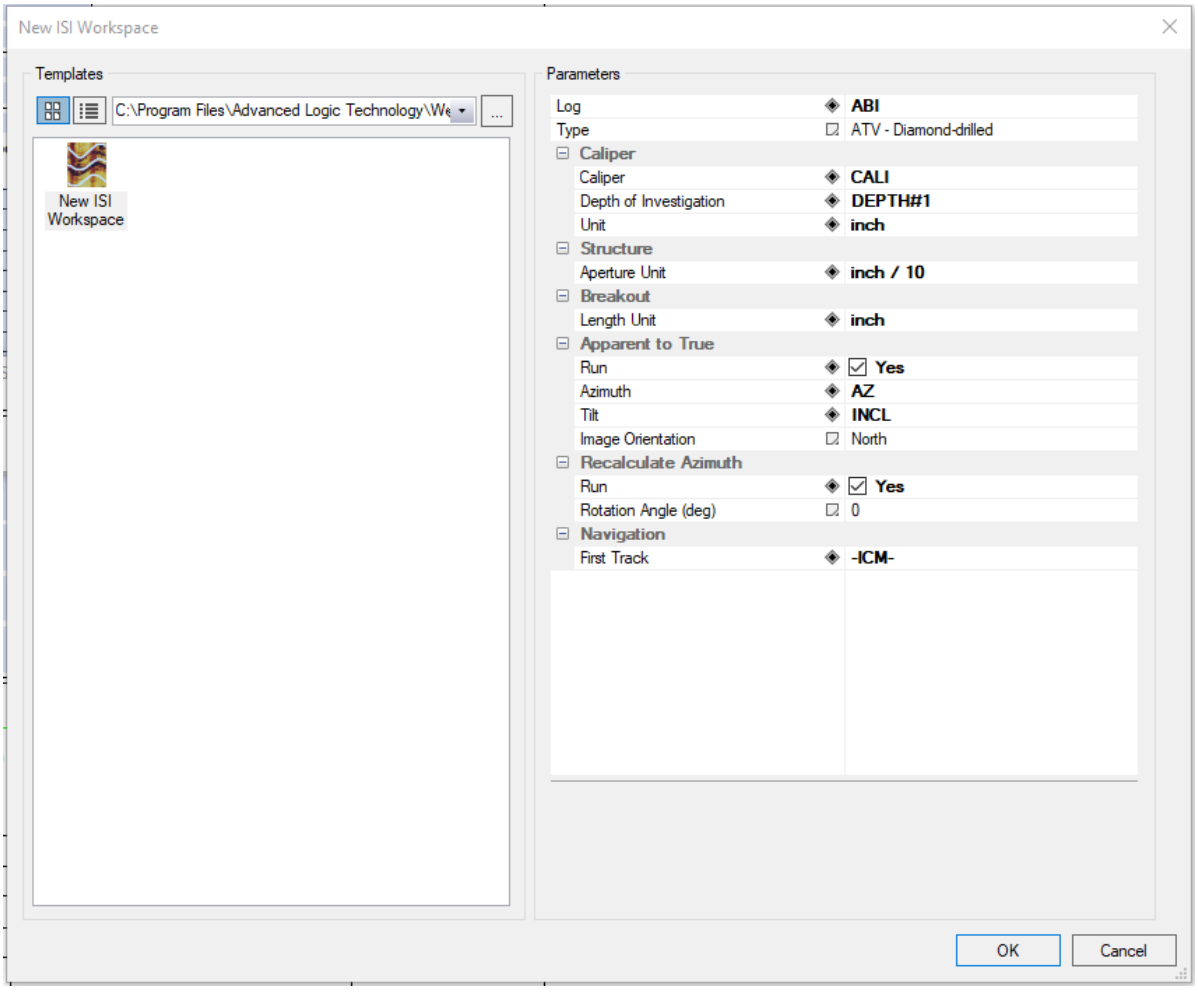

Figure C.1: Workspace setup settings, with in bold the properties that should be defined (Unit, Aperture unit, Length Unit), linked to a log (Log, Caliper, Depth of Investigation, Azimuth, Tilt) or adjusted to preference (Recalculate Azimuth, First track).

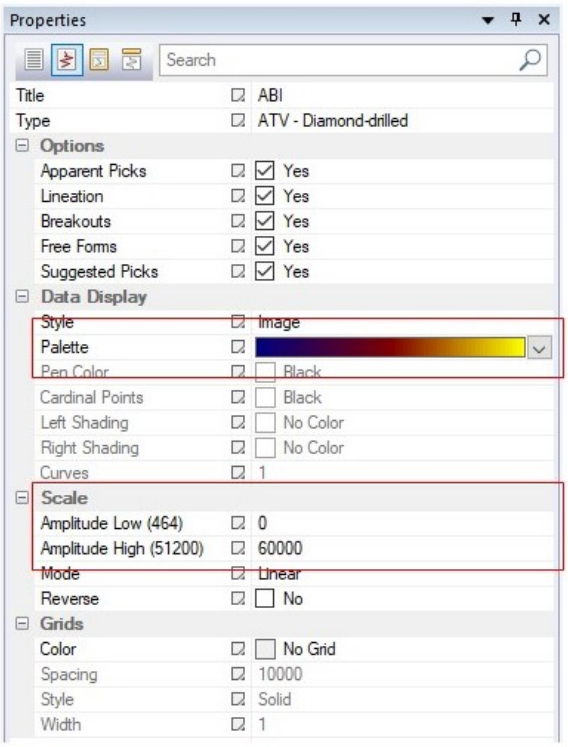

Figure C.2: Properties can be adjusted to filter the image log and highlight certain structures. Select the log (Type), and adjust to preference (Palette, Amplitude).

D

Stereoplots per depth interval

This appendix presents stereoplots per 10m interval for GEo-01 open/shear fractures, GEo-01 mineralized fractures and GEo-02 open/shear fractures.

D.1. GEo-01

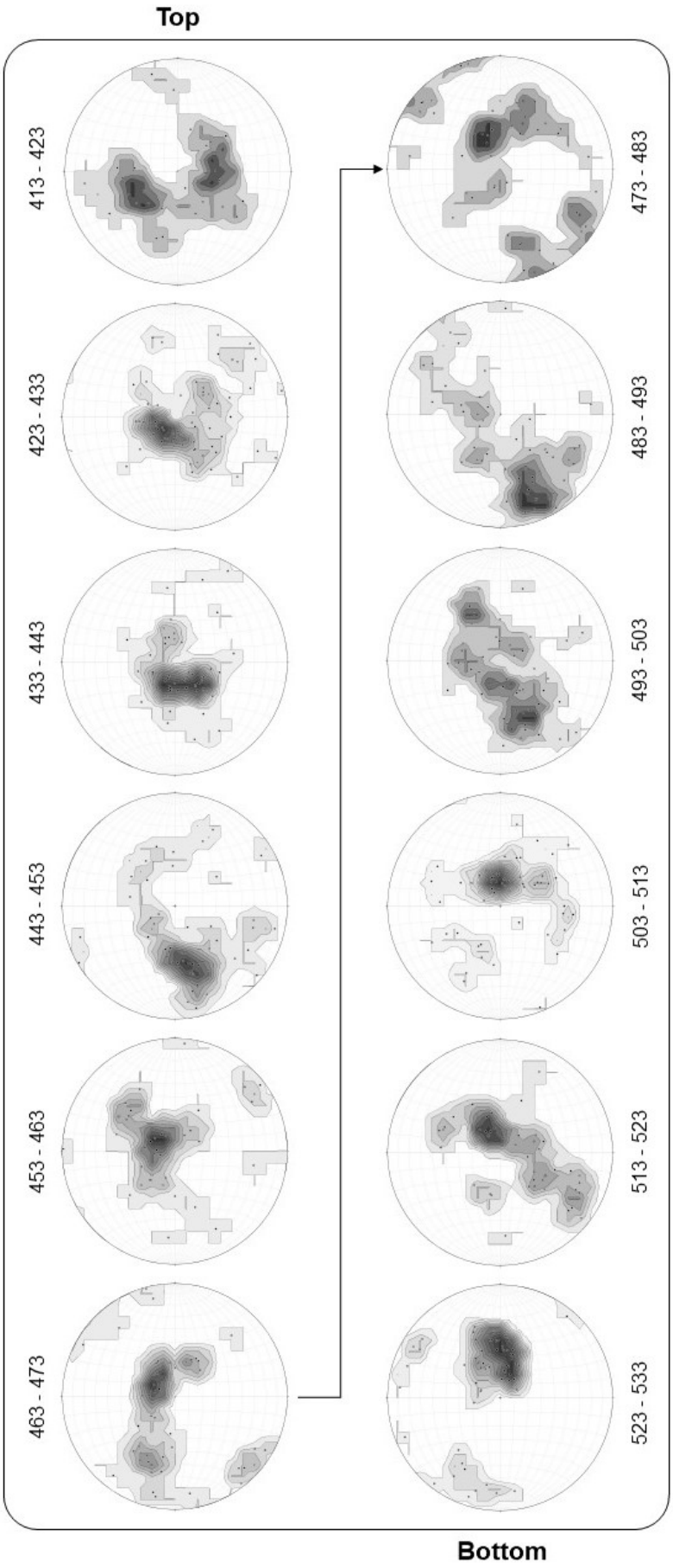

Figure D.1: Stereoplots per 10m of the open/shear fractures of GEo-01.

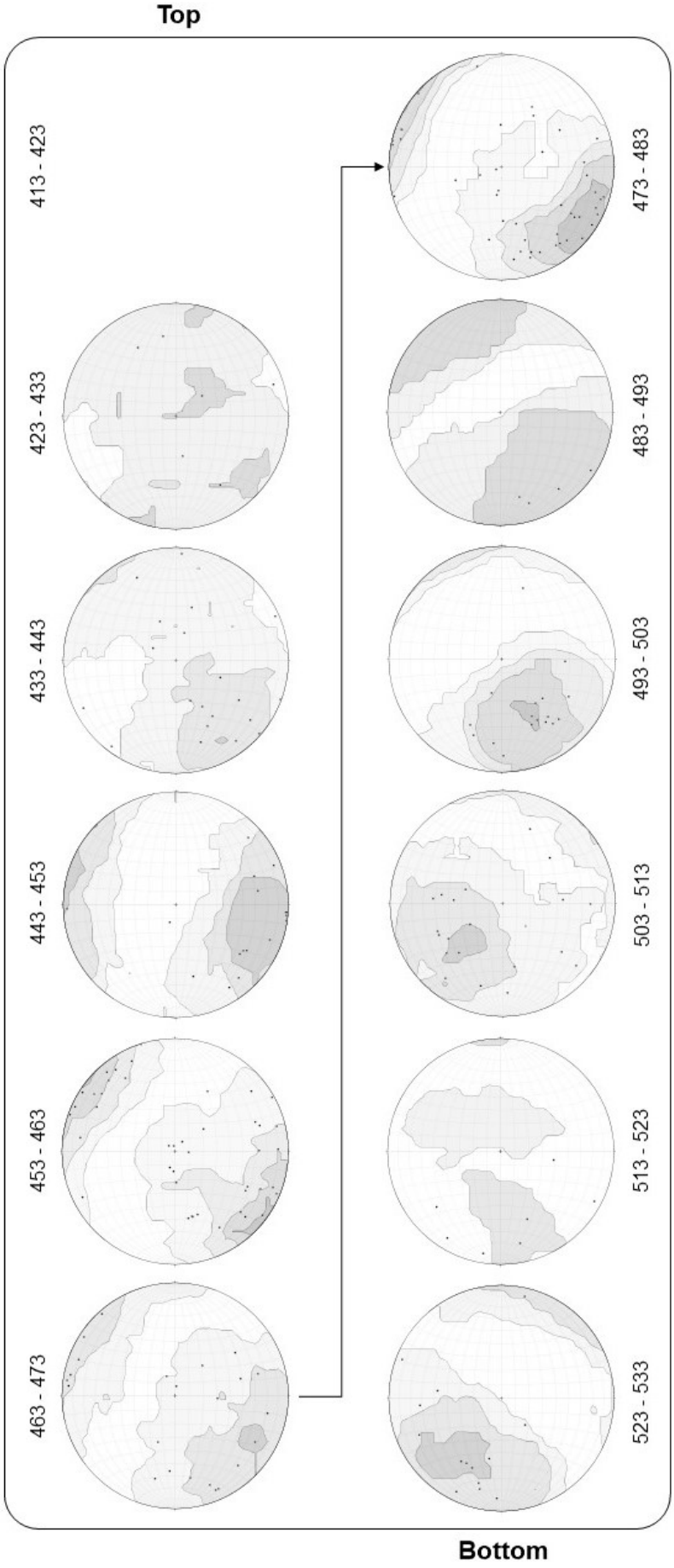

Figure D.2: Stereoplots per 10m of the mineralized fractures of GEo-01.

D.2. GEo-02

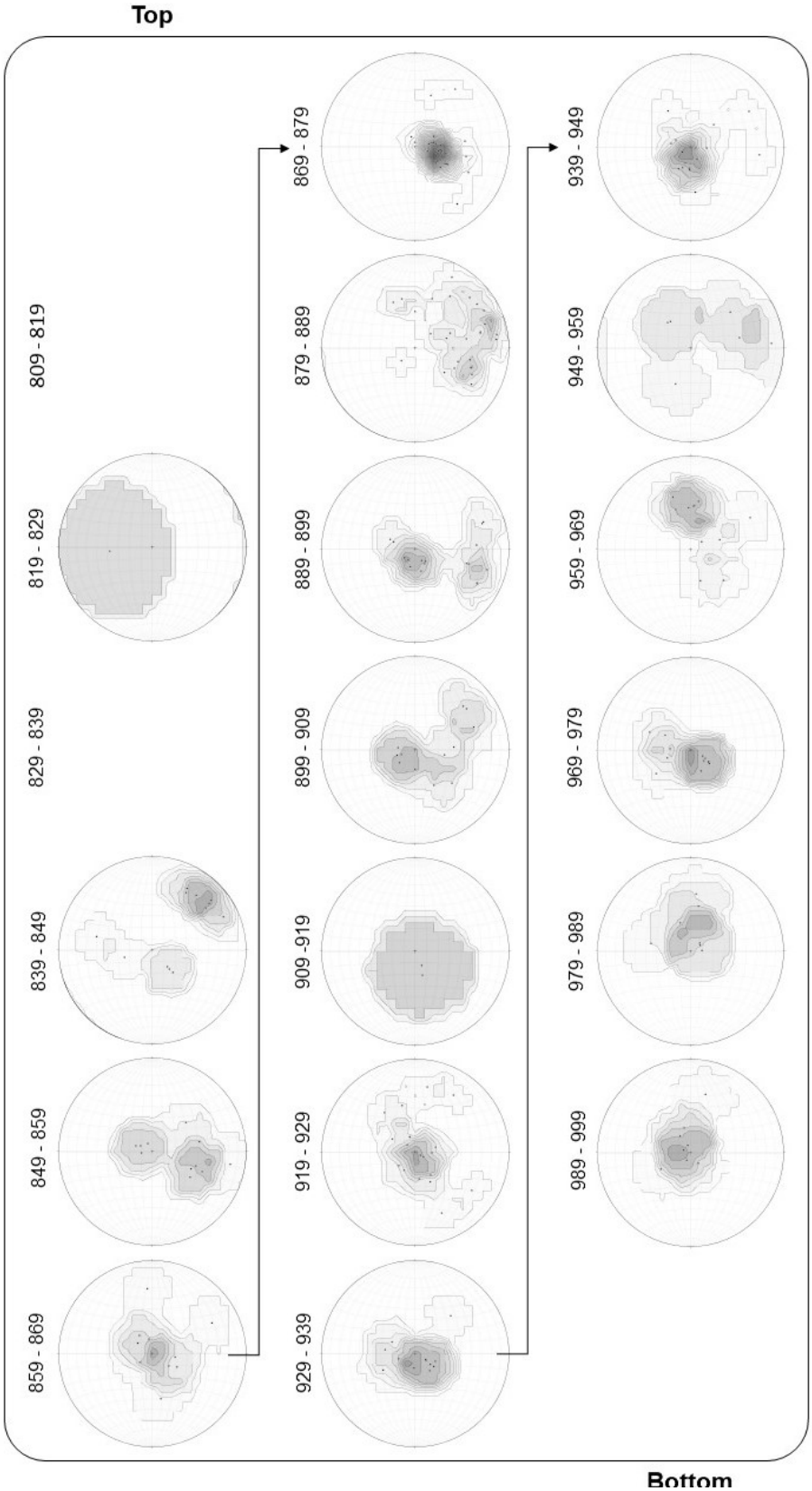

Figure D.3: Stereoplots per 10m of the fractures of GEo-02.